Dynamics of Stark Acceleration/Deceleration: Molecules Riding Waves

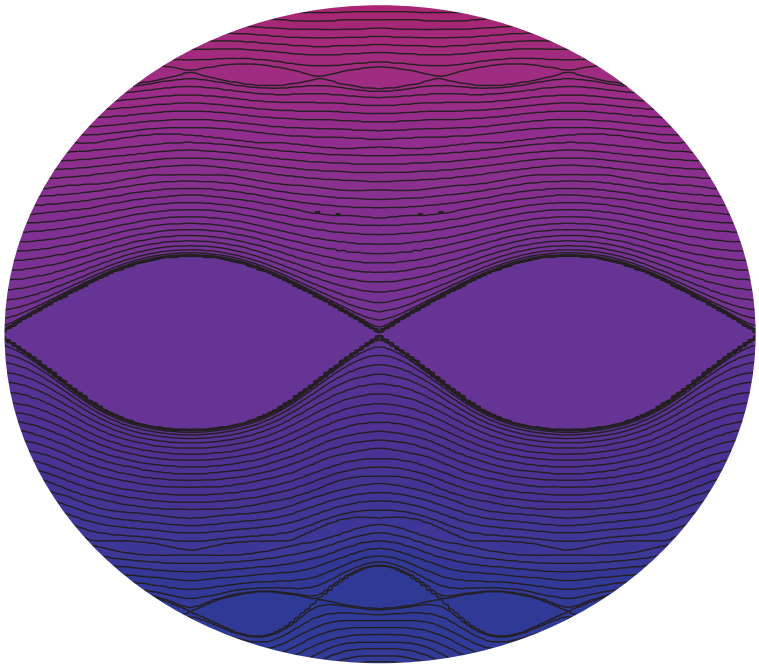

Koos Gubbels

Dynamics of Stark Acceleration/Deceleration: Molecules Riding Waves

Koos Gubbels

Master's Thesis

Department of Molecular and Laser physics
Radboud University Nijmegen

26th January, 2006

Research performed at:
Fritz-Haber-Institut der Max-Planck-Geselschaft
Department of Molecular Physics
Faradayweg 4-6
14195 Berlin

Under daily supervision of: Dr. Bretislav Friedrich
Thesis supervisor: Prof. dr. Gerard Meijer

Thanks

The past ten months I did research for my master's thesis at the Molecular Physics department of the Fritz-Haber-Institut der Max-Planck-Gesellschaft in Berlin. I had a great time there. Not only because Berlin is a very lively city and the Germans are very humoristic people, but mostly because I loved doing research, especially at this particular institute. The atmosphere in the department was great; everybody was very open, interested, fun and helpful. I experienced that a pleasant working environment can have a very positive influence on the quality of your work. For this I really have to thank the whole department.

But there are some people who played a special role in the realization of this thesis. First of all, I would like to express my deep gratitude to Bretislav Friedrich, who was my daily supervisor at the Fritz-Haber-Institute the past year. We worked together very closely and fruitfully on the wave model of Stark deceleration, which resulted in a paper (to be submitted soon) and this thesis. Bretislav, thank you very much for teaching me everything about cold molecules and physical modelling, for all the interesting historical anecdotes (scientific or not) you shared with me over a cup of cappuccino and for all the other things you have done for me; I enjoyed it a lot.

I was also very lucky with Gerard Meijer as a second supervisor, responsible for the quality and the final judgement of my thesis. Gerard, your exceptional qualities as a physicist, teacher and motivator are well-known and don't need any further explanation. But in addition I found it very special that a director of such a big department, who is so busy, always finds time to be scientifically and (maybe even more important) personally involved with everybody in the department. I am very grateful for having been able to profit from that.

Furthermore, I need to mention my two roommates at the institute, Bas van de Meerakker and Joop Gilijamse, who played a particular important role in making my stay at the institute a very pleasant one. Bas, thank you very much for answering all my questions and for sharing all your impressive knowledge about the Stark decelerator, which makes you almost a third supervisor for this thesis. Without your help, I would have never been able to make all those links between the wave model and the actual experiments. Joop, thank you very much

for the very nice experiment we performed (see Paragraph 4.5) and for keeping me informed about the latest developments down under in the lab. I also really admire you for staying so positive and cheerful in a year that Ajax almost lost every week, while PSV was conquering Europe.

And of course I want to thank all the other people in the department. Nicolas Vanhaecke, who continued his career in Zürich, but who taught me a lot about decelerating and simulating when he was still in Berlin; Joost Bakker, for throwing a party every time he won another prize; Steven Hoekstra, Andreas Ostenwalder, and Jochen Küpper for all the small and big (computer) help; Cynthia Heiner, Jacqueline van Veldhoven, Irena Labazan, Sophie Schlunk, Melanie Schnell and Undine Erlekam for providing the department with some girl power; and everybody I have accidentally forgotten.

A special thanks goes to my parents for everything they have done for me, which is 'quite' a lot: from always supporting me to letting me see the world, from teaching me all the important things I know to spoiling me whenever I am at home. I also want to thank my friends for visiting me and my roommates in Berlin for making my stay in a foreign country, which is not always easy, a lot of fun. And last but not least I want to thank my girlfriend Roosje for being the sweetest person in the world.

Contents

Chapter 1

General Introduction

Physics is the branch of science that studies the most general laws that govern the material world around us. In performing their mission, physicists make extensive use of two useful sets of tools, namely measuring instruments and mathematics. A measuring instrument allows a physicist to directly extract quantitative information from nature. This is called an experiment. Mathematics allows physicists to formulate a set of rules describing a certain regime in nature. This is called a model or a theory. There exists a rich interplay between theory and experiments. In order to understand experiments, theory is needed, and, conversely, in order to prove a theory, experiments are needed. Furthermore, new theoretical discoveries often lead to new experimental observations, which is also true for the other way around.

The demands that a good model or theory has to fulfill vary widely. First of all, a model has to be internally consistent. Second, it has to be in accurate quantitative agreement with the results coming from experiments. A model is especially convincing, if it is able to predict new phenomena that have never been observed before. This is the reason why most physicists like the Standard Model, since it accurately predicted the existence of several particles, before they were ever observed in nature. Third, a model is judged on the amount of phenomena it can explain using the same set of assumptions, which is called unification. A good example is the statistical description of thermodynamics where a very broad range of phenomena can be explained by assuming that the underlying system consists of a hughe number of tiny particles.

Sometimes, the criteria by which a model is judged, can also be quite subjective. 'Beauty' can play an important role in appealing to the physics community. A model is considered to be 'beautiful' when it is based on very few assumptions, the derivations are done without (too many) approximations and the resulting equations are simple. Other appealing features are symmetry, originality, intelligibility and visualizability. A good example of a theory that became popular because of its visual properties is Feynman's diagrammatic approach to

quantum field theory.

This thesis is also about a model, namely the wave model of Stark deceleration. A Stark decelerator is an apparatus that produces slow molecules by applying time-varying inhomogeous electric fields to a a molecular beam pulse [1]. Fourier analysis reveals that the time-varying electric fields give rise to an infinite multitude of running waves propagating through the decelerator [2]. The goal of this thesis is to give a full description of the longitudinal dynamics in a Stark decelerator by tackling analytically the effect of every individual wave on the motion of the molecules. Also the analytic results of the wave model will be extensively compared with the results from numerical simulations and experiments.

But first we put the research with the Stark decelerator in a broader context and briefly discuss the motivation for studying cold molecules. Furthermore, we'll have a quick look at the most used techniques for producing cold molecules, which will bring us automatically to Stark deceleration. We'll discuss the previous work with the Stark decelerator in more detail to obtain a framework in which this thesis can be placed. This introduction will be concluded with an outline for the rest of the thesis.

1.1 Applications of Cold Molecules

Cold molecules are slow molecules. Or, more accurately, since the notion of slowness is relative: cold molecules have a small width in their velocity distribution. As in the case of a molecular beam, the small velocity spread of cold molecules can also be centered around a high mean velocity in the lab frame. Still, whenever in this thesis cold molecules are mentioned, it will be assumed that they are moving slowly in the lab frame. This in contrast to a molecular beam, where molecules are cold in a moving frame.

Since cold molecules move slowly in the lab frame, they provide long interaction times with measuring devices, such as detection lasers. As a result, the resolution of spectroscopic measurements using cold molecules can be improved by orders of magnitude [3]. Furthermore, slow molecules can be confined in space by using electrostatic or magnetic traps, increasing the interaction times with measuring devices even more. This also creates the possibility of determining long lifetimes of metastable states [4], that cannot be measured using conventional molecular beam methods.

Since cold molecules give rise to high spectroscopic resolution, they are suitable candidates for metrology experiments and sensitive symmetry tests. An example of such a symmetry

test is the search for the electric dipole moment (EDM) of the electron, as predicted by physics beyond the Standard Model. Such an EDM would violate time reversal symmetry and could be related to the asymmetric distribution between matter and anti-matter in the Universe [5]. A polar molecule, like YbF, is a particularly suitable system for measuring a possible EDM, because it provides a large enhancement of an applied electric field. As a result, an unpaired electron in YbF gives rise to an equally enhanced energy shift, provided it has an EDM [6]. So far, the EDM has not been found, although the experimental upper bound has already reached the range in which theory predicts the EDM to be. By decelerating and trapping the YbF molecules, the experimental resolution will be further increased, resulting in an even lower upper bound on the EDM. This will either lead to the discovery of the EDM or to a falsification of theories beyond the Standard Model.

The improved spectroscopic resolution of cold molecules can also be used to search for possible traces of the weak interaction in chiral molecules. The weak interaction violates mirror symmetry (parity) and could therefore result in a difference between the energy spectra of left- and right-handed chiral molecules [7, 8]. Such a difference then might explain the preference of biochemical systems for left handed amino acids, which up to now has not been understood.

In 1923, Louis de Broglie showed that particles can be attributed a wavelength that is inversely proportional to their momentum. As a result, slow particles have a large wavelength. At room temperature, the de Broglie wavelength of a small molecule is typically 0.1 Å, i.e. smaller than the size of the molecule. But for small (ultra)cold molecules at 1 mK the wavelength is on the order of 100 Å, considerably exceeding molecular dimensions. As the wavelength of the particles increases, their quantum mechanical wave character takes over. A particularly exciting regime is entered, when the wavelength of the particles starts exceeding the inter-particle separation. In the 1990's, this regime was reached with atoms, which led to a revolutionary transformation of atomic physics marked by milestone experiments, such as the observation of Bose-Einstein condensation (BEC) [9], Fermi degeneracy [10], the demonstration of an atom laser [11] and of non-linear atom optics [12, 13]. Molecular physics is undergoing a similar transformation, where molecules could provide extra dimensions to the experiments mentioned above, because of their richer structure than atoms.

For example, polar molecules possess a body fixed dipole moment, which would give rise to an anisotropic dipole-dipole interaction in a molecular BEC. By playing around with trap shapes, the dipole interaction can be made either attractive or repulsive, influencing the stability of the BEC [14]. As a result, the interaction in the BEC can be experimentally tuned, giving new possibilities to control macroscopic quantum states [15].

The increased wavelength of (ultra)cold molecules also has profound consequences for their chemical behavior. Collision experiments in the (ultra)cold regime will be governed by quantum mechanical effects and all kinds of resonances in the resulting cross sections have been predicted [16, 17]. Since a Stark decelerator can state selectively decelerate molecules to arbitrary final velocities, it is particularly well suited to probe this regime. In a crossed molecular beam setup, the predicted resonances could be studied in great detail as a function of the center-of-mass collision energy.

This last experiment represents the general potential of a Stark decelerator in offering full control over the translational motion of gas phase molecules, particularly in the low velocity range [18]. Controlling both the internal and the external degrees of freedom of gas-phase molecules has been a prominent goal in molecular physics during the last decades. Molecular beams, both continuous and pulsed, have been used throughout to produce large densities of molecules in selected quantum states. In these beams, the longitudinal velocity spread corresponds to a temperature of typically 1 K, and the mean velocity of the beam can be varied by adjusting the temperature of the source or by using different carrier gases. In this way, beams have been obtained with a velocity typically in the 300 m/s to 2000 m/s range, but not much lower. Since a Stark decelerator succeeds in deceleration all the way down to zero velocity [19, 20], the technique allows for molecular beam experiments in a whole new range of velocities.

Finally, the trapping of ultracold polar molecules in a optical lattice has been proposed for realizing a quantum computation scheme [21]. In this design, the electric dipole moment of a polar molecule, oriented along or against an applied electric field, acts as a qubit, the quantum mechanical counterpart of a bit. Coupling between different qubits can be realized through the electric dipole-dipole interaction.

1.2 Production of Cold Molecules

In every day life people think of cooling in terms of a decrease in temperature. In physics we rather associate cooling with an increase in phase space density, which can be defined as [22]

$$D = n\Lambda^3 \tag{1.1}$$

where n is the number density and $\Lambda = (2\pi\hbar^2/mkT)^{1/2}$ is the thermal de Broglie wavelength. Therefore, cooling techniques that increase the phase space density are referred to as real cooling, in contradistinction to cooling techniques which only lower the temperature at the expense

of the number density.

1.2.1 Laser Cooling and Association of Cold Atoms

One method to produce cold molecules is starting out from cold atoms and associating them to form cold molecules. Over the past decades, great progress has been made in cooling atoms, mainly due to the successful implementation of laser cooling [23]. This technique is based on the momentum transfer that occurs when an atom absorbs and re-emits a photon. In a suitable setup, the applied laser light acts as a friction force for the atoms, damping their motion and increasing the phase space density. The atoms have to undergo thousands of absorption-emission cycles before they reach ultracold temperatures. As a result, laser cooling can only be applied to atoms for which a 'closed' absorption-emission cycle can be found. This means that the atoms are only allowed to decay into exactly the same state from which they were excited. As a result, laser cooling is only applicable to a select group of atoms and essentially inapplicable to molecules.

When the laser cooled atoms are paramagnetic, they can be confined in a magnetic trap, where they establish a thermodynamic equilibrium. By subsequently lowering the depth of the trap, the hottest atoms are allowed to escape, after which the remaining atoms re-thermalize at a lower temperature. This is called evaporative cooling and it leads to a considerable increase of phase space density [24]. Using these techniques, the first atomic BEC was observed in 1995, consisting of 10^4 rubidium atoms with a density of 10^{12} atoms/cm^3 at a temperature of 170 nK [9]. This corresponds to a phase space density of about 3×10^{-1}.

Cold atoms can be associated to form cold molecules in several ways: by using photons (photo-association); by using a scattering resonance that is tunable with a magnetic field (Feshbach resonance); or by three body recombination of cold atoms. In 2003, application of a Feshbach resonance led to the first observation of molecular BEC's in K_2 and Li_2 [25, 26]. So far, only the production of ultracold homonuclear alkali dimers has been demonstrated with this technique. Since Feshbach resonances also have been found in dual-species traps [27, 28], this technique might lead soon to the production of ultracold polar bi-alkali dimers.

Photo-association of atoms has already resulted in the formation of bi-alkali dimers, like RbCs [29, 30]. Although the photo-associated dimers are translationally ultracold, they are typically produced in short lived high vibrational states of an electronically excited state. As a result, laser-stimulated transfer processes have to be applied to bring the molecules to their ground state [31].

1.2.2 Buffer-gas Cooling

The main disadvantage of cold atom association is the narrow range of applicability. Laser cooling can only be applied to a select group of atoms and the difficulty of their association limits the possibilities even further. A much more general technique to produce cold molecules is buffer gas cooling. Using cryogenic methods, helium can be cooled to a few hundred milliKelvin, where it still has a considerable vapor pressure. When hot molecules are injected into the cold helium gas, they thermalize with its atoms by means of collisions. As a result, the hot molecules end up with the same temperature as the buffer gas [32, 33].

The cryogenic setup can be extended with a superconducting magnetic trap, that is capable of confining paramagnetic molecules at the center of the cell. In 1998, buffer-gas cooling led to the first trapping experiment of neutral molecules. Hot CaH molecules were produced by laser ablation from a solid target inside the cell, after which about 10^8 molecules thermalized with the helium and were trapped in their rovibronic ground state. The obtained density was 10^8 molecules/cm^3 at a temperature of 400 mK [34].

In principle, every molecule can be buffer-gas cooled, provided that its cross section for collisions with helium are favorable for thermalization.

1.2.3 Deceleration of a Molecular Beam

Another way to produce cold molecules is to start out from a molecular beam. In the production process of a molecular beam, the free jet expansion, molecules are typically cooled to a (longitudinal) temperature of about 1 K and their density can be as high as 10^{13} molecules/cm^3. The only thing preventing these molecules from being trapped is their high mean velocity in the lab frame. Several methods have been developed to decelerate molecular beams and transfer their favorable properties to the lab frame. Since these techniques themselves do not increase the phase space density, they are not referred to as cooling techniques. Among them are Stark deceleration of polar molecules using time-varying electric fields [1], counter-rotation of the molecular beam source [35], inelastic collisions in crossed molecular beams [36], and pulsed optical fields for deceleration of polar or polarizable molecules [37].

So far, of these methods only Stark deceleration has resulted in the three dimensional trapping of neutral molecules [19, 20].

1.2.4 Previous Experimental Work on Stark Deceleration

In the 1960s, for the first time effort was undertaken to develop a Stark accelerator/decelerator with the goal to reduce the linewidth of a maser [38], or to study high energy molecular collisions

[39]. The efforts failed, mainly due to a lack of flexibility of the constructed machines. In 1999, Bethlem, Berden and Meijer demonstrated for the first time that a beam of neutral polar molecules can be decelerated using time-varying inhomogenous fields, called Stark deceleration. In their pioneering experiment, metastable CO ($a^3\Pi_1$) molecules were decelerated from 225 m/s to 98 m/s using 63 field stages [1]. A year later, the Stark decelerator was used to perform deceleration and electrostatic trapping of ground state ND_3 molecules, where 10^4 molecules were trapped with a density of 10^7 molecules/cm^3 at a temperature of 25 mK [19].

Subsequent work in Meijers group led to the construction of an electrostatic storage ring [40] and the development of a buncher. By combining the two, packets of ammonia were observed to make more than 50 round trips in the ring [41]. Furthermore, longitudinal focussing of a molecular beam by the buncher resulted in a velocity spread corresponding to a temperature of 250 μK [42]. Inspired by the success of the first decelerator, an up-scaled version was constructed, consisting of 108 field stages. With this decelerator OH radicals were trapped [20] and subsequently the long radiative life time of the first vibrationally excited state of OH was determined [4].

The experiments mentioned above have all been performed with molecules in so called low field seeking states, which means that such molecules are accelerated towards regions of minimum field strength. This in contradistinction to molecules in high field seeking states, which are accelerated towards regions of maximum field strength. As a result, Stark deceleration is more difficult for high field seekers which have a tendency to crash into the electrodes, where the electric field strength is maximal. By using dipole lenses as field stages, this problem can be overcome. A prototype of such an alternate gradient (AG) decelerator was able to focus and decelerate metastable CO molecules in a high field seeking state [43]. Combining the AG decelerator with an AC electric trap [44] provides in principle a method to trap any high field seeking polar molecule.

Since its introduction in 1999, various other groups have started to pursue implementation of the Stark deceleration technique. The group of Ye in Boulder, USA, has succeeded in decelerating OH [45, 46] and H_2CO molecules, although electrostatic trapping has not been reported yet. In Hannover, Germany, the group of Lisdat and Tiemann have recently built a Stark decelerator to slow down a beam of SO_2 molecules, whereas the group of Softley in Oxford, UK, is still in the middle of the construction process. In London, UK, a long AG decelerator has just become operational in the group of Hinds, that will be used to decelerate and trap YbF molecules, helping them in their search for the electric dipole moment of the

electron.

1.2.5 Previous Theoretical Work on Stark Deceleration

The Stark decelerator for neutral polar molecules is the equivalent of a linear accelerator (LINAC) for charged particles. In a Stark decelerator, the quantum-state specific force that a polar molecule experiences in an electric field is exploited. This force is rather weak, typically some eight to ten orders of magnitude weaker than the force that a corresponding molecular ion would experience in the same electric field. This force nevertheless suffices to achieve complete control over the motion of polar molecules, using techniques akin to those used for the control of charged particles.

A crucial feature of the Stark decelerator is that it can be operated under the conditions of phase stability. Phase stability, which is the basis for synchrotron-like charged particle accelerators [47, 48], enables to hold a packet of neutral molecules together throughout the Stark deceleration process. Phase stable operation of a Stark decelerator, viewed as trapping of neutral molecules in a travelling potential well, was first studied in connection with the early deceleration experiments on metastable CO [49]. In that work, as well as in later publications on the deceleration of various isotopomers of ammonia, the one-dimensional equation of motion for molecules that undergo phase-stable transport was given [50, 51]. In more recent work, the coupling between the transverse and the longitudinal motion was included, and the transverse stability in a Stark decelerator was discussed [52]. To arrive at the longitudinal equation of motion, the Stark energy (potential energy) of the molecules was expressed as a function of position along the decelerator axis, and the change in Stark energy per deceleration stage was evaluated. As this treatment did not yield *a priori* an expression for the force on the molecules as a function of time, assumptions about the time-dependence of the force were made to deduce, in an intuitive way, the equation of motion. The validity of these assumptions were checked against trajectory calculations, and it was concluded that this equation of motion indeed describes correctly the physics of the phase stable motion in a Stark decelerator [49, 50, 51]. Nevertheless, a mathematically rigorous derivation of the equation of motion and an in-depth analysis of the complex dynamics in a Stark decelerator was still wanting.

More recently, another approach was given to derive the equation of motion [2]. In that work, the (longitudinal) force acting on the molecules as a function of both their position and time was obtained by expressing the spatial and temporal dependence of the electric fields in terms of a Fourier series. The Fourier expansion resulted in an infinite sum of stationary and counter-propagating waves, where the interaction of a molecule with the dominant wave was treated explicitly. This resulted in an elegant derivation of the equation of motion, although

several questions remained. For example, it was not clear which role all the other waves in the expansion played and why, in discussing phase stability, it is allowed to take only one wave into account. Furthermore, it was not directly evident how to connect the given treatment to trajectory calculations or experiments. In particular, it was not clear where the experimentally observed second-order resonances, as first explained by the intuitive model [53], come from in the Fourier series description.

1.3 This Thesis

In this thesis, we give a full analysis of the longitudinal motion of molecules in a Stark decelerator. The description is based on the wave model [2], which is improved and generalized where needed. We treat analytically the motion of the molecules through phase space due to any of the waves in the Fourier expansion, as well as due to their mutual perturbations. Furthermore, we find an explanation for the experimentally observed second order resonances in terms of two wave interferences. Throughout the thesis, the link with the actual experimental situation is made. Finally, we compare the obtained analytical results with numerical calculations and with an experiment.

The thesis is built up as follows: in Chapter 2 we follow the route from the molecular Stark effect to a Stark decelerator. This serves as a background for Chapter 3, where we present the analytic treatment of the longitudinal physics in a Stark decelerator, the main content of this thesis. Finally, Chapter 4 provides the comparison of the theory with simulations and experiment.

Chapter 2

From the Molecular Stark Effect to a Stark Decelerator

Abstract

A Stark decelerator can be defined as an apparatus that uses time-varying inhomogeneous electric fields to decelerate a molecular beam pulse. It exploits the molecular Stark effect to extract energy from the molecules in the pulse. In this chapter we give an extensive treatment of the Stark effect, where special attention is paid to the OH radical in its $X^2\Pi$ state, which is the model system used in the various simulations throughout this thesis.

Next, we will describe how a Stark decelerator produces cold molecules in practice. Stark deceleration always starts from a molecular beam pulse whose production technique, the free jet expansion, will be considered in more detail. The expansion results in an internally cold beam pulse, which implies a small velocity spread and molecules predominantly in a single quantum state. After the expansion, the beam pulse moves at a high velocity in the lab frame. Stark deceleration provides a method to transfer the favorable properties of a molecular beam pulse to very low velocities in the lab frame. We will describe an experimental setup that is used in deceleration experiments of OH radicals.

This chapter should be seen as a theoretical and experimental background for Chapter 3, where the Stark deceleration dynamics is treated, the main topic of this thesis.

2.1 Molecular Stark Effect

2.1.1 Introduction

Molecules represent very complicated and rich quantum systems. The general expression for the non-relativistic molecular Hamiltonian in the coordinate representation is given by

$$\begin{aligned}\hat{H} &= -\frac{\hbar^2}{2}\sum_\alpha \frac{\nabla_\alpha^2}{M_\alpha} - \frac{\hbar^2}{2m_e}\sum_i \nabla_i^2 + \sum_\alpha \sum_{\beta>\alpha} \frac{Z_\alpha Z_\beta e^2}{4\pi\epsilon_0 r_{\alpha\beta}} - \sum_\alpha \sum_i \frac{Z_\alpha e^2}{4\pi\epsilon_0 r_{i\alpha}} + \sum_i \sum_{j>i} \frac{e^2}{4\pi\epsilon_0 r_{ij}} \\ &\equiv \hat{T}_N + \hat{T}_e + \hat{V}_{NN} + \hat{V}_{eN} + \hat{V}_{ee} \end{aligned} \tag{2.1}$$

where the Greek subscripts refer to the nuclei of the molecule, the Roman subscripts refer to the electrons and Z designates the number of protons in a certain nucleus. In the second line of eq. (2.1) we defined the nuclear kinetic energy, the electronic kinetic energy, the nucleus-nucleus repulsion energy, the electron-nucleus attraction energy and the electron-electron repulsion energy. The corresponding time-independent Schrödinger equation needed for calculating the energy level structure of a molecule

$$\hat{H}|\psi\rangle = E|\psi\rangle \tag{2.2}$$

is easier written down than solved. Still, by using appropriate approximations and applying symmetry considerations great progress has been made in solving eq. (2.2) and addressing the physical processes behind the complicated energy spectra obtained from molecular spectroscopy. Extensive treatments of this topic on different levels can be found in several text books [54, 55].

The first step in these treatments is always to apply the Born-Oppenheimer separation. This approximation exploits the fact that the electrons move much faster than the nuclei, so that in order to solve for the electronic structure we can treat the nuclei as fixed in space. This leads to the purely electronic Schrödinger equation

$$\hat{H}_{el}|\psi_{el}\rangle = E_{el}|\psi_{el}\rangle \tag{2.3}$$

where $\hat{H}_{el}$ is given by

$$\hat{H}_{el} = \hat{T}_e + \hat{V}_{eN} + \hat{V}_{ee} \tag{2.4}$$

and where eqs. (2.3) and (2.4) depend only parametrically on the positions of the nuclei $\mathbf{r_\alpha}$.

Since the electrons in the molecule adjust their positions instantaneously to those of the nuclei, their total electronic energy $E_{el}(\mathbf{r}_\alpha)$ acts effectively as a potential for nuclear motion. This leads to a total nuclear potential energy $U(\mathbf{r}_\alpha)$

$$U(\mathbf{r}_\alpha) = E_{el}(\mathbf{r}_\alpha) + V_{NN}(\mathbf{r}_\alpha) \tag{2.5}$$

resulting in the nuclear Schrödinger equation

$$\hat{H}_N|\chi_N\rangle = E_N|\chi_N\rangle \tag{2.6}$$

with $\hat{H}_N$ given by

$$\hat{H}_N = \hat{T}_N + U(\mathbf{r}_\alpha) \tag{2.7}$$

From eqs. (2.6) and (2.7) it follows that the molecule will not only perform rotational and translational motion like any rigid body, but will also perform vibrational motion under the potential $U(\mathbf{r}_\alpha)$. Translational motion is usually not considered since it just pertains to an overall shift of the internal energy level structure.

Finally, the total molecular wavefunction after the Born-Oppenheimer separation becomes

$$|\psi\rangle = |\psi_{el}\rangle|\chi_N\rangle = |\psi_{el}\rangle|\chi_{rot}\rangle|\chi_{vibr}\rangle \tag{2.8}$$

where in the last step we also separated the rotational motion of the nuclei from the vibrational motion.

As a result of its rich internal structure, a molecule can give rise to an asymmetric charge distribution, leading to a body-fixed electric dipole moment $\boldsymbol{\mu}$. The application of an external electric field $\boldsymbol{\varepsilon}$ to such a polar molecule leads to the molecular Stark effect, whose treatment requires an additional term in the molecular Hamiltonian

$$\hat{H}_{Stark} = -\boldsymbol{\mu} \cdot \boldsymbol{\varepsilon} \tag{2.9}$$

complicating the situation even more. The electric fields applied in deceleration experiments are relatively weak, so they leave the electronic and vibrational energy level structures of the molecule intact. Furthermore, at the used field strengths the induced dipole moment due to the polarizability of the molecule can be neglected. What remains is the influence of the Stark interaction term (2.9) on the rotational energy level structure.

2.1.2 Rotational Energy Level Structure of a Rigid Rotor

In order to accurately calculate the rotational energy level structure of a molecule one has to deal with angular momentum in all its entirety. Molecules possess rotational angular momentum $\mathbf{R}$, electronic orbital angular momentum $\mathbf{L}$, electronic spin $\mathbf{S}$ and nuclear spin $\mathbf{I}$, that can all couple to each other in various ways. Taking all this into account leads to a very detailed description of the observed rotational spectra, but for a general understanding of the Stark effect such an extensive description is not necessary.

Therefore we will start by treating the molecule as a rigid rotor leaving out the electronic and nuclear angular momenta. The total angular momentum $\mathbf{J}$ of the molecule is then equal to the rotational angular momentum $\mathbf{R}$ leading to the following rotational Hamiltonian

$$\hat{H}_{rot} = A\hat{R}_a^2 + B\hat{R}_b^2 + C\hat{R}_c^2 = A\hat{J}_a^2 + B\hat{J}_b^2 + C\hat{J}_c^2 \tag{2.10}$$

where the subscripts a, b, c denote the projections of the angular momentum operators $\hat{R}$, $\hat{J}$ on the three principal axes of inertia (a, b, c) and where A, B and C designate the rotational constants that are inversely proportional to the principal moments of inertia.

Symmetric Tops

When at least two of the rotational constants are equal, we speak of a symmetric top molecule, whose quantum mechanical treatment has nice analytic properties. Here we will assume an oblate top, i.e. $A = B < C$, but keep in mind that the treatment of a prolate top, $A < B = C$, goes along the same lines.

In treating the symmetric top, two frames naturally occur: a body fixed molecular frame (x, y, z) and a space fixed laboratory frame (X, Y, Z). The orientation of the molecular system relative to the laboratory system is described by three Euler angles θ, ϕ and χ, which define a transformation matrix linking an arbitrary vector $\mathbf{A}$ in the molecular frame to the laboratory frame

$$A_F = \sum_{g=x,y,z} \Phi_{Fg} A_g$$

where $F \in \{X, Y, Z\}$ and Φ_{Fg} are the elements of the so called direction cosine matrix [56].

The body-fixed axes (x, y, z) of the symmetric top molecule are most suitably chosen to coincide with its principal axes of inertia (a, b, c). Furthermore, when $A = B$, it is convenient to identify the z axis with the c axis, resulting in the following expression for the rotational Hamiltonian

$$\hat{H}_{rot} = A\hat{J}^2 - (A - C)\hat{J}_z^2 \tag{2.11}$$

which is seen to commute with $\hat{J}^2$, $\hat{J}_z$ and $\hat{J}_Z$ [54]. As a result, a basis of simultaneous eigenfunctions can be found defined by the following eigenvalue equations

$$\hat{J}^2|JKM\rangle = J(J+1)|JKM\rangle \tag{2.12}$$

$$\hat{J}_Z|JKM\rangle = M|JKM\rangle \tag{2.13}$$

$$\hat{J}_z|JKM\rangle = K|JKM\rangle \tag{2.14}$$

$$\hat{H}_{rot}|JKM\rangle = E|JKM\rangle = [AJ(J+1) - (A-C)K^2]|JKM\rangle \tag{2.15}$$

where for convenience we set $\hbar = 1$. The rotational energy levels of a symmetric top given by eq. (2.15) are seen to be degenerate in M. The symmetric top wavefunctions take the following form

$$|JKM\rangle = \left[\frac{2J+1}{8\pi^2}\right]^{1/2} e^{iM\phi} e^{iK\chi} d^J_{MK}(\theta) \tag{2.16}$$

where $d^J_{MK}(\theta)$ can be expressed in terms of Jacobi polynomials [56].

Asymmetric Tops

The asymmetric top does not allow a complete analytic description as the symmetric top does. Still, with the help of the symmetric top basis set $|JKM\rangle$ a general procedure for solving the asymmetric top can be formulated. The first step is to rewrite the rotational Hamiltonian

$$\begin{aligned}\hat{H}_{rot} &= A\hat{J}_a^2 + B\hat{J}_b^2 + C\hat{J}_c^2 = A\hat{J}_x^2 + B\hat{J}_y^2 + C\hat{J}_z^2 \\ &= \left(\frac{A+B}{2}\right)\hat{J}^2 + \left(C - \frac{A+B}{2}\right)\hat{J}_z^2 + \left(\frac{A-B}{4}\right)[(\hat{J}^+)^2 + (\hat{J}^-)^2] \end{aligned} \tag{2.17}$$

where in the first line we identified the axes of the molecular frame (x, y, z) with the principal axes of inertia (a, b, c) and in the second line we rewrote $\hat{H}_{rot}$ in terms of the raising and lowering operators

$$\hat{J}^{\pm} = \hat{J}_x \pm i\hat{J}_y \tag{2.18}$$

These operators have the following effect on the symmetric top eigenfunctions

$$\hat{J}^{\pm}|JKM\rangle = [J(J+1) - K(K \mp 1)]^{1/2}|JK \mp 1M\rangle \tag{2.19}$$

where it is noted that $\hat{J}^-$ is the raising operator and $\hat{J}^+$ is the lowering operator in the molecular frame. This is due to the anomalous commutation relation

$$[\hat{J}_x, \hat{J}_y] = -i\hat{J}_z \tag{2.20}$$

which is the result of the way the body fixed frame was introduced with respect to the lab frame [54].

With the use of eqs. (2.12), (2.14) and (2.19) it is straightforward to evaluate $\hat{H}_{rot}$ in the symmetric top basis set $|JKM\rangle$. Because of the $(\hat{J}^+)^2$ and $(\hat{J}^-)^2$ terms, $\hat{H}_{rot}$ is not diagonal in this set. By diagonalizing $\hat{H}_{rot}$ one obtains the rotational energy level structure and the eigenfunctions of the asymmetric top. In general, this can only be done numerically.

2.1.3 Applying an External Electric Field

The rotational wavefunction of a polar molecule contains information about the orientation of the molecular axes (and therefore the dipole moment) with respect to the lab frame. In the absence of an electric field there is no preferred direction in space, which is expressed by the degeneracy in M of the field-free rotational energy levels. Applying an external electric field to a polar molecule introduces a preferred direction in space, and we will show in this paragraph that, as a result, the degeneracy in M is lifted.

When the applied electric field $\boldsymbol{\varepsilon}$ is constant in magnitude and is directed along the Z axis in the lab frame, eq. (2.9) becomes

$$\hat{H}_{Stark} = -\varepsilon \sum_{i=x,y,z} \mu_i \Phi_{Zi} \tag{2.21}$$

where Φ_{Zi} are the direction cosines of the molecular x, y, z axes with reference to the space-fixed Z axis.

Symmetric Tops

Because of symmetry reasons, symmetric top molecules for which $A = B$ only have a dipole component along the principal c axis, which can be conveniently identified with the molecular z axis. Then $\mu_z = \mu$ and $\mu_x = \mu_y = 0$, which means that the Stark interaction term is simply given by

$$\hat{H}_{Stark} = -\mu\varepsilon\Phi_{Zz} = -\mu\varepsilon\cos\theta \tag{2.22}$$

The matrix elements of the $\cos\theta$ operator can be found in many textbooks, e.g. ref. [57]. The only nonzero matrix elements $\langle J'K'M'|\cos\theta|JKM\rangle$ are given by the selection rules $M = M'$, $K = K'$ and $J = J', J' \pm 1$. They can be evaluated using the following expressions

$$\langle JKM|\hat{H}_{Stark}|JKM\rangle = -\mu\varepsilon\langle JKM|\cos\theta|JKM\rangle = -\frac{KM}{J(J+1)}\mu\varepsilon \tag{2.23}$$

$$\langle JKM|\hat{H}_{Stark}|J+1KM\rangle = -\frac{\mu\varepsilon}{J+1}\sqrt{\frac{[(J+1)^2-K^2][(J+1)^2-M^2]}{(2J+1)(2J+3)}} \tag{2.24}$$

Because of eq. (2.24), the Hamiltonian $\hat{H}_{rot} + \hat{H}_{Stark}$ will not be diagonal. In order to obtain the full rotational energy level structure of a symmetric top under the influence of an applied electric field, $\hat{H}_{rot} + \hat{H}_{Stark}$ has to be diagonalized. This can be done numerically, taking as many J components into account as the accuracy of the calculation requires.

When the electric field strengths are (relatively) low, like in deceleration experiments, the mixing of different J levels is small. When furthermore $K, M \neq 0$, the Stark shift is dominated by eq. (2.23) and to a good approximation the influence of eq. (2.24) can be neglected. Eq. (2.23) is said to give rise to the so called *first-order Stark effect*. The first-order Stark effect is seen to remove the M degeneracy of the field free rotational levels as given by eq. (2.15). Upon application of an external electric field, each field free level splits into $2J + 1$ different components with a splitting linear in ε, K and M.

Figure 2.1 shows a vector diagram that reveals the geometric interpretation of the first order Stark effect for a symmetric top in a $|JKM\rangle$ state. The projection of the total angular momentum $\mathbf{J}$ on the Z axis has the constant value M, which pertains to the precessional motion of $\mathbf{J}$ about the Z axis. Furthermore, the projection of $\mathbf{J}$ on the molecular z axis, $\mathbf{J}_z$, has the constant value K, which in the lab frame is expressed by the precessional motion of $\mathbf{J}_z$ about $\mathbf{J}$. Now, the Stark effect is the interaction of the dipole moment $\boldsymbol{\mu}$ (along z) with the electric field $\boldsymbol{\varepsilon}$ (along Z). From the vector diagram it is clear that on average only the projection of $\boldsymbol{\mu}$ on $\mathbf{J}$ interacts with $\boldsymbol{\varepsilon}$. As a result, the first-order Stark effect can be readily obtained geometrically

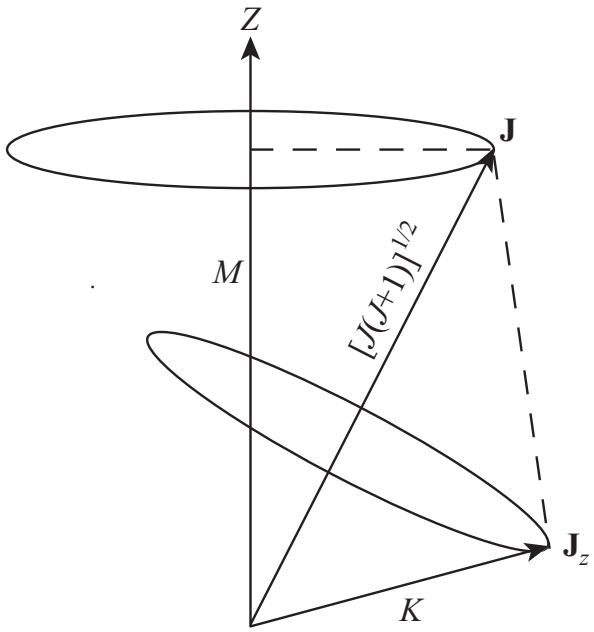

Figure 2.1: *Vector diagram allowing a geometric interpretation of the first order Stark effect for a symmetric top molecule in a $|JKM\rangle$ state. The projection of the total angular momentum vector* **J** *of length $[J(J+1)]^{1/2}$ on the space-fixed Z axis has the constant value M, whereas the projection of* **J** *on the molecular z axis, $\mathbf{J}_z$, has the constant value K. The Stark effect is the interaction of the dipole moment $\boldsymbol{\mu}$ along z with the electric field $\boldsymbol{\varepsilon}$ along Z. On average only the projection of $\boldsymbol{\mu}$ on* **J** *interacts with $\boldsymbol{\varepsilon}$.*

from Fig. 2.1

$$W_{Stark} = -\mu\varepsilon\cos(\mathbf{J}_z, \mathbf{J})\cos(\mathbf{J}, Z) = -\mu\varepsilon\frac{MK}{J(J+1)} \tag{2.25}$$

From eq. (2.25) it follows that for states with $MK > 0$ the eigenenergy decreases with increasing field strength. In an inhomogeneous field a molecule in such a state will seek regions of maximum field strength, where its eigenenergy is minimal. Therefore these states are called *high-field seeking states*. For states with $MK < 0$ the eigenenergy increases with increasing field strength. A molecule in such a state will seek regions of minimum field strength. Therefore, these states are called *low-field seeking states*.

Upon increasing the field strength, the coupling of the rotational levels, eq. (2.24), becomes more dominant, leading to second- and higher-order Stark shifts. Eventually, the interaction with the field will become so strong that the molecule no longer rotates freely in space, but can only librate about the electric field direction. These states are therefore called pendular states [58, 59]. All pendular states are high field seeking.

Asymmetric Tops

The Stark effect for asymmetric tops can be treated similarly as for symmetric tops, provided

that the dipole moment lies along one of the principal axes of the molecule, which is mostly the case. This axis is then conveniently chosen to be the molecular z axis and eq. (2.22) still holds. The operator $\hat{H}_{rot} + \hat{H}_{Stark}$ can be readily evaluated in the symmetric top basis set using eqs. (2.12), (2.14), (2.19), (2.23) and (2.24). Diagonalization of the resulting matrix gives the rotational energy level structure of an asymmetric top in an electric field. As for the symmetric top, the Stark effect removes the M degeneracy of the field free lines and split them into $2J+1$ different components.

When the body-fixed dipole moment is not along one of the principal axes of the molecule a choice has to be made. Either one chooses the molecular z axis along the dipole moment, or one chooses the molecular z axis along one of the principal axes. In the first case, eq. (2.22) still holds, but eq. (2.17) is not valid anymore. In the second case, eq. (2.17) still holds, but eq. (2.22) is not valid anymore. Which choice leads to the least cumbersome calculation depends on the specific molecule.

2.1.4 Rotational energy level structure of the OH radical in its $X^2\Pi$ state

So far, we neglected the electronic and nuclear angular momenta **L**, **S** and **I**. Taking these into account does not add additional insight into the origin of the Stark effect, but it does lead to a more accurate description of reality. In this paragraph a detailed discussion of the OH radical in its $X^2\Pi$ electronic ground state is given, since this molecule is used in the various simulations throughout this thesis. Furthermore, the treatment is an example for how to calculate molecular energy levels in general.

For a diatomic molecule, like OH, the rotational Hamiltonian is given by

$$\hat{H}_{rot} = B\mathbf{R}^2 = B(\mathbf{J} - \mathbf{L} - \mathbf{S})^2 \tag{2.26}$$

where B is the rotational constant and where we neglected the nuclear spin **I**, since its effect, the hyperfine structure, is too small to be of any importance for our purposes. Eq. (2.26) can be rewritten by introducing the following raising and lowering operators

$$\hat{L}^{\pm} = \hat{L}_x \pm i\hat{L}_y \quad \hat{S}^{\pm} = \hat{S}_x \pm i\hat{S}_y \tag{2.27}$$

giving

$$\begin{aligned} \hat{H}_{rot} &= B[\hat{J}^2 - 2\hat{J}_z\hat{S}_z + \hat{S}^2 - 2(\hat{J}_z - \hat{S}_z)\hat{L}_z + \hat{L}_z^2 - \hat{J}^+\hat{S}^- - \hat{J}^-\hat{S}^+] \\ &\quad -B[(\hat{J}^+ - \hat{S}^+)\hat{L}^- + (\hat{J}^- - \hat{S}^-)\hat{L}^+ - \frac{1}{2}(\hat{L}^+\hat{L}^- + \hat{L}^-\hat{L}^+)] \end{aligned} \tag{2.28}$$

where we also used eq. (2.19). In the calculation of the rotational energy levels, the second line of eq. (2.28) can be neglected to a first approximation. The first term of the second line,

containing $\hat{L}^-$, and the second term, containing $\hat{L}^+$, generate a small coupling between different electronic states. This results in a small effect called Λ-doubling, to which we will come back later. The last term does not couple different electronic states and does not depend on J. Its expectation value just shifts uniformly the rotational energy levels and is therefore ignored.

Since electrons are charged particles, their orbital motion $\mathbf{L}$ produces a magnetic field, which can interact with the spin of the electrons $\mathbf{S}$. This is called spin-orbit coupling and its effect can be substantial, certainly compared to the rotational Hamiltonian. Therefore it needs to be taken into account when calculating the rotational energy level structure. This can be done by introducing the following term

$$\hat{H}_{so} = \mathcal{A}\mathbf{L}\cdot\mathbf{S} = \mathcal{A}\hat{L}_z\hat{S}_z + \frac{1}{2}\mathcal{A}[\hat{L}^+\hat{S}^- + \hat{L}^-\hat{S}^+] \tag{2.29}$$

where $\mathcal{A}$ is the spin-orbit coupling constant and where the terms containing $L^\pm$ can again be neglected in first instance.

In order to solve the rotational energy level structure of a diatomic molecule we 'only' have to write the operator $\hat{H}_{rot} + \hat{H}_{so}$ in a suitable basis set and diagonalize it. The convenient separation of the molecular basis functions into an electronic, vibrational and rotational part was already discussed in the introduction to this chapter. It yields

$$|\psi_{el}\rangle|\chi_{vibr}\rangle|\chi_{rot}\rangle = |n\Lambda S\Sigma\rangle|v\rangle|J\Omega M\rangle \tag{2.30}$$

where the electronic state is also often referred to as $|n^{2S+1}\Lambda_\Omega\rangle$. The rotational set $|J\Omega M\rangle$ has already been introduced in Paragraph 2.1.2. Here we adopted the usual notation that in the case of a diatomic molecule the eigenvalue of $\hat{J}_z$ is labelled Ω rather than K. The electronic set $|n\Lambda S\Sigma\rangle$ and its labels are characterized by the following set of equations

$$\hat{L}_z|n\Lambda S\Sigma\rangle = \Lambda|n\Lambda S\Sigma\rangle \tag{2.31}$$

$$\hat{S}^2|n\Lambda S\Sigma\rangle = S(S+1)|n\Lambda S\Sigma\rangle \tag{2.32}$$

$$\hat{S}_z|n\Lambda S\Sigma\rangle = \Sigma|n\Lambda S\Sigma\rangle \tag{2.33}$$

$$\hat{S}^\pm|n\Lambda S\Sigma\rangle = [S(S+1) - \Sigma(\Sigma\pm 1)]^{1/2}|n\Lambda S\Sigma\pm 1\rangle \tag{2.34}$$

where n distinguishes between states for which all other electronic quantum numbers are equal.

For the $X^2\Pi$ electronic ground state of the OH radical, we have four basis functions for each rovibronic level, namely

$$|X^2\Pi_{\pm 3/2}vJM\rangle = |X,\Lambda=\pm 1,S=\frac{1}{2},\Sigma=\pm\frac{1}{2}\rangle|v\rangle|\Omega=\pm\frac{3}{2}JM\rangle \tag{2.35}$$

$$|X^2\Pi_{\pm 1/2}vJM\rangle = |X,\Lambda=\pm 1,S=\frac{1}{2},\Sigma=\mp\frac{1}{2}\rangle|v\rangle|\Omega=\pm\frac{1}{2}JM\rangle \tag{2.36}$$

By making linear combinations, we can create a convenient, symmetrized basis set

$$|X^2\Pi_{3/2}vJMe/f\rangle = \frac{|X^2\Pi_{3/2}vJM\rangle \pm |X^2\Pi_{-3/2}vJM\rangle}{\sqrt{2}} \quad (2.37)$$

$$|X^2\Pi_{1/2}vJMe/f\rangle = \frac{|X^2\Pi_{1/2}vJM\rangle \pm |X^2\Pi_{-1/2}vJM\rangle}{\sqrt{2}} \quad (2.38)$$

where the upper (lower) sign corresponds to $e(f)$ parity [54]. By using eqs. (2.12), (2.14), (2.19), (2.31)-(2.34) $\hat{H}_{rot} + \hat{H}_{so}$ can be evaluated in this symmetrized basis set, which gives the following result (neglecting the terms containing $\hat{L}^{\pm}$)

$$\hat{H}_{rot} + \hat{H}_{so} = \begin{pmatrix} H' & 0 \\ 0 & H' \end{pmatrix}$$

where each H' block corresponds to a different parity e/f and is given by

$$H' = \begin{pmatrix} -\frac{1}{2}\mathcal{A} + B\left[J(J+1) + \frac{1}{4}\right] & -B\left[J(J+1) - \frac{3}{4}\right]^{1/2} \\ -B\left[J(J+1) - \frac{3}{4}\right]^{1/2} & \frac{1}{2}\mathcal{A} + B\left[J(J+1) - \frac{7}{4}\right] \end{pmatrix}$$

where the first row/column corresponds to $|X^2\Pi_{1/2}vJMe/f\rangle$, while the second row/column corresponds to $|X^2\Pi_{3/2}vJMe/f\rangle$. Diagonalization of this matrix leads to a quadratic equation, whose solution is

$$E^{\pm} = B[(J - \frac{1}{2})(J + \frac{3}{2}) \pm \frac{1}{2}X] \quad (2.39)$$

where

$$X = \sqrt{4(J + \frac{1}{2})^2 + Y(Y-4)} \quad (2.40)$$

$$Y = \frac{\mathcal{A}}{B} \quad (2.41)$$

Note that each eigenvalue is doubly degenerate with respect to e/f parity. The corresponding eigenfunctions are given by

$$|X^2\Pi E^- vJMe/f\rangle = c_1(J)|X^2\Pi_{1/2}vJMe/f\rangle + c_2(J)|X^2\Pi_{3/2}vJMe/f\rangle \quad (2.42)$$

$$|X^2\Pi E^+ vJMe/f\rangle = -c_2(J)|X^2\Pi_{1/2}vJMe/f\rangle + c_1(J)|X^2\Pi_{3/2}vJMe/f\rangle \quad (2.43)$$

where

$$c_1(J) = \sqrt{\frac{X + Y - 2}{2X}} \quad (2.44)$$

$$c_2(J) = \sqrt{\frac{X - Y + 2}{2X}} \quad (2.45)$$

Eqs. (2.42)-(2.45) reveal that $\hat{H}_{rot}$ mixes levels with different Ω, which is therefore not a good quantum number anymore.

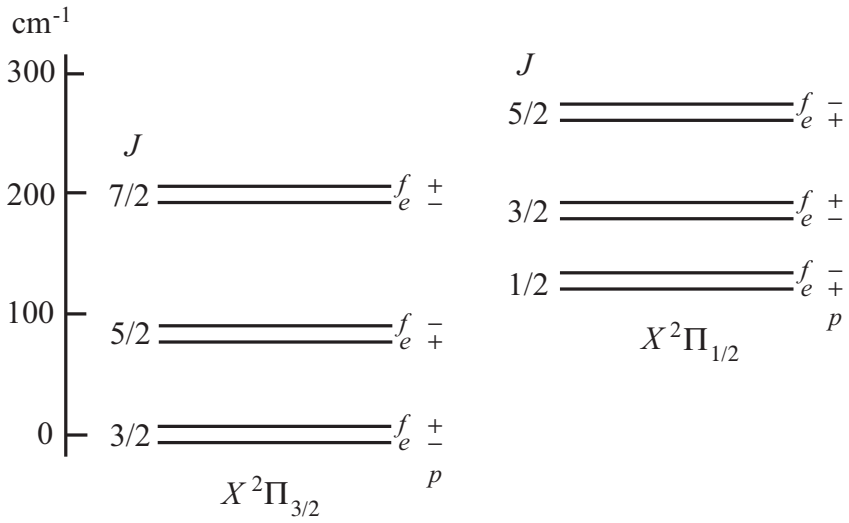

Figure 2.2: *Energy level diagram showing the lowest rotational levels of the vibronic groundstate $X^2\Pi, v = 0$ of the OH radical. For reasons of clarity the Λ-doublet splitting of each rotational level is largely exaggerated. Furthermore, the e/f parity and the total parity p corresponding to each energy level are indicated.*

So far the discussion has been very general and it is valid for any diatomic molecule in a $^2\Pi$ state. For the specific case of OH, $B = 18.515$ cm^{-1} and $\mathcal{A} = -139.73$ cm^{-1} [60]. Since $|\mathcal{A}| \gg |B|$, OH is characterized by a Hund's case (a) coupling scheme [54]. As a result, the mixing in eqs. (2.42)-(2.45) is small and Ω is almost a good quantum number. Furthermore, since $\mathcal{A} < 0$, $|X^2\Pi_{3/2}, v = 0, J = 3/2, M, e/f\rangle$ is seen to be the rovibronic groundstate.

Up to now, the terms containing $\hat{L}^{\pm}$ in eqs. (2.28) and (2.29) have been neglected. These terms couple the $X^2\Pi$ state weakly to other electronic states differing by one unit of Λ. Taking this coupling into account results in a small effect, that lifts the degeneracy in e/f parity and splits each energy level in eq. (2.39) into two components. This is called Λ-doubling. For a $^2\Pi$ state no simple analytic expression for Λ doubling exists. For OH, which is a Hund's case (a) molecule, the Λ splitting in the $^2\Pi_{1/2}$ levels varies linearly in J, whereas the splitting in the $^2\Pi_{3/2}$ levels varies with the third power of J [56]. The resulting splitting in the ground state of OH is very small, only 0.05 cm^{-1} [61]. An energy level diagram showing the lowest rotational levels of the vibronic ground state of the OH radical, including Λ-doubling, is shown in Figure 2.2.

2.1.5 Stark Effect of the OH Radical in its $X^2\Pi$ State

The dipole moment of a diatomic molecule is always directed along the internuclear axis, which can be conveniently chosen as the molecular z axis. Upon application of a constant electric field in the Z direction, $\hat{H}_{Stark}$ is given by eq. (2.22). The nonzero matrix elements of the $\hat{H}_{stark}$

operator in the symmetric top basis $|JKM\rangle$ were given by eqs. (2.23) and (2.24), where we remember that for diatomics K is replaced by Ω.

For the OH radical, the mixing in eqs. (2.42)-(2.45) is small and the eigenfunctions of $\hat{H}_{rot} + \hat{H}_{so}$ are to a good approximation given by $|X^2\Pi_\Omega vJMe/f\rangle$. The degeneracy of the corresponding energy levels in e/f parity is lifted due to Λ doubling, causing a small splitting of each rotational level into two levels separated by E_Λ.

From eqs. (2.23), (2.24), (2.35)-(2.38) the non-zero matrix elements of $\hat{H}_{Stark}$ in the $|X^2\Pi_\Omega vJMe/f\rangle$ basis are readily derived. For the first-order Stark effect

$$\langle X^2\Pi_\Omega vJMf/e|\hat{H}_{Stark}|X^2\Pi_\Omega vJMe/f\rangle = -\frac{\Omega M}{J(J+1)}\mu\varepsilon \tag{2.46}$$

which is seen to mix levels with different e/f parity. For the second-order Stark effect

$$\langle X^2\Pi_\Omega vJMe/f|\hat{H}_{Stark}|X^2\Pi_\Omega vJ+1Me/f\rangle = -\frac{\mu\varepsilon}{J+1}\sqrt{\frac{[(J+1)^2-\Omega^2][(J+1)^2-M^2]}{(2J+1)(2J+3)}} \tag{2.47}$$

At the electric field strengths used in deceleration experiments, the second-order Stark effect may be neglected and for the rovibronic groundstate $|X^2\Pi_{3/2}, v=0, J=3/2, M, e/f\rangle$ the Stark matrix becomes

$$\hat{H}_{Stark} = \begin{pmatrix} -E_\Lambda/2 & -\mu\varepsilon\frac{M\Omega}{J(J+1)} \\ -\mu\varepsilon\frac{M\Omega}{J(J+1)} & E_\Lambda/2 \end{pmatrix}$$

where we added the effect of the Λ doubling along the diagonal. Note that the upper level of the Λ doublet corresponds to f parity [62]. The Stark shift W_{Stark} of the ground state Λ doublet levels is given by

$$W_{Stark} = \pm\sqrt{\left(\frac{E_\Lambda}{2}\right)^2 + \left(\mu\varepsilon\frac{M\Omega}{J(J+1)}\right)^2} \mp \frac{E_\Lambda}{2} \tag{2.48}$$

and is shown in Figure 2.3. For very low field strengths, $\epsilon \approx 0$, eq. (2.48) yields

$$W_{Stark} \approx \pm\mu^2\varepsilon^2\frac{M^2\Omega^2}{J^2(J+1)^2E_\Lambda} \tag{2.49}$$

which means an initial quadratic rise as a function of the field strength. But as the field increases, the Λ doubling becomes negligibly small and the Stark shift is, to an excellent approximation, linear in field strength, cf. Fig. 2.3.

To conclude we stress that applying an electric field to a polar molecule introduces a preferred direction in space, lifts the degeneracy in M and mixes states with opposite parity. As a result, the *space fixed* dipole moment μ_Z has a non-zero expectation value

$$\langle\mu_Z\rangle = \mu\langle\cos\theta\rangle \neq 0 \tag{2.50}$$

which means that the Stark effect gives rise to the *orientation* of molecules.

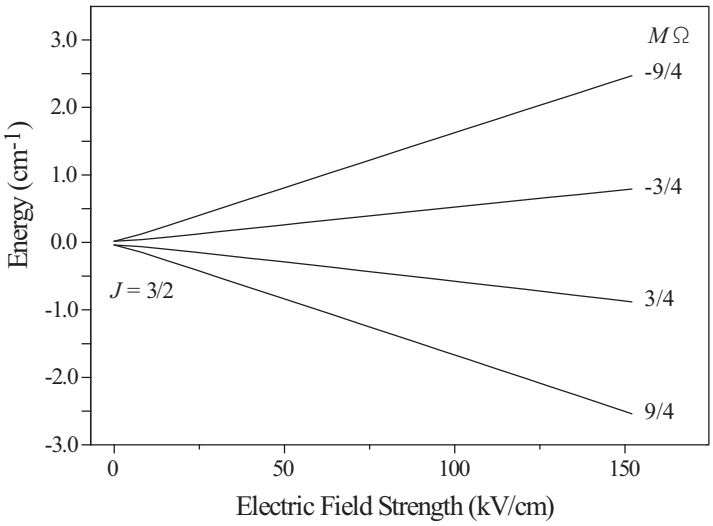

Figure 2.3: *Stark shift of the Λ-doublet levels of the* $X^2\Pi, v = 0, J = 3/2$ *rovibronic ground state of the OH radical as a function of the electric field strength.*

2.2 Stark Decelerator

As mentioned in the introduction, during the last years several techniques have been developed to produce cold molecules. Some of them, including Stark deceleration, are based on deceleration of a molecular beam pulse. In the next paragraph we will see that a molecular beam pulse, formed by a free jet expansion, is already internally cold, but moves at a high velocity in the lab frame. Stark deceleration uses the molecular Stark effect to slow down the beam pulse and to produce cold molecules in the lab frame.

2.2.1 Free-jet Molecular Beam

By a molecular beam we understand an ensemble of molecules having (nearly) the same velocity vectors. The *free-jet molecular beam* arises from a supersonic jet expansion. It is produced by seeding the molecules in a so-called carrier gas, which is kept at high pressure P_0 in a container. Next the gas is expanded into a region of low pressure P_V (typically vacuum). This is shown in Figure 2.4. Near the opening of the container, called the nozzle, the molecules are bombarded by particles only from one side, resulting in an accelerated motion towards the vacuum. In the expanding gas, the faster particles keep on colliding with the slower ones creating a much narrower velocity distribution than originally in the container. A pulsed molecular beam is obtained by opening and closing the container with a certain frequency. The free-jet expansion can be described in terms of a hydrodynamic flow of an ideal gas.

We start by introducing a central quantity in our description, namely the Mach number

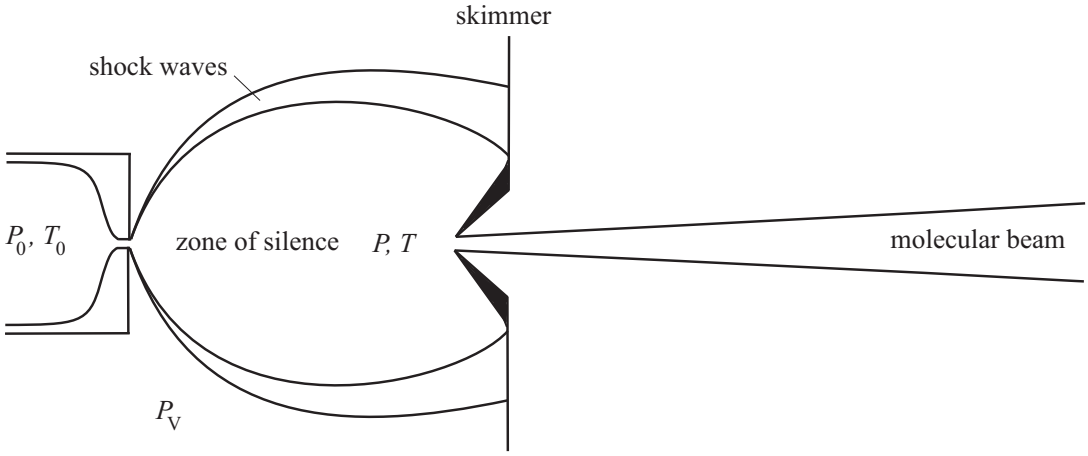

Figure 2.4: *Schematic view of a free jet expansion resulting in a molecular beam. Molecules are seeded in a carrier gas, that is kept at a pressure P_0 and a temperature T_0 in a container. The pressure of the background is P_V. As the gas expands into the vacuum it obtains a supersonic velocity, which leads to the formation of a so-called zone of silence, where there is no information available about any external boundary condition. In order to still satisfy the boundary conditions, shock waves have to occur. Also shown are the pressure P and the temperature T inside the zone of silence, which vary with position in the jet. The final molecular beam is extracted from the zone of silence by placing a skimmer that only selects the centerline beam.*

M, which is defined as the ratio of the local flow velocity u to the local speed of sound a

$$M = \frac{u}{a} \tag{2.51}$$

For $M < 1$, $M = 1$ and $M > 1$, we speak of subsonic, sonic and supersonic flow. At the pressure ratios P_0/P_V typically used in molecular beam experiments, the flow exits the nozzle with a supersonic velocity. This means that any information inside the flow, which is transported at the speed of sound, moves slower than the flow itself. As a result, a central region inside the expansion arises, called the zone of silence, where no information about any external boundary conditions is available. From this region the molecular beam is extracted.

The zone of silence can be described as a region of isentropic flow of an ideal gas, which means neglecting viscous and heat conduction effects. These are good approximations for high-speed flow, when the characteristic flow time is short compared to the time scales at which such non-equilibrium processes take place [63]. Since the pressure P is the relevant quantity in the expansion, the jet is most conveniently described by its enthalpy $H(S, P)$. For an isentropic process the enthalpy is given by

$$dH = TdS + VdP = VdP = dW \tag{2.52}$$

where V is the volume, S is the entropy and W the flow work done by the expanding gas. As the gas is subject to a negative pressure gradient, it performs negative work, which can also be

construed as positive work done on the gas by the applied pressure difference. As a result, the kinetic energy of the gas flow increases. Using equation (2.52), the conservation of energy can be expressed as

$$-\Delta h = h_0 - h = -\Delta w = \frac{1}{2}u^2 \tag{2.53}$$

where h, h_0 and w are the enthalpy, initial enthalpy and the work per unit mass. The gas is assumed to have a negligible initial flow velocity.

The equation of state for an ideal gas is given by

$$PV = NkT \tag{2.54}$$

where N is the number of molecules and k the Boltzmann constant. For an ideal gas several useful equations hold

$$dh = c_P dT \tag{2.55}$$

$$c_P - c_V = k/m \tag{2.56}$$

$$c_P = \frac{\gamma k}{(\gamma - 1)m} \tag{2.57}$$

where c_P and c_V are the heat capacities at constant pressure and volume per unit mass, and m is the mass of the atom or molecule in the gas. γ is called the Poisson coefficient and is given by

$$\gamma \equiv c_P/c_V = 1 + 2/D \tag{2.58}$$

where the last step is valid for an ideal gas whose particles have D degrees of freedom; for atoms $\gamma = 5/3$, whereas for diatomics $\gamma = 7/5$. For mixtures a weighted average of the mass, heat capacities and the Poisson coefficient has to be used. A typical mixture for a molecular beam contains about 1 % molecules and the rest carrier gas.

Using eqs. (2.52), (2.54), (2.55) and (2.57) it is easy to show that for an ideal, isentropic expansion

$$P/P_0 = (T/T_0)^{\gamma/(\gamma-1)} \tag{2.59}$$

$$\rho/\rho_0 = n/n_0 = (T/T_0)^{1/(\gamma-1)} \tag{2.60}$$

that shows how temperature, pressure, mass density ρ and number density n are related to each other in the flow. Furthermore, by combining eqs. (2.53), (2.55) and (2.57) we obtain

$$h_0 - h = \frac{\gamma k}{(\gamma - 1)m}(T_0 - T) = \frac{1}{2}u^2 \tag{2.61}$$

which allows us to calculate the limiting behavior of the flow velocity as $T \to 0$

$$\lim_{T\to 0} u \equiv u_\infty = \left[\frac{2\gamma k T_0}{(\gamma - 1)m}\right]^{1/2}$$

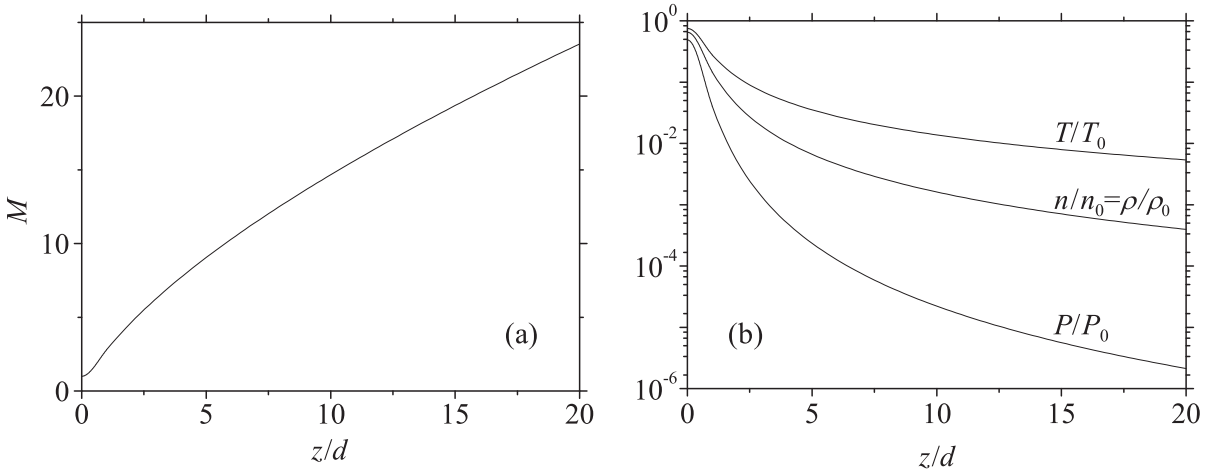

Figure 2.5: *Behavior of (a) the Mach number M, and (b) the pressure P, the number density n, the mass density ρ and the temperature T as a function of their position z along the centerline in the jet for a typical seeded molecular beam ($\gamma \approx 5/3$); d is the diameter of the nozzle.*

Using the expression for the velocity of sound a in an ideal gas [64]

$$a = (\gamma kT/m)^{1/2} \tag{2.62}$$

eq. (2.61) can be rewritten in a more convenient form

$$T_0/T = 1 + \frac{1}{2}(\gamma - 1)M^2 \tag{2.63}$$

Eqs. (2.59), (2.60) and (2.63) show that the temperature, pressure and density are directly related to the Mach number. Hence, if M can be determined as an explicit function of position, then all thermodynamic quantities are readily computed in the free jet. The determination of $M(\mathbf{r})$ has to be done numerically, for example by integrating the conservation laws (mass, momentum, energy) using the Method of Characteristics (MOC) [63]. No analytic expression exists, but the functional behavior of M along the centerline can be fitted by

$$M(0, z) = z^{\gamma-1}[C_1 + C_2 z^{-1} + C_3 z^{-2} + C_4 z^{-3}] \tag{2.64}$$

where C_1, C_2, C_3 and C_4 are fitting parameters. Note that this expression diverges when $z \to 0$. Therefore, for $z \approx 0$, the behavior is fitted by

$$M(0, z) = 1 + Az^2 + Bz^3 \tag{2.65}$$

where A and B are again fitting parameters. The total behavior of $M(0, z)$ is shown in Figure 2.5 a.

The behavior for large z, $M(0, z) \propto z^{\gamma-1}$ is readily understood from the conservation of mass. At large distances close to the centerline the streamlines are straight and seem to originate

from the same point. These lines describe a purely radial expansion, for which conservation of mass becomes

$$\rho u R^2 = const. \tag{2.66}$$

with R the radial distance. This yields

$$M(R) \propto R^{\gamma-1} \tag{2.67}$$

where we made use of eqs. (2.60), (2.63) and the approximations $u \approx u_\infty$,
$1 + \frac{1}{2}(\gamma - 1)M^2 \approx \frac{1}{2}(\gamma - 1)M^2$, which are valid for large R.

From the dependence of the Mach number M on z, we can evaluate the behaviour of the other thermodynamic quantities along the centerline of the flow field, where the result is shown in Figure 2.5 b.

The actual molecular beam is obtained by placing a small cone-shaped aperture, called the skimmer, into the zone of silence, thereby selecting only the centerline fraction (cf. Fig. 2.4). The final beam consists of molecules predominantly in their rovibronic ground state and is characterized by a small velocity spread as expressed by the low temperature, typically around 1 K (even temperatures of about 1 mK have been reached). Much lower temperatures are not attainable with this technique, since at some point the used idealizations break down. For example, due to the finite sized cross sections the gas runs out of collisions at a certain density. Thermal equilibrium cannot be maintained anymore and further expansion doesn't lead to additional cooling. Furthermore, at low temperatures the particles start to form clusters, releasing energy that heats the beam. The problem of cluster formation can be solved to some extent by using a noble gas as a carrier, which forms clusters only at very low temperatures.

To conclude, by using a free jet expansion molecular beams with translational temperatures of 1 K can be routinely produced at densities of $n = 10^{13}$ molecules/cm^3, where the molecules reside predominantly in their rovibronic ground state. The only thing that prevents the trapping of such molecules is their high mean velocity in the lab frame, typically 300 to 2000 m/s. So what we need, is a method to slow the molecules down. This is where the Stark decelerator comes in.

2.2.2 Principle of Stark Deceleration

Figure 2.6 shows a schematic picture of a Stark decelerator consisting of two field stages at three different moments in time. At t_1 and t_2 the left electrode pair is at high voltage, whereas the right electrode pair is grounded. This leads to a maximum electric field strength between the left electrode pair. Between t_2 and t_3 the voltages are abruptly switched. The high voltage

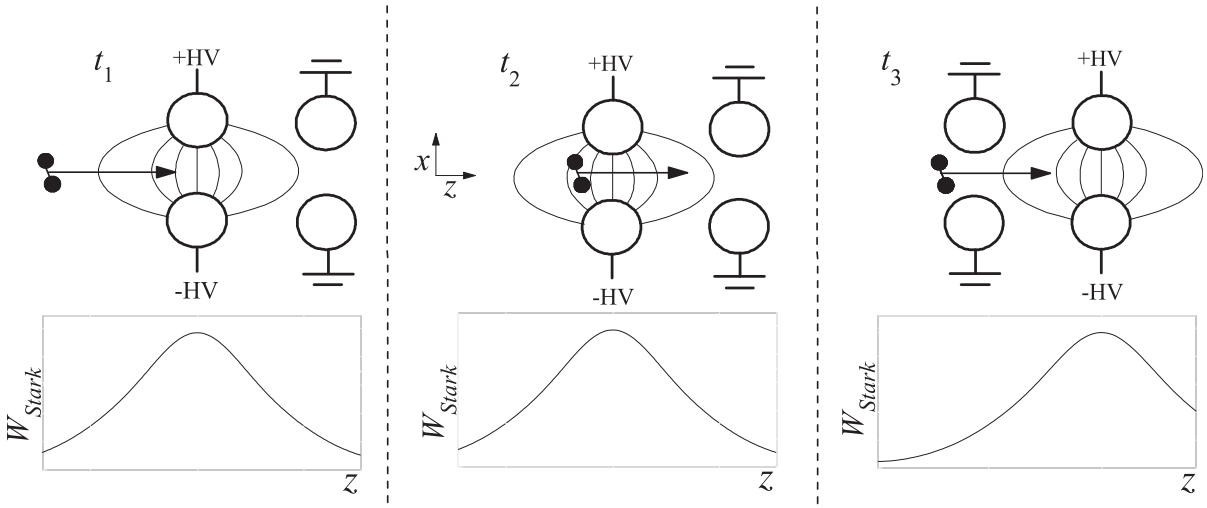

Figure 2.6: *Schematic picture of a two stage Stark decelerator at three different moments in time. At t_1 and t_2 the left electrode pair is at high voltage and the right pair is grounded, whereas at t_3 the right electrode pair is at high voltage and the left pair is grounded. At each moment in time also the Stark energy W_{Stark} of a low-field seeking molecule is shown as a function of the longitudinal coordinate z. As a low-field seeking molecule flies into the decelerator from the left, its Stark energy increases, which goes at the cost of its kinetic energy. By switching the fields between t_2 and t_3, the molecule doesn't regain its kinetic energy and has to fly into a region of increasing field strength again. Also shown is the transverse x direction.*

pair on the left becomes grounded, whereas the grounded pair on the right is put at high voltage. This leads to a maximum field strength between the right electrode pair. At each moment in time also the Stark energy of a low-field seeking molecule is shown as a function of its longitudinal coordinate z. In keeping with what we discussed in Paragraph 2.1.3, the eigenenergy of a low-field seeking state increases with increasing field strength.

As a low-field seeker flies into the decelerator from the left, its Stark energy increases, which happens at the cost of its kinetic energy. The Stark energy is seen to act as a potential energy and typically the molecule loses about 1% of its initial kinetic energy between t_1 and t_2. If we would do nothing between t_2 and t_3, the electric fields would remain unchanged and the low-field seeker would just regain its kinetic energy on the right side of the potential slope. But if we switch the field stages very fast between t_2 and t_3, so fast that the position of the molecule essentially doesn't change during switching, then the instantaneous velocity of the molecule at t_2 is not affected by the switching. As a result, the molecule will fly on without having regained its kinetic energy. Furthermore, the molecule will have to fly into another region with increasing field strength, which will lead again to the loss of kinetic energy. By using many more field stages, separated by a constant distance, this process can be repeated as often as one wishes. As a result, the molecule can be decelerated down to every desired final velocity.

From the above outline, several things follow. First, we notice that the deceleration rate of the molecule depends on its relative position with respect to the electrodes when the fields are switched. The further we let the molecule fly up the potential hill before switching, the more energy is extracted. This position relative to the electrodes at the moment of switching is kept constant during the deceleration process, resulting in the same amount of energy extracted at every field stage. After each time the fields are switched, the molecule moves slower and needs a longer time to reach the same relative position at the next field stage. To compensate for the slowing down of the molecule, the time between the switching of the fields has to increase correspondingly.

So far, the discussion pertained to one molecule only. Furthermore, this single molecule was very special, since the applied switching sequence was arranged to be perfectly synchronous with respect to its motion. Therefore, this molecule is called the *synchronous molecule*. But in order to perform experiments at the end of the decelerator, we would like to decelerate many molecules, not just the synchronous one. Fortunately, the decelerator gives rise to an important feature called *phase stability*, which means that in the deceleration process molecules stay together and form bunches, rather than just spread out. Phase stability will be discussed extensively in Chapter 3, but here we will give a short qualitative description.

Consider a non-synchronous molecule flying a little bit ahead of the synchronous molecule. The non-synchronous molecule travels further up the potential slope than the synchronous one and when the fields are switched, more energy is extracted from it. Since the non-synchronous molecule is slowed down more, it gets a correction towards the synchronous molecule. In a similar way less energy is extracted from a non-synchronous molecule that is lagging behind, also resulting in a correction towards the synchronous molecule. In this way a whole packet of molecules having different (initial) positions and velocities can be kept together throughout the deceleration process.

The above describes phase stability in the longitudinal direction, but in order to keep the packet of molecules together in three dimensions we also need transverse stability. In Fig. 2.6 one of the transversal directions is shown, namely the x direction. In this two dimensional figure the minimum of the electric field lies on the central longitudinal z axis, whereas the maximum field strength is at the electrodes. As mentioned above, low-field seekers feel a counteracting force upon entering regions of increasing field strength. Since the field increases in the transversal direction, low-field seekers feel a restoring force when flying off axis.

This explains stability in the x direction, but not in the y direction, which points out of the paper in Fig. 2.6. By letting successive electrode pairs make an angle of 90° in the plane perpendicular to the longitudinal z axis, as shown in Figure 2.7 , stability in both transversal

directions is guaranteed. A full description of transverse stability of low-field seeking OH radicals in a Stark decelerator is given in [52].

So far, we talked solely about how to decelerate low-field seekers. The question now arises if the same principles can also be applied to high-field seeking molecules. Longitudinally, there is not much of a difference. Where low-field seekers are decelerated upon flying into a region of increasing field strength, high-field seekers are decelerated upon flying into a region of decreasing field strength. And just like we can arrange that low-field seekers constantly feel an increasing field, we can also arrange that high-field seekers constantly feel a decreasing field. But transversally the story is very different. Where an increasing field in the transverse direction means automatically stability for low-field seekers, it means instability for high-field seekers. The high-field seekers are accelerated away from the central axis and have the tendency to crash into the electrodes. Therefore a more complicated setup is needed using dipole lenses as field stages [43], rather than the electrode geometry schematically depicted in Fig. 2.7.

Finally, it might be clear that the whole story about decelerating molecules can equally well be told for accelerating molecules. Indeed, the Stark decelerator can perform just as easily as a Stark accelerator. Still, the technique is primarily used for slowing-down molecules, which has two reasons. First of all, there is a lively interest in cold molecules nowadays, cf. Paragraph 1.1. Second, a 1 meter long decelerator only gives rise to a kinetic energy change that is on the order of 10 meV. Although this suffices to decelerate a molecular beam to a standstill, it is of little avail in acceleration experiments. Note that the 10 meV per meter is about 9 orders of magnitude less than the 40 MeV per meter that is reached in modern charged particle accelerators. These are exactly the 9 orders of magnitude that separate the force on a neutral polar molecule from the force on a charged molecular ion in the same electric field.

2.2.3 Experimental Setup for Decelerating OH Radicals

Figure 2.7 shows a schematic of the experimental setup as used at the Fritz-Haber-Institut in Berlin to decelerate low field seeking OH radicals. We'll consider this setup in more detail to get a feeling for the experimental realization of a Stark deceleration experiment. Furthermore, this setup was used to perform an experiment connected to this thesis, which will be described in Paragraph 4.5. The OH radical and the dimensions of this particular decelerator are also used as parameters in various simulations, which will be presented throughout Chapter 3 and 4.

The experimental setup of Fig. 2.7 is enclosed in three differentially pumped vacuum chambers. A pulsed molecular beam is formed by opening a valve at a frequency of 10 Hz and letting the carrier gas, e.g. Xenon or Krypton, expand into a vacuum of 2×10^{-5} Torr. In

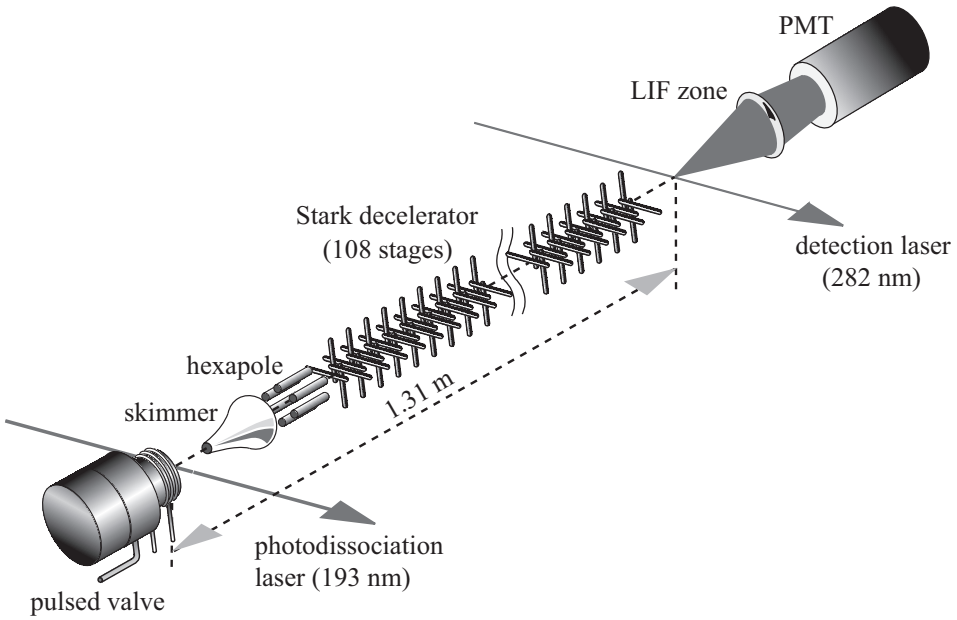

Figure 2.7: *Scheme of the experimental setup used for the deceleration of OH radicals. A carrier gas, seeded with HNO_3, is expanded into the vacuum. Here the HNO_3 is photo-dissociated to form OH. The pulsed molecular beam passes through the skimmer, the hexapole and the Stark decelerator and is detected using an LIF detection scheme. Adapted from [18].*

the carrier gas HNO_3 is seeded, which is photo-dissociated to form OH radicals. The pulsed molecular beam is cooled in the supersonic expansion and after the expansion most OH radicals reside in the lowest rotational ($J = 3/2$) and vibrational level of the electronic ground state $X^2\Pi_{3/2}$. With this setup the low field seeking $M\Omega = -3/4$ and $M\Omega = -9/4$ components of the ground state (cf. Fig. 2.3) can be decelerated, where the Stark shift for the last is three times higher than for the first. The final molecular beam is extracted from the expansion by placing a skimmer with a 2 mm diameter at a distance of 21 mm from the valve. The mean velocity of the beam depends on the carrier gas and is around 450 m/s for OH seeded in Krypton and 370 m/s for OH seeded in Xenon. The longitudinal velocity spread is typically around 15 % FWHM.

Past the skimmer, the molecular beam enters a second vacuum chamber (4×10^{-7} Torr), where it is focussed by a 37 mm long hexapole placed 23.5 mm downstream from the skimmer. The hexapole consists of 6 stainless steel rods with a diameter of 3mm, placed equidistantly at the circumference of a circle with a diameter of 6 mm. When the hexapole operates, every other rod is at high voltage (typically 10 kV), creating a field whose strength increases quadratically with distance from the central axis [65]. Low field seeking molecules flying off axis experience a restoring force that results in a focussing of the molecular beam. The focal length of the

hexapole is chosen such that the beam is focussed into the decelerator.

The first stage of the decelerator is placed at 16.8 mm from the exit of the hexapole. The decelerator consists of 108 equidistant electric field stages that are longitudinally separated by 11 mm. Each stage consists of 2 polished hardened steel rods with a diameter of 6 mm. They are placed parallel in a plane perpendicular to the molecular beam axis at a center to center distance of 10 mm. Alternating electrode pairs are rotated by 90°, resulting in a 4×4 mm^2 transverse acceptance area of the decelerator.

When the decelerator is operating every other field stage is energized and every other grounded, leading to two possible field configurations between which it is being switched, cf. Fig. 3.1. In the experiment, an electric field strength is desired that is as high as possible. A higher field strength does not only increase the deceleration rate, but it also increases the number of molecules that can be decelerated, cf. Chapter 3. On the other hand, increasing the field strength leads to a higher risk of an electrical breakdown, which can cause severe damage to the decelerator. As a compromise, the decelerator is operated by putting a voltage of $\pm$ 20 kV on the electrodes, leading to a maximum field strength of 115 kV/cm near the rods. Depending on the velocity of the decelerating molecules, a field stage is typically at high voltage during 40-400 μs, after which the fields are quickly switched. During the switching of the fields, the voltage drops with an $1/e$ time of about 450 ns, resulting in a time dependence of the field that is square-wave-like.

The OH radicals are detected 21 mm downstream from the decelerator using a laser induced fluorescence (LIF) scheme. In short, LIF detection means that the passing molecules are excited using a tunable laser and that the fluorescence is detected using a photo multiplier tube (PMT). In the scheme used here, 282 nm radiation of a pulsed dye laser is used to induce transitions from the ground state to the $A^2\Sigma^+, v = 1$ state. This state has a short radiative lifetime of 760 ns [66], where the main decay channel is via the $A^2\Sigma^+, v = 1 \rightarrow X^2\Pi_{3/2}, v = 1$ band around 313 nm. The emitted photons are collected onto the PMT with the help of a lens, where stray light from the laser is reduced by using optical filters in front of the PMT.

The experimental data presented in Paragraph 4.5 consist of time of flight (TOF) profiles which give the OH intensity as a function of the time difference between the production of the OH radicals by the dissociation laser and the detection of the OH radicals. Each data point is obtained by running the experiment 32 times at a fixed time difference and averaging the resulting PMT signals. Since the valve opens at a frequency of 10 Hz, each data point takes 3.2 seconds. For more information about the experimental setup, see ref. [18].

Chapter 3

Dynamics of Stark Acceleration/Deceleration

Abstract

Stark acceleration/deceleration relies on time-dependent inhomogeneous electric fields generated by an array of field stages, to repetitively exert an accelerating/decelerating force on polar molecules. Fourier analysis reveals that such fields consist of a superposition of partial waves with well-defined phase velocities, and that molecules whose velocities are close to the phase velocity of a given wave get a ride from that wave. For a square-wave temporal dependence of the Stark field, the phase velocities of the waves are found to be odd-fraction multiples of a fundamental phase velocity λ/τ, with λ and τ the spatial and temporal periods of the field. Here we study explicitly the dynamics due to any of the waves as well as due to their mutual perturbations. We first solve the equations of motion for the case of single-wave interactions and exploit their isomorphism with those for the biased pendulum. Next we analyze the perturbations of the single-wave dynamics by other waves and find that these have no net effect on the phase stability of the acceleration/deceleration process. Finally, we find that a packet of molecules can also ride a wave which results from an interference of adjacent waves. In this case, phase stability areas form around phase velocities that are even-fraction multiples of the fundamental velocity.

3.1 Fourier Representation of the Electric Field

Figure 3.1 shows a prototypical switchable field array suitable for accelerating or decelerating polar molecules. The electric fields are generated by *field stages* (rod-electrode pairs, cylindrical electrodes, or other) longitudinally separated by a distance $\lambda/2$. In the array, every other field stage is energized and every other grounded. Which field stages are energized and which are grounded determines one of two possible *field configurations* of the array. Fig. 3.1 a shows, for the case of four field stages, the electric fields that are generated by the two field configurations. The magnitudes of the electric fields that pertain to the upper and lower field configuration are shown by the red and blue curves and will be referred to as the red, ε_r, and blue, ε_b, field, respectively. Also shown is the longitudinal coordinate z. A given field stage is energized or grounded during a time $\tau/2$, after which the fields are *switched*, i.e., the field stages that were energized become grounded and the field stages that were grounded become energized. Fig. 3.1 b shows the *alternation* between the red and blue fields as a function of time, t. An energized field stage becomes grounded or vice versa during a transient time, $\Delta\tau$. For $\Delta\tau \ll \tau$, the temporal alternation between the red and blue fields is *square-wave-like*.

We'll now represent the spatial and temporal dependence of the *net field*, which results from the switching between the static red and blue fields, by a Fourier series. This will reveal that the net field consists of a superposition of counter-propagating waves with characteristic phase velocities. In Paragraph 3.3 we'll see that a single wave dominates the interaction of the net field with the molecules that are subjected to it. The Fourier analysis makes it possible to single out the dominant wave and to tackle analytically, one by one, the effect of all the partial waves on the motion of the molecules.

We'll begin by Fourier-expanding the spatial dependence of the red field, which is produced by field stages at positions $z = \left(\frac{1}{4} + m\right)\lambda$, with $m = 0, 1, 2, 3...$, see Fig. 3.1 a. The strength of the red field is given by

$$\varepsilon_r(z) = \frac{1}{2}\varepsilon_0 + \sum_{m=1}^{\infty} \varepsilon_m \cos(m\varphi) \tag{3.1}$$

where ε_m are the spatial Fourier coefficients and

$$\varphi \equiv 2\pi z/\lambda - \pi/2 \tag{3.2}$$

Note that the Fourier expansion (3.1) is limited to terms with an even symmetry relative to the field stages, corresponding to the symmetry of the electric field.

The blue field is produced by field stages at positions $z = \left(\frac{3}{4} + m\right)\lambda$, see Fig. 3.1 a,

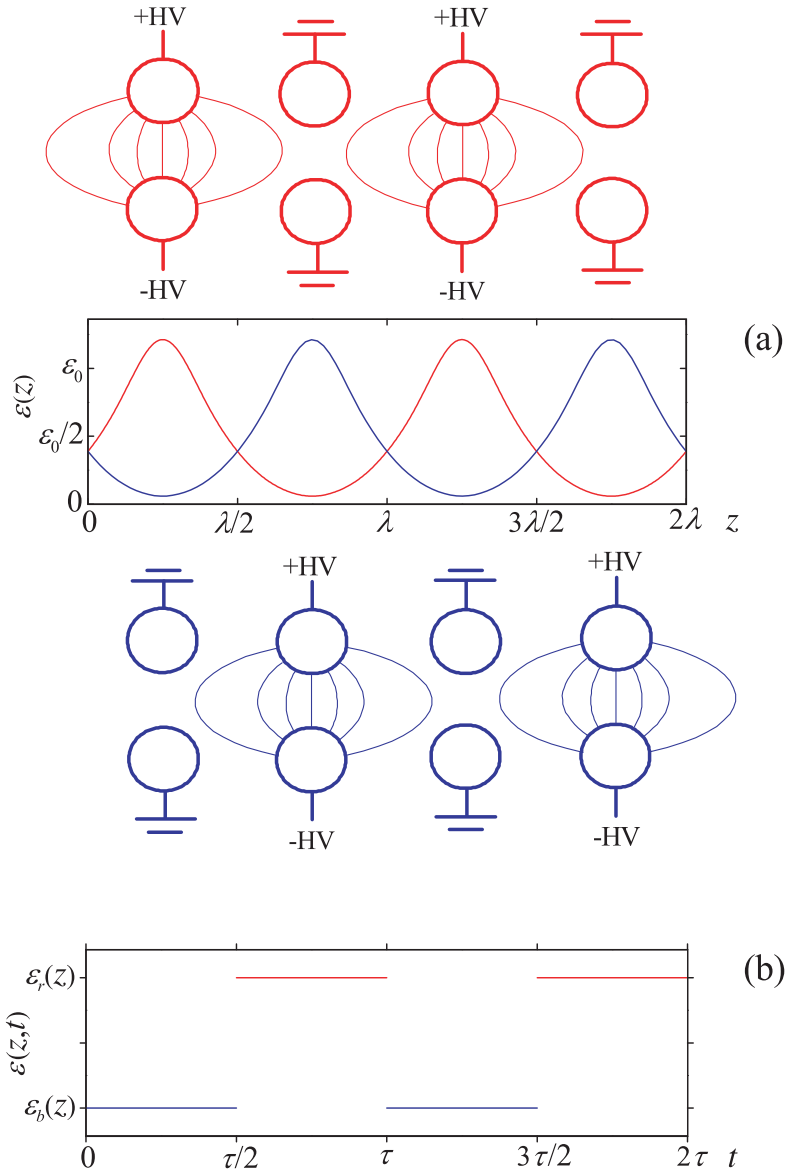

Figure 3.1: *A prototypical switchable field array that generates fields suited for accelerating or decelerating polar molecules. The field stages are longitudinally separated by a distance $\lambda/2$. Every other field stage is energized and every other grounded, leading to two possible field configurations. (a) Electric fields generated by the two field configurations (for the case of four field stages). The electric fields that pertain to the upper and lower field configurations are shown by the red and blue curves and are referred to here as the red, $\mathcal{E}_r$, and blue, $\mathcal{E}_b$, fields, respectively. Also shown is the longitudinal coordinate z; (b) Alternation between the red and blue fields as a function of time, t. A given field stage is energized or grounded during a time $\tau/2$, after which the fields are switched, i.e., the field stages that were energized become grounded and vice versa. The figure pertains to the case of guiding, for which the period τ is constant. The case of a varying period is shown in Fig. 3.2. See also text.*

and so is obtained from the red field by shifting it by $\lambda/2$, i.e.,

$$\varepsilon_b(z) = \varepsilon_r\left(z - \frac{\lambda}{2}\right) = \frac{1}{2}\varepsilon_0 + \sum_{m=1}^{\infty}(-1)^m \varepsilon_m \cos(m\varphi) \tag{3.3}$$

Taking $\Delta\tau = 0$, the net field, $\varepsilon(z,t)$, is given by

$$\begin{aligned} \varepsilon(z,t) &= \varepsilon_b(z) \qquad \text{for} \qquad 0 < t < \tau(t)/2 \\ \varepsilon(z,t) &= \varepsilon_r(z) \qquad \text{for} \qquad \tau(t)/2 < t < \tau(t) \end{aligned} \tag{3.4}$$

see Fig. 3.1 b and Fig. 3.2. While Fig. 3.1 b shows a time dependence of the field with a constant period τ (which corresponds to *guiding* at a constant velocity), Fig. 3.2 shows a time sequence with a varying period $\tau = \tau(t)$ (one which corresponds to *deceleration*).

In order to derive the Fourier representation of the net field, we'll expand eq. (3.4) in terms of a temporal Fourier series. By invoking the 'well-known' result for a temporal square wave [67], the net field can be written as

$$\varepsilon(z,t) = \frac{1}{2}\left[\varepsilon_b(z) + \varepsilon_r(z)\right] + \frac{1}{2}\left[\varepsilon_b(z) - \varepsilon_r(z)\right] \times \sum_{\ell \text{ odd}}^{\infty} \frac{4}{\pi\ell}\sin(\ell\theta) \tag{3.5}$$

where θ is the temporal phase such that

$$\dot{\theta}(t) = \omega(t) = \frac{2\pi}{\tau(t)} \tag{3.6}$$

with $\omega(t)$ the angular frequency. Note that this is a generalization of the familiar case of constant τ, for which

$$\theta(t) = \omega t = \frac{2\pi}{\tau} t \tag{3.7}$$

In either case, the square-wave rises or falls whenever the temporal phase θ is an integer multiple of π.

Substitution into eq. (3.5) from eqs. (3.1)-(3.3) yields

$$\begin{aligned} \varepsilon(z,t) &= \frac{1}{2}\varepsilon_0 + \sum_{p=2,4,\ldots}^{\infty}(-1)^{\frac{1}{2}p}\varepsilon_p \cos(pkz) \\ &\quad + \sum_{n=1,3,\ldots}^{\infty}\sum_{\ell=1,3,\ldots}^{\infty}\frac{4}{\pi\ell}(-1)^{\frac{1}{2}(n+1)}\varepsilon_n \sin(nkz)\sin(\ell\theta) \\ &= \frac{1}{2}\varepsilon_0 + \sum_{p=2,4,\ldots}^{\infty}(-1)^{\frac{1}{2}p}\varepsilon_p \cos(pkz) \\ &\quad + \sum_{n=1,3,\ldots}^{\infty}\sum_{\ell=1,3,\ldots}^{\infty}\frac{2}{\pi\ell}(-1)^{\frac{1}{2}(n+1)}\varepsilon_n(\cos\phi_{+,n,\ell} - \varepsilon_n\cos\phi_{-,n,\ell}) \end{aligned} \tag{3.8}$$

where we made use of the identity $\sin\alpha\sin\beta = \frac{1}{2}\left[\cos(\alpha-\beta) - \cos(\alpha+\beta)\right]$, defined the spatial frequency (wave vector)

$$k \equiv 2\pi/\lambda \tag{3.9}$$

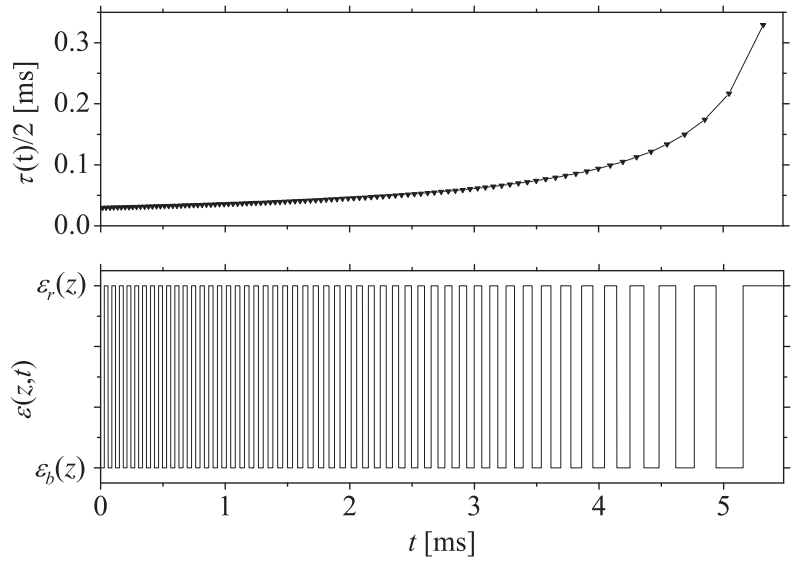

Figure 3.2: *Below: The time dependence of the field pertaining to the case of deceleration, for which the period τ is a function of time, $\tau = \tau(t)$. The case of a constant period is shown in Fig. 3.1. The timing sequence is suitable for decelerating OH radicals on the $(+,1,1)$ wave with $\phi_s = 53°$ from an initial velocity of 370 m/s to a final velocity of 25 m/s. Above: The corresponding time dependence of (half) the switching period $\tau(t)/2$. The markers designate the time difference between two subsequent switching times below.*

and introduced the *phase*

$$\phi_{\pm,n,\ell} \equiv nkz \mp \ell\theta(t) \tag{3.10}$$

Eq. (3.8) reveals that the net field consists of a superposition of *stationary* and of *pairwise counter-propagating partial waves*. The propagating waves move with *well-defined phase velocities*

$$\begin{aligned} \mathrm{V}_{\pm,n,\ell} &\equiv -\frac{\left(\partial\phi_{\pm,n,\ell}/\partial t\right)_z}{\left(\partial\phi_{\pm,n,\ell}/\partial z\right)_t} = \pm\frac{\ell}{n}\frac{\dot{\theta}(t)}{k} = \pm\frac{\ell}{n}\frac{\omega(t)}{k} = \pm\frac{\ell}{n}\frac{\lambda}{\tau(t)} \\ &\equiv \pm\frac{\ell}{n}\mathrm{V}(t) \end{aligned} \tag{3.11}$$

from left to right (+ sign) and from right to left (− sign). The second line of eq. (3.11) defines the *fundamental phase velocity*, $\mathrm{V}(t)$, which is determined solely by the spatial and temporal periods λ and $\tau(t)$.

The path taken here in deriving eq. (3.8) is a shortcut of the route used to derive the same equation in [2]. Moreover, the time dependence of the temporal period and angular frequency is here correctly incorporated right from the outset. Note that the spatial Fourier coefficients ε_m along with the square-wave time dependence fully characterize the net field. While the temporal Fourier coefficients fall only as ℓ^{-1}, the spatial ones fall off roughly exponentially

with m, i.e.,

$$\varepsilon_m \propto \exp[-\xi m] \tag{3.12}$$

where ξ is a decay parameter which depends on the geometry of the field array. Hence we can expect waves with small n and larger ℓ; as we'll see in Chapter 4, waves with $n \lesssim 5$ and $\ell \lesssim 21$ account for all the dynamics so far observed.

3.2 Potential and Force

A molecule with a space-fixed electric dipole moment $\langle\mu\rangle = \langle\mu(\varepsilon)\rangle$ subject to field (3.8) has a Stark energy

$$W(z,t) = -\langle\mu(\varepsilon)\rangle\varepsilon(z,t) \tag{3.13}$$

In what follows, we'll consider molecular states whose space-fixed electric dipole moment is independent of the electric field strength; this is a good approximation when the field-molecule interaction is governed by the first-order Stark effect. Molecular states whose space-fixed electric dipole moment $\langle\mu\rangle$ is parallel ($\langle\mu\rangle > 0$) or antiparallel ($\langle\mu\rangle < 0$) to the electric field strength are referred to as *high-* or *low-field seeking states*, respectively. As mentioned before, the eigenenergy of high-field seekers decreases with increasing field strength, whereas it increases for the low-field seekers. As a result, in an inhomogeneous electric field, such as $\varepsilon(z,t)$, high-field seekers seek regions of maximum, and low-field seekers seek regions of minimum field strength where their eigenenergy is minimal. In the net field (3.8), the Stark energy becomes

$$\begin{aligned} W(z,t) &= \frac{1}{2}W_0 + \sum_{p\ \text{even}}^{\infty} (-1)^{\frac{1}{2}p} W_p \cos(pkz) \\ &\quad + \sum_{n\ \text{odd}}^{\infty} \sum_{\ell\ \text{odd}}^{\infty} \frac{2}{\pi\ell}(-1)^{\frac{1}{2}(n+1)} W_n(\cos\phi_{+,n,\ell} - \cos\phi_{-,n,\ell}) \end{aligned} \tag{3.14}$$

with

$$W_i = -\langle\mu\rangle\varepsilon_i \qquad i = 1, 2, 3, ... \tag{3.15}$$

We note that in the case of a non-linear Stark effect [68], eq. (3.14) can still be used to represent the Stark energy; the Fourier coefficients of eq. (3.14) will, however, no longer be linear in field strength. If the eigenenergy Fourier coefficients, eq. (3.15), are available as the primary parameters, the nature of the Stark effect doesn't need to be considered explicitly [69].

Since the Stark energy plays the role of a potential for the motion of the molecules, the force, $F(z,t)$, that the field exerts on a molecule of mass M is given by

$$\begin{aligned} F(z,t) &= -\frac{dW(z,t)}{dz} = \sum_{p\ \text{even}} MA_p \sin(pkz) \\ &\quad + \sum_{n\ \text{odd}} \sum_{\ell\ \text{odd}} MA_{n,\ell}(\sin\phi_{+,n,\ell} - \sin\phi_{-,n,\ell}) \end{aligned} \tag{3.16}$$

where

$$\begin{aligned} A_p &\equiv (-1)^{\frac{1}{2}p}\frac{pk}{M}W_p \\ A_{n,\ell} &\equiv (-1)^{\frac{1}{2}(n+1)}\frac{2nk}{\pi\ell M}W_n \end{aligned} \tag{3.17}$$

Thus we see that a molecule subjected to force (3.16) is acted upon by an infinite multitude of stationary as well as propagating and counter-propagating waves. However, as we'll see in Paragraph 3.3, only a single wave dominates the molecule-field interaction. Which wave it is, is determined by the difference between the wave's phase velocity and the velocity of the molecule: only a wave whose initial phase velocity comes close to the initial velocity of the molecule can become dominant. Since we have the velocities of the waves experimentally under control, we can choose which wave we would like to interact with which molecule(s). In order to quantify this statement, we must do the dynamics.

3.3 Dynamics of the Interaction of Molecules with a Single Wave

In this Paragraph we'll examine the dynamics of the interaction of a bunch of molecules with a single wave. After developing a formalism for describing such an interaction and discussing its dynamics, we'll be able to show why, to an excellent approximation, the effect of all the other waves can be neglected. We'll also tackle the effects due to interfering waves which interact jointly with a bunch of molecules.

3.3.1 Force Exerted by an Arbitrary Wave

As we can glean from eqs. (3.8), (3.14), or (3.16), an arbitrary propagating wave can be labelled by a pair of *odd* integers, n and ℓ, and by its propagation direction (+ for left to right or − for right to left), i.e., by $(\pm, n, \ell)$. Since the molecules move from left to right by convention, in what follows we'll consider waves moving from left to right. Thus such an otherwise arbitrary wave travels from left to right with a phase velocity

$$\mathrm{V}_{n,\ell} \equiv \mathrm{V}_{+,n,\ell} = \frac{\ell}{n}\frac{\dot{\theta}}{k} \tag{3.18}$$

cf. eq. (3.11), and exerts a force on a molecule given by

$$F_{n,\ell}(z,t) = MA_{n,\ell}\sin\phi_{n,\ell} \tag{3.19}$$

with the phase

$$\phi_{n,\ell} \equiv \phi_{+,n,\ell} = nkz - \ell\theta(t) \tag{3.20}$$

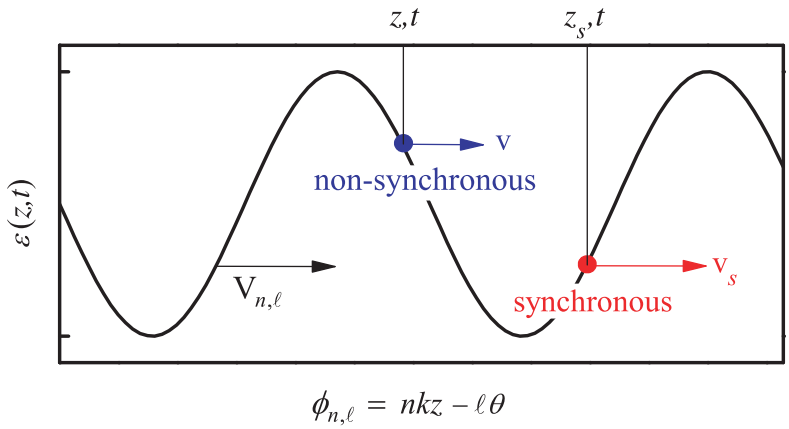

Figure 3.3: *A synchronous and a non-synchronous molecule subjected to the field $\varepsilon(z,t)$ of a (n,ℓ) wave moving at a phase velocity $V_{n,\ell}$ (all motion is from left to right). The change of the velocity, v_s, of a synchronous molecule is such that its phase ϕ_s with respect to the traveling field remains constant. This is the case when $v_s = V_{n,\ell}$. The velocity, v, of a non-synchronous molecule and its phase, $\phi_{n,\ell}$, both change with time. Also shown are the spatial coordinates of the synchronous and non-synchronous molecule, z_s and z, respectively.*

The corresponding acceleration/deceleration then becomes

$$a_{n,\ell} \equiv \ddot{z}_{n,\ell} = \frac{F_{n,\ell}(z,t)}{M} = A_{n,\ell} \sin \phi_{n,\ell} \tag{3.21}$$

3.3.2 Synchronous Molecule and Its Velocity

A key concept in tackling the molecule-wave interaction is that of a *synchronous molecule*. This is defined as the molecule which maintains a *constant (synchronous) phase*

$$\phi_s \equiv (\phi_{n,\ell})_s = nkz_s - \ell\theta(t) = const. \tag{3.22}$$

with respect to a *given wave* (n,ℓ) throughout the acceleration/deceleration process - no matter what, see Figure 3.3.

It should be noted that the definition of the synchronous phase given here is slightly different from the definition that has been used in earlier descriptions of phase-stability in a Stark decelerator [49]-[51],[53]. In these earlier studies the synchronous phase was defined in terms of the position of the synchronous molecule relative to the electrodes, and this position was required to be the same every time that the electric fields were switched from one configuration to the other. Although this definition takes the full spatial dependence of the Stark interaction into account, it only specifies the synchronous phase at the moment when the fields are switched. In the case when the Stark interaction is governed by a single wave (n,ℓ), both definitions are equivalent.

From eq. (3.19) it immediately follows that the synchronous molecule is acted upon by a *constant force*

$$(F_{n,\ell})_s = MA_{n,\ell} \sin \phi_s \tag{3.23}$$

and thus has a *constant acceleration/deceleration*

$$(a_{n,\ell})_s = A_{n,\ell} \sin \phi_s \equiv a_s \tag{3.24}$$

From eq. (3.24) we see that the acceleration/deceleration rate can be *controlled* by *tuning the synchronous phase*. As follows from eq. (3.22), at $t = 0$, when the fields are switched for the first time, the synchronous phase is simply

$$\phi_s(z_s, t = 0) = nkz_s \tag{3.25}$$

Therefore, the synchronous phase can be tuned by launching the *switching sequence* (or *burst*) when the synchronous molecule has the desirable longitudinal coordinate z_s. The subsequent switching times between the two field configurations can always be chosen such that the synchronous molecule will keep the same phase.

With a tunable acceleration/deceleration, the initial velocity of the synchronous molecule can be increased/decreased to any value

$$\mathrm{v}_s(t) = \mathrm{v}_s(t = 0) + a_s t \tag{3.26}$$

3.3.3 Phase Velocity, Temporal Phase, and Switching Sequence

In order to keep the phase of the synchronous molecule constant during acceleration/deceleration, the phase velocity of the wave that interacts with the molecule needs to be varied. This is done by applying a *variable* switching sequence to the field array as the molecule progresses through it. In other words, the temporal frequency or period of the applied field is made time-dependent, $\omega = \omega(t)$ or $\tau = \tau(t)$. As a result, the phase velocity becomes also time dependent, cf. eq. (3.11). In this paragraph we'll show that the phase velocity of the wave is always equal to the synchronous velocity of the molecule, as one would expect. Furthermore, we'll evaluate the temporal phase and hence the timing sequence needed to *keep* a molecule synchronous.

From the definition of the synchronous phase, eq. (3.22), we obtain

$$\dot{\phi}_s = 0 = nk\dot{z}_s - \ell\dot{\theta} \tag{3.27}$$

from which it follows that

$$\dot{z}_s \equiv \mathrm{v}_s = \frac{\ell}{n}\frac{\dot{\theta}}{k} \tag{3.28}$$

By comparing this result with eq. (3.18), we see that, indeed, the phase velocity is equal to the synchronous velocity

$$\mathrm{v}_s = \mathrm{V}_{n,\ell} \tag{3.29}$$

In what follows we'll use the following notation for the initial phase and synchronous velocities

$$\mathrm{v}_s(0) = \mathrm{V}_{n,\ell}(0) = \frac{\ell}{n}\frac{\omega(t=0)}{k} = \frac{\ell}{n}\frac{\lambda}{\tau(t=0)} \equiv \frac{\ell}{n}\mathrm{V}_0 \tag{3.30}$$

In order to derive an expression for the temporal phase consistent with the condition of a constant synchronous phase, we invoke eq. (3.22)

$$\theta(t) = \frac{nkz_s(t)}{\ell} - \frac{\phi_s}{\ell} \tag{3.31}$$

and substitute for $z_s(t)$ from the first integral of eq. (3.26),

$$z_s(t) = \frac{1}{2}a_s t^2 + \mathrm{v}_s(0)t + z_0 = \frac{1}{2}a_s t^2 + \frac{\ell}{n}\mathrm{V}_0 t + \frac{\phi_s}{nk} \tag{3.32}$$

where the initial position, z_0, was obtained from eq. (3.25). This yields a temporal phase

$$\theta(t) = \frac{nkz_s(t)}{\ell} - \frac{\phi_s}{\ell} = \frac{1}{2}\frac{n}{\ell}ka_s t^2 + k\mathrm{V}_0 t \tag{3.33}$$

which pertains to a square wave that falls/rises only when the following periodic condition is fulfilled:

$$\theta(t) = \frac{1}{2}\frac{n}{\ell}ka_s t^2 + k\mathrm{V}_0 t = q\pi \qquad\qquad q = 0, 1, 2, ... \tag{3.34}$$

Eq. (3.34) defines exactly that switching sequence which is required in order to keep the phase of the synchronous molecule constant and hence for achieving a constant acceleration/deceleration. The corresponding switching times are given by solving eq. (3.34) for $t(q)$, with the result

$$t(q) = \frac{\ell}{n}\frac{\mathrm{V}_0}{a_s}\left[\left(\frac{2\pi q n a_s}{\ell k \mathrm{V}_0^2} + 1\right)^{1/2} - 1\right] \tag{3.35}$$

which is identical with a result obtained earlier [70]. Figure 3.2 shows a switching sequence generated by eq. (3.34), suitable for decelerating OH radicals.

3.3.4 Equation of Motion

The equation of motion of a non-synchronous molecule subjected to wave (n, ℓ) is

$$\ddot{z} = \frac{F_{n,\ell}}{M} = A_{n,\ell}\sin\phi_{n,\ell} \tag{3.36}$$

where we made use of equation (3.19). For the synchronous molecule we have

$$\ddot{z}_s = \frac{F_{n,\ell}}{M} = A_{n,\ell}\sin\phi_s \tag{3.37}$$

A combination of eqs. (3.36) and (3.37) yields

$$\ddot{z} - \ddot{z}_s = A_{n,\ell}(\sin\phi_{n,\ell} - \sin\phi_s) \tag{3.38}$$

The left-hand side of eq. (3.38) can be recast in terms of the non-synchronous and synchronous phase. We have, with the help of eq. (3.20),

$$\begin{aligned} \phi_{n,\ell}(t) - \phi_s(t) &\equiv \Delta\phi_{n,\ell}(t) \\ &= nkz(t) - \ell\theta(t) - [nkz_s(t) - \ell\theta(t)] \\ &= nk[z(t) - z_s(t)] \equiv nk\Delta z(t) \end{aligned} \tag{3.39}$$

where $\Delta z \equiv z - z_s$ is the longitudinal distance between the non-synchronous and synchronous molecule, see also Fig. 3.3. Eq. (3.39) implies the following equations for the time derivatives:

$$\dot{\phi}_{n,\ell}(t) - \dot{\phi}_s(t) \equiv \Delta\dot{\phi}_{n,\ell}(t) = nk(\dot{z} - \dot{z}_s) \equiv nk\Delta\,\dot{z} \tag{3.40}$$

and

$$\ddot{\phi}_{n,\ell}(t) - \ddot{\phi}_s(t) \equiv \Delta\ddot{\phi}_{n,\ell}(t) = nk(\ddot{z} - \ddot{z}_s) \equiv nk\Delta\,\ddot{z} \tag{3.41}$$

However,

$$\Delta\dot{\phi}_{n,\ell}(t) = \dot{\phi}_{n,\ell}(t) \tag{3.42}$$

and

$$\Delta\ddot{\phi}_{n,\ell}(t) = \ddot{\phi}_{n,\ell}(t) \tag{3.43}$$

since, by definition, $\dot{\phi}_s(t) = \ddot{\phi}_s(t) = 0$.

Substituting eqs. (3.41) and (3.43) into eq. (3.38) finally yields

$$\ddot{\phi}_{n,\ell} = \alpha_{n,\ell}(\sin\phi_{n,\ell} - \sin\phi_s) \tag{3.44}$$

with

$$\alpha_{n,\ell} \equiv nkA_{n,\ell} = (-1)^{\frac{1}{2}(n+1)}\frac{2n^2k^2}{\pi\ell M}W_n \tag{3.45}$$

3.3.5 Solving the Equation of Motion

Relating the motion of all molecules to a molecule which maintains a constant (synchronous) phase with respect to a given wave not only greatly simplifies the equation of motion but reduces it to a form which is isomorphic with the equation of motion of a *biased pendulum*, see Figure 3.4. Since the biased pendulum problem can be well understood - both mathematically and intuitively - it offers precious lessons about the Stark accelerator/decelerator dynamics [2].

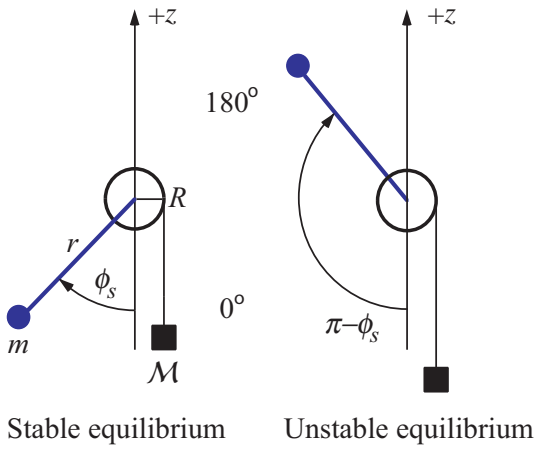

Figure 3.4: *Realization of a plane biased pendulum: a bob of mass m is fixed to a rigid suspension of length r which is attached to an axle of diameter R; wound around the axle is a string that carries a bias of mass $\mathcal{M}$. A plane biased pendulum is a one-dimensional system, whose only coordinate is the angle ϕ between the vertical axis z and the bob suspension r. The stable and unstable equilibrium points are located symmetrically with respect to a plane perpendicular to the direction of the z axis at angles ϕ_s and $\pi - \phi_s$, respectively. The stable-equilibrium angle ϕ_s of the biased pendulum corresponds to the synchronous phase of the Stark accelerator/decelerator.*

Both the biased-pendulum problem and the Stark accelerator/decelerator have the following Lagrangian

$$\mathcal{L}(\phi, \dot{\phi}) = \frac{1}{2}\eta\dot{\phi}^2 - \eta\alpha_{n,\ell}(\cos\phi + \phi\sin\phi_s) \tag{3.46}$$

where η and $\alpha_{n,\ell}$ are constants different for the two problems. The application of Lagrange's equation

$$\frac{\partial\mathcal{L}}{\partial\phi} = \frac{d}{dt}\frac{\partial\mathcal{L}}{\partial\dot{\phi}} \tag{3.47}$$

immediately yields the correct equation of motion, namely eq. (3.44).

The first term of the Lagrangian (3.46) is the kinetic energy, the second term is the potential,

$$\begin{aligned} V(\phi) &= \eta\alpha_{n,\ell}(\cos\phi + \phi\sin\phi_s) = (-1)^{\frac{1}{2}(n+1)}\frac{2W_n}{\pi\ell}(\cos\phi + \phi\sin\phi_s) \\ &= (-1)^{\frac{1}{2}(n+1)}\frac{2W_n}{\pi\ell}\cos\phi + (-1)^{\frac{1}{2}(n+1)}\frac{2W_n}{\pi\ell}\phi\sin\phi_s \equiv V_P(\phi) + V_B(\phi) \end{aligned} \tag{3.48}$$

In writing down the potential we split it into the pendulum part, $V_P(\phi)$, and the bias part, $V_B(\phi)$. These are plotted for four different cases ($\alpha_{n,\ell}$ positive/negative, acceleration/deceleration) in Figure 3.5. The figure provides a valuable insight into the dynamics of the studied system(s). Like a simple pendulum, a biased pendulum has two equilibrium points, a *stable* and an *unstable* one, the latter called here a *tipping point*. These are located, symmetrically, at $\phi = \phi_s$

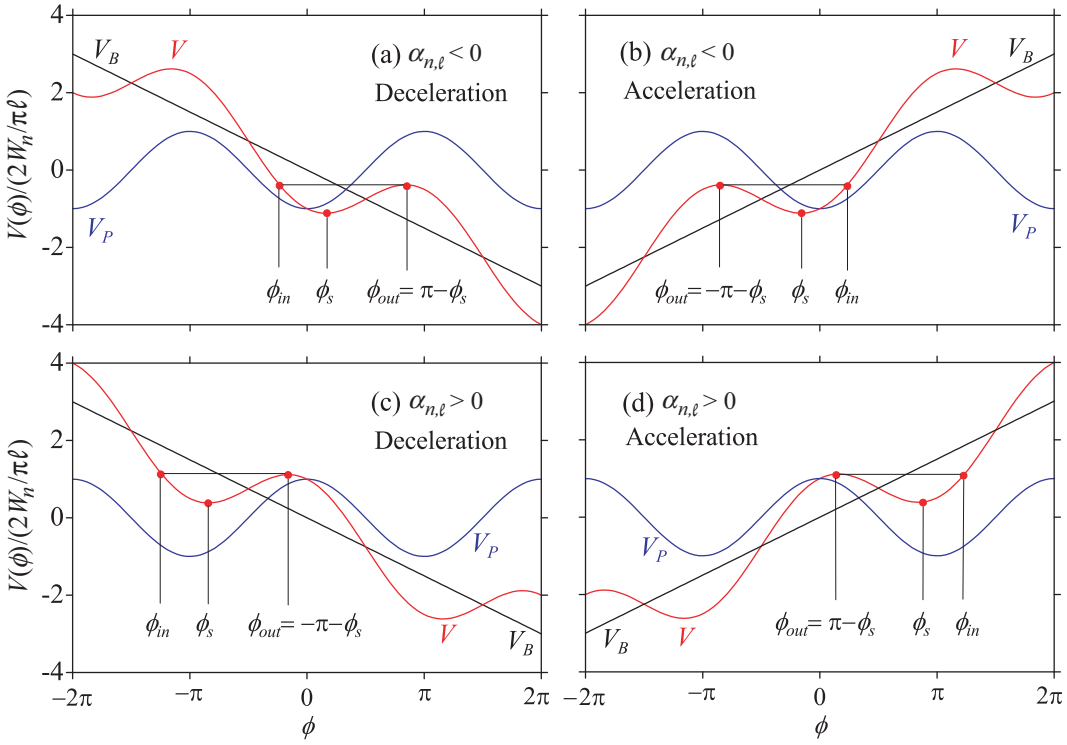

Figure 3.5: *The potential $V(\phi)$ of a biased pendulum or, interchangeably, of a Stark accelerator/decelerator (red curve) along with the pure pendulum potential $V_P(\phi)$ (blue curve) and the potential of the bias $V_B(\phi)$ (black curve). Also shown are the minimum (stable) and maximum (unstable) equilibrium points. One can see that the unstable equilibrium point coincides with the outermost turning point, ϕ_{out}. Angles in excess of ϕ_{out} result in a nonuniform accelerating rotation of the pendulum about the axle, propelled by the falling bias. On the other hand, the inner turning point, ϕ_{in}, cannot be exceeded, since the potential at $\phi < \phi_{in}$ is repulsive. The cases of acceleration and deceleration for $\alpha_{n,\ell} < 0$ and $\alpha_{n,\ell} > 0$ are shown in panels a-d, as labelled. The potential is expressed in terms of its amplitude $\frac{2W_n}{\pi\ell}$.*

and $\phi = \pi - \phi_s$ and correspond to the positions of the minimum and maximum (modulo 2π) of the potential (3.48), as revealed by taking the first and second derivatives of the potential with respect to ϕ. The unstable equilibrium point coincides with the outermost turning point, ϕ_{out}, for a motion under the potential (3.48). Angles in excess of ϕ_{out} result in a nonuniform accelerating rotation of the pendulum about its axle, propelled by the falling bias. For the accelerator/decelerator this means that non-synchronous molecules whose phase would exceed the tipping point will fall out of the potential well due to $V(\phi)$ and thus be lost. Exceeding the tipping point amounts to disengaging from the acceleration/deceleration process. On the other hand, the inner turning point, ϕ_{in}, cannot be exceeded, since the potential at $\phi < \phi_{in}$ is repulsive. The phase of a non-synchronous molecule that is confined by the potential periodically oscillates about the synchronous phase, whose value is set by the position of the potential's minimum. We also note that for higher acceleration/deceleration rates, the potential minimum

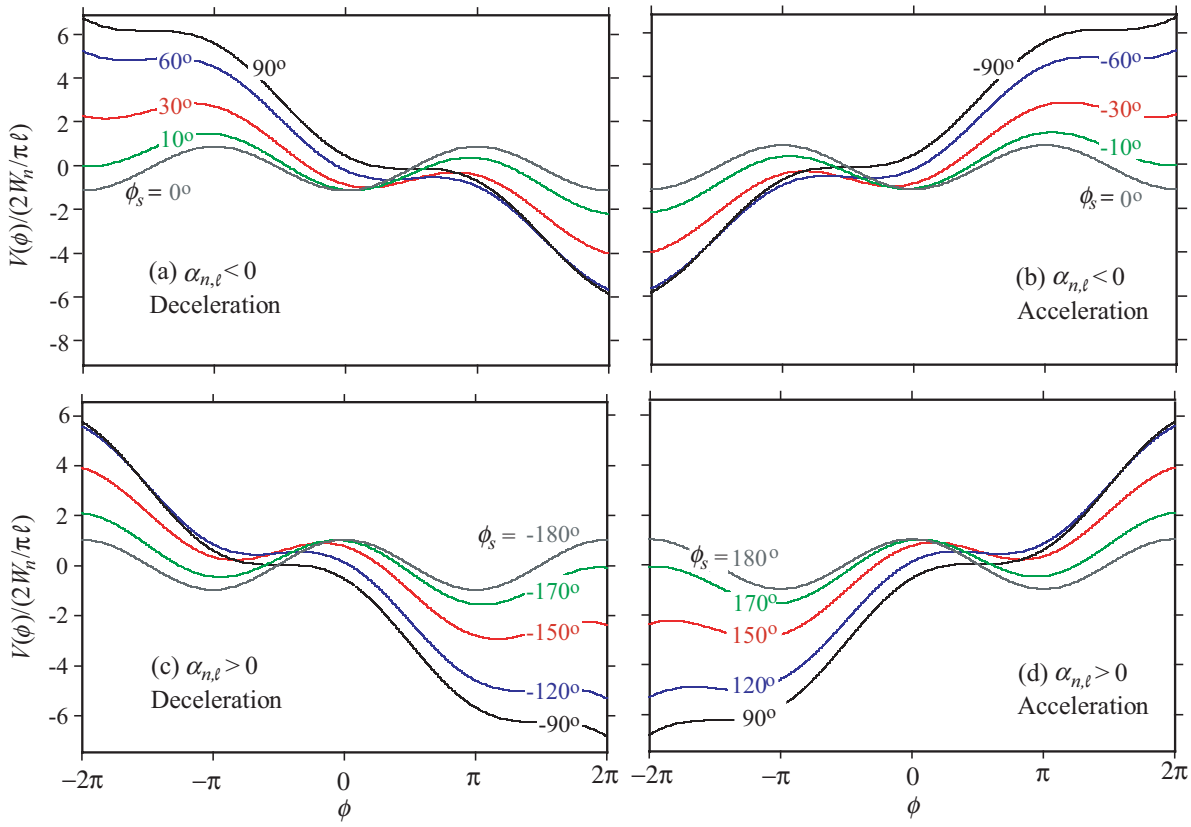

Figure 3.6: *Biased pendulum or, interchangeably, Stark accelerator/decelerator potential $V(\phi)$ for a range of values of the stable equilibrium point or, interchangeably, of the synchronous phase, ϕ_s. For $\phi_s = \pm\pi/2$, the stable and unstable equilibrium points coincide and the potential cannot support any bound states. The potential is expressed in terms of its amplitude $\frac{2W_n}{\pi\ell}$.*

shifts correspondingly and the well becomes shallower, see Figure 3.6. This leads to a reduction and shifting of areas where stable oscillations of the non-synchronous phase about the synchronous one can take place, i.e., the areas of the so called *phase stability*. In what follows we'll evaluate the phase-stable areas of the phase space exactly.

Multiplying the equation of motion (3.44) - where we dropped the n, ℓ subscripts from the phase for notational simplicity - by $\dot{\phi}$ and integrating once over time

$$\int \ddot{\phi}\dot{\phi}dt = \alpha_{n,\ell}\int \sin\phi\dot{\phi}dt - \alpha_{n,\ell}\int \sin\phi_s\dot{\phi}dt \tag{3.49}$$

yields

$$\dot{\phi}^2 = -2\alpha_{n,\ell}(\cos\phi + \phi\sin\phi_s) + \beta \tag{3.50}$$

or

$$\dot{\phi} = \pm[-2\alpha_{n,\ell}(\cos\phi + \phi\sin\phi_s) + \beta]^{1/2} \tag{3.51}$$

with β an integration constant. Eq. (3.51) represents the trajectory of a non-synchronous molecule through phase space $(\phi, \dot{\phi})$.

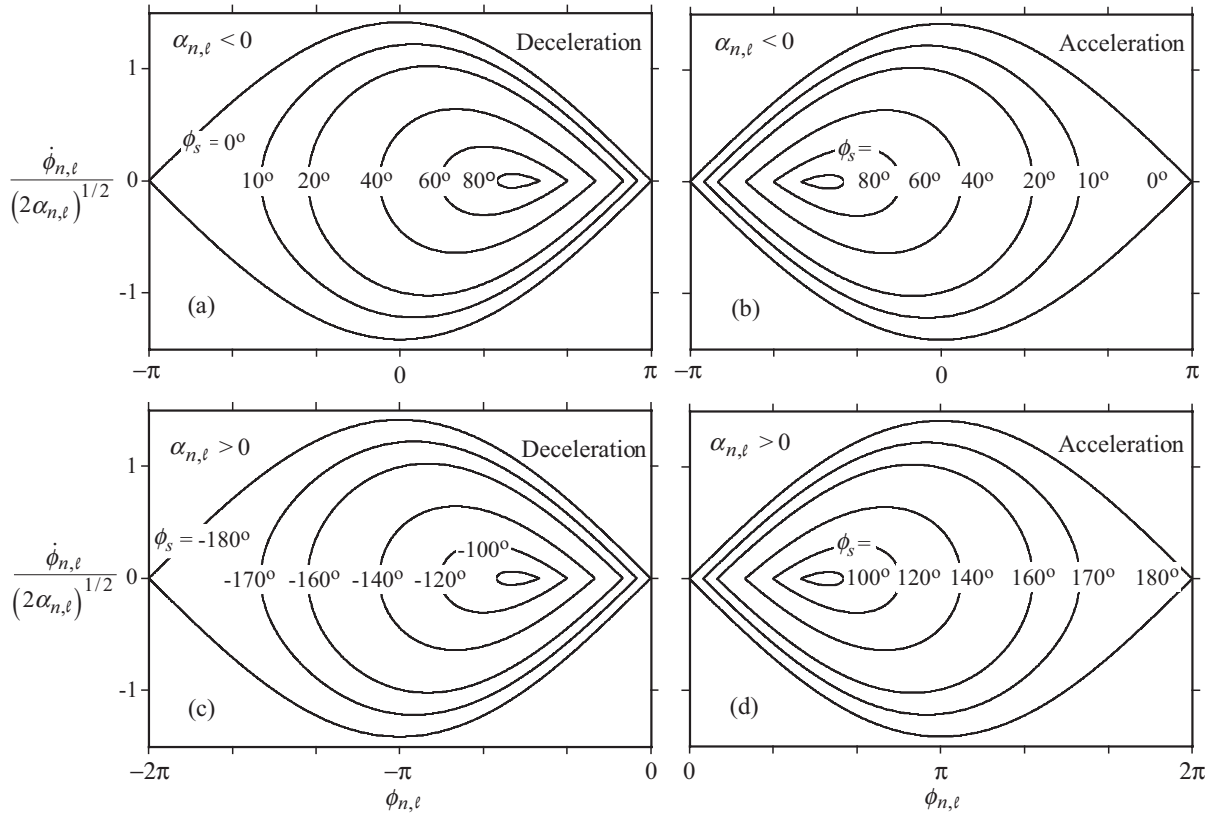

Figure 3.7: *Separatrices for different values of the synchronous phase, ϕ_s. Contours demarcate domains in phase space $(\phi_{n,\ell}, \dot{\phi}_{n,\ell})$ where stable oscillations take place. Note that $\dot{\phi}_{n,\ell}\,/(2\alpha_{n,\ell})^{1/2}$ plays the role of a (dimensionless) momentum and the angle $\phi_{n,\ell}$ of its conjugate coordinate. Depending on the sign of $\alpha_{n,\ell}$ and on the sign of a_s (acceleration or deceleration), four cases are distinguished and shown in panels (a)-(d).*

For a bound motion, β is determined by the condition $\dot{\phi} = 0$, which defines the value ϕ_{out} of the non-synchronous phase at the outer *turning point*, see Figs. 3.5 and 3.6. Thus

$$\beta = 2\alpha_{n,\ell}(\cos\phi_{out} + \phi_{out}\sin\phi_s) \tag{3.52}$$

A special case occurs when the turning point reaches its maximum, tipping value. This determines the *separatrix*, which separates the bound and unbound motion in the phase space. Along the separatrix, $\dot{\phi}$ becomes zero at the nearest local extremum of the potential. We distinguish four cases, corresponding to the four different types of potentials shown in Figs. 3.5 and 3.6.

Case 1: $\alpha_{n,\ell} < 0$, $0 \le \phi_s \le \frac{\pi}{2}$ and $-\pi \le \phi \le \pi$, pertaining to deceleration.
Along the separatrix, $\dot{\phi}$ becomes zero at $\phi_{out} = \pi - \phi_s$, see also Fig. 3.5 a. Using eq. (3.52) we obtain for the corresponding β

$$\beta = -2\alpha_{n,\ell}[\cos\phi_s - (\pi - \phi_s)\sin\phi_s] \tag{3.53}$$

Inserting this into eq. (3.51) gives the expression for the separatrix

$$\dot{\phi} = \pm[-2\alpha_{n,\ell}(\cos\phi + \cos\phi_s + (\phi - \pi + \phi_s)\sin\phi_s)]^{1/2} \tag{3.54}$$

which is plotted for various values of ϕ_s in Figure 3.7 a. For the other cases we can follow exactly the same procedure.

Case 2: $\alpha_{n,\ell} < 0$, $-\frac{\pi}{2} \leq \phi_s \leq 0$ and $-\pi \leq \phi \leq \pi$, pertaining to acceleration.
Along the separatrix, $\dot{\phi}$ becomes zero at $\phi_{out} = -\pi - \phi_s$; see also Fig. 3.5 b. Here

$$\beta = -2\alpha_{n,\ell}[\cos\phi_s + (\pi + \phi_s)\sin\phi_s] \tag{3.55}$$

and the separatrix is given by

$$\dot{\phi} = \pm[-2\alpha_{n,\ell}(\cos\phi + \cos\phi_s + (\phi + \pi + \phi_s)\sin\phi_s)]^{1/2} \tag{3.56}$$

which is plotted for various values of ϕ_s in Fig. 3.7 b.

Case 3: $\alpha_{n,\ell} > 0$, $-\pi \leq \phi_s \leq -\frac{\pi}{2}$ and $-2\pi \leq \phi \leq 0$, pertaining to deceleration.
Along the separatrix, $\dot{\phi}$ becomes zero at $\phi_{out} = -\pi - \phi_s$; see also Fig. 3.5 c. Here

$$\beta = 2\alpha_{n,\ell}[-\cos\phi_s - (\pi + \phi_s)\sin\phi_s] \tag{3.57}$$

and so the separatrix is given by

$$\dot{\phi} = \pm[2\alpha_{n,\ell}(-\cos\phi - \cos\phi_s - (\phi + \pi + \phi_s)\sin\phi_s)]^{1/2} \tag{3.58}$$

which is plotted for various values of ϕ_s in Fig. 3.7 c.

Case 4: $\alpha_{n,\ell} > 0$, $\frac{\pi}{2} \leq \phi_s \leq \pi$ and $0 \leq \phi \leq 2\pi$, pertaining to acceleration.
Along the separatrix, $\dot{\phi}$ becomes zero at $\phi_{out} = \pi - \phi_s$; see also Fig. 3.5 d. Here

$$\beta = 2\alpha_{n,\ell}[-\cos\phi_s + (\pi - \phi_s)\sin\phi_s] \tag{3.59}$$

and the separatrix is given by

$$\dot{\phi} = \pm[2\alpha_{n,\ell}(-\cos\phi - \cos\phi_s + (\pi - \phi - \phi_s)\sin\phi_s)]^{1/2} \tag{3.60}$$

which is plotted for various values of ϕ_s in Fig. 3.7 d.

For all other combinations of $\alpha_{n,\ell}$ and ϕ_s there is no phase stability, as also illustrated by Fig. 3.6. We note that case 3 and 4 differ from case 1 and 2 just by a shift over π.

3.3.6 Small-angle Dynamics

Eq. (3.44) can be solved analytically for small phase oscillations, i.e., for $\Delta\phi \ll 1$. In that case

$$\sin\phi = \sin(\Delta\phi + \phi_s) = \sin\phi_s\cos\Delta\phi + \cos\phi_s\sin\Delta\phi \simeq \sin\phi_s + \Delta\phi\cos\phi_s \tag{3.61}$$

and so eq. (3.44) becomes

$$\ddot{\Delta\phi} \simeq \alpha_{n,\ell}\Delta\phi\cos\phi_s \tag{3.62}$$

which is recognized as the harmonic oscillator equation for $\alpha_{n,\ell} < 0$ and $-\pi/2 \leq \phi_s \leq \pi/2$ or for $\alpha_{n,\ell} > 0$ and $\pi/2 \leq \phi_s \leq 3\pi/2$. Other combinations of $\alpha_{n,\ell}$ and ϕ_s lead to non-oscillatory, exponentially diverging solutions of eq. (3.62), which preclude phase stability.

The harmonic solution of eq. (3.62) is

$$\Delta\phi \simeq \Delta\phi_0\cos(\Omega t + \delta_0) \tag{3.63}$$

with

$$\Omega^2 \equiv -\alpha_{n,\ell}\cos\phi_s \equiv \Omega_{n,\ell}^2 \geq 0 \tag{3.64}$$

the square of the angular frequency of the harmonic phase oscillations, $\Delta\phi_0$ the initial phase difference, and δ_0 the initial temporal phase. The harmonic oscillation frequency is given by

$$\frac{\Omega}{2\pi} = \left((-1)^{\frac{1}{2}(n-1)}\frac{2n^2W_n}{\pi\ell M\lambda^2}\cos\phi_s\right)^{1/2} \tag{3.65}$$

where we made use of eqs. (3.45) and (3.64). This differs for $n > 1$ from the result obtained previously [71].

Thus we see that for small relative phase angles $\Delta\phi$, the non-synchronous molecule oscillates harmonically about the synchronous one with a frequency Ω. As $\Delta\phi$ increases, the anharmonic terms in the sine expansion become more important and the small-angle approximation becomes invalid. The onset of the anharmonic terms brings about more complicated, lower-frequency oscillations. At the separatrix, the oscillation frequency drops to zero and beyond the separatrix the motion becomes unbound with no periodic phase oscillations.

At this juncture, we'll make a general point which we'll use frequently later on. We'll refer to the oscillations of the non-synchronous phase about the synchronous one as *slow oscillations*. This reflects the fact that Ω is typically much smaller than $\omega(t)$. In contradistinction, we'll refer to the oscillations at frequency $\omega(t)$ as *fast oscillations*.

We note that the period $\mathcal{T}_{n,\ell}$ of the (slow) oscillations is generally given by

$$\mathcal{T}_{n,\ell} = 2\int_{\phi_{in}}^{\phi_{out}}\frac{dt}{d\phi_{n,\ell}}d\phi_{n,\ell} \tag{3.66}$$

and can be evaluated numerically from the first integral of the equation of motion (3.51) and from the transcendental equations for the turning points $\phi_{in} \equiv \phi_{in}^{n,\ell}$ and $\phi_{out} \equiv \phi_{out}^{n,\ell}$. For harmonic oscillations,

$$\mathcal{T}_{n,\ell} = \frac{2\pi}{\Omega_{n,\ell}} \tag{3.67}$$

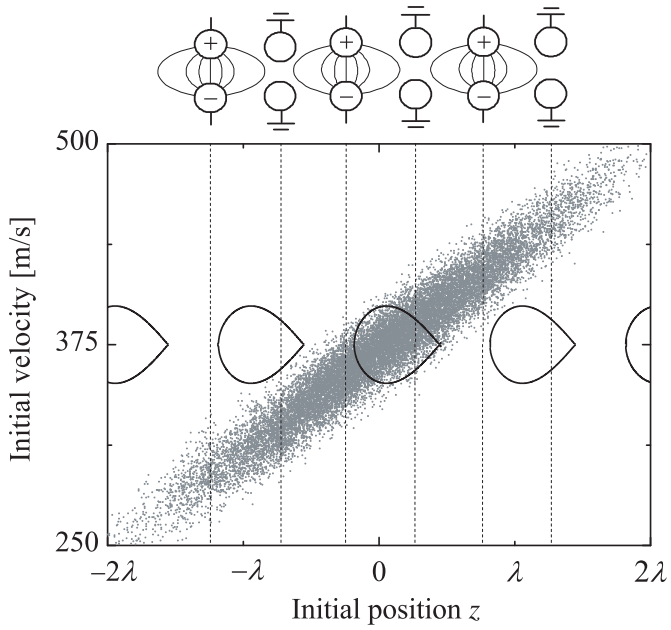

Figure 3.8: *Phase-space distribution of a molecular beam pulse as it enters the Stark accelerator/decelerator. The best overlap between a phase stable area (black 'fishes') and the molecular beam pulse (swarm of dots) is obtained when the synchronous molecule matches the mean position and velocity of the beam pulse.*

3.3.7 Phase Stability

The notion of *phase stability* pertains to periodic solutions of the equation of motion (3.44). Physically, these correspond to stable oscillations of the non-synchronous molecule about the synchronous one. The solutions of the equation of motion, given by eqs. (3.54), (3.56), (3.58), and (3.60), determine a boundary for the momentum of a non-synchronous molecule, $\dot{\phi}_{n,\ell}$, as a function of its phase, $\phi_{n,\ell}$, that pertains to phase-stable motion. That is to say, together, $(\phi_{n,\ell}, \dot{\phi}_{n,\ell})$ delimit an *area of phase stability in the phase space* for molecules interacting with a given wave (n, ℓ).

Phase stability is a key property of a Stark accelerator/decelerator, which enables handling other molecules than just the synchronous one. This is what makes the device a practical one, since *bunches* of molecules, with a *distribution of positions and velocities*, can then be accelerated/decelerated. Without phase stability, only a single molecule could be handled, namely the synchronous one [47, 48].

The explicit evaluation of the phase stable areas, eqs. (3.54), (3.56), (3.58), and (3.60), clarifies several issues:

(a) The *choice* of the *synchronous molecule*. The distribution of positions and velocities of molecules in a bunch entering the decelerator (typically Gaussian, for a pulsed supersonic beam,

ref. [72]) occupies a certain region of phase space. In order for the accelerator/decelerator to act on most of the molecules in the bunch, an overlap between the phase space occupied by the bunch and the separatrices for phase-stable acceleration/deceleration needs to be sought. As the calculations of the separatrices attest, the synchronous molecule is always at the center of the phase-stable area, cf. Fig. 3.7. Hence a maximum phase space overlap is achieved when the position and velocity of the synchronous molecule coincides with the most probable position and velocity of the molecular-beam pulse, see Figure 3.8. Thus in an acceleration/deceleration experiment, the synchronous molecule is generally defined by the most probable position and velocity of the molecular-beam pulse.

(b) The *size* of the *phase-stable areas* depends on ϕ_s which, in turn, determines the *acceleration/deceleration rate*. At higher acceleration/deceleration rates, only smaller bunches of molecules can be handled. The largest bunches of molecules can be handled at zero acceleration/deceleration, when a bunch is just transported (or *guided*) through the field array.

(c) The *dominant wave*. Since ε_1 is the largest spatial Fourier coefficient, cf. eq. (3.12), we see that α_{11} supports the largest phase-stable area and affords the highest acceleration/deceleration rate. The corresponding wave, $(1,1)$, referred to as the *first-harmonic wave*, gives the best yield according to this 1-D treatment. *Higher overtones* are normally not used in experiments, but the effects of many of these have been observed [53]. In Chapter 4 we'll examine in more detail the relative sizes of the phase-stable areas due to different overtones.

3.4 Why Does a Single-wave Do Nearly All the Job?

So far we limited our considerations to the single-wave dynamics, i.e. to the equation of motion and its solutions that pertain to a single wave (n,ℓ) interacting with a bunch of molecules. Here we'll show that it is indeed just a single wave that gives a ride to the molecules, with the infinitely many other waves, eq. (3.16), playing no role or a marginal role (see Paragraph 3.5 on interferences).

In order to see why this is the case, we'll look at the effect an arbitrary perturbing wave (r,s) has on the phase-stable motion of molecules due to a (n,ℓ)-wave, whose dynamics we outlined in Paragraph 3.3.

Before delving into that, however, let's consider first the relationship between the velocities of the non-synchronous and synchronous molecules for an arbitrary single wave. Since the averages of the non-synchronous phase and its time derivatives over the oscillation period $\mathcal{T}_{n,\ell}$ are identically equal to zero

$$\langle \dot{\phi}_{n,\ell} \rangle \equiv \frac{1}{\mathcal{T}_{n,\ell}} \int \dot{\phi}_{n,\ell} dt = 0 \tag{3.68}$$

and since, from eq. (3.40),

$$\Delta\dot{z} = \dot{z} - \dot{z}_s = \mathrm{v} - \mathrm{v}_s = nk\Delta\dot{\phi}_{n,\ell} = nk\dot{\phi}_{n,\ell} \tag{3.69}$$

we see that

$$\langle \mathrm{v} - \mathrm{v}_s \rangle = \frac{1}{\mathcal{T}_{n,\ell}} \int (\mathrm{v} - \mathrm{v}_s) dt = \frac{1}{\mathcal{T}_{n,\ell}} \int \mathrm{v} dt - \frac{1}{\mathcal{T}_{n,\ell}} \int \mathrm{v}_s dt = \langle \mathrm{v} \rangle - \langle \mathrm{v}_s \rangle = nk \langle \dot{\phi}_{n,\ell} \rangle = 0 \tag{3.70}$$

i.e., the non-synchronous velocity averaged over a phase oscillation is equal to the average synchronous velocity. This in turn shows that the synchronous velocity (pertaining to a given wave) acts as a *pilot* for the non-synchronous velocity (pertaining to that same wave) as long as phase stability is maintained. Therefore, *molecules which oscillate about a molecule synchronous with an arbitrary wave will get a ride from that wave!* In what follows we'll call a wave that gives a ride to a given bunch of molecules a *resonant wave*.

Let's now approach the problem from the other side and look at the effect of a perturbing wave on the motion driven by a resonant wave. We'll look at the case of zero acceleration/deceleration, i.e., the case when the switching frequency ω is constant and the Stark accelerator/decelerator serves as a *guide*. This will make our calculations simpler, although the same arguments apply to the general case of nonzero acceleration/deceleration. Also, we'll make our notation more accurate and, invoking eqs. (3.32) and (3.39), write the molecule's coordinate due to the ride from the (n, ℓ)-wave as

$$z_{n,\ell}(t) = \frac{\phi_{n,\ell}(t)}{nk} + \frac{\ell}{n}\mathrm{V}_0 t \tag{3.71}$$

For small oscillations, the unperturbed motion of a molecule riding the (n, ℓ)-wave is given by

$$z_{n,\ell}(t) = \frac{\Delta\phi_0}{nk} \cos(\Omega_{n,\ell} t + \delta_0) + \frac{\ell}{n}\mathrm{V}_0 t + \frac{\phi_s}{nk} \tag{3.72}$$

as follows from eqs. (3.39), (3.63) and (3.71). Its velocity is readily obtained by taking the time derivative of eq. (3.72) with the result

$$\mathrm{v}_{n,\ell}(t) = \frac{\ell}{n}\mathrm{V}_0 - \frac{\Delta\phi_0 \Omega_{n,\ell}}{nk} \sin(\Omega_{n,\ell} t + \delta_0) \tag{3.73}$$

The harmonic slow-oscillation frequency $\Omega_{n,\ell}$ is given by eq. (3.64).

We'll consider now the perturbing effect of the (r, s)-wave on the motion of a molecule which is riding the (n, ℓ)-wave. The (r, s)-wave perturbs the ride of the molecule by acting on its coordinate $z_{n,\ell}(t)$ as determined by the (n, ℓ)-wave. As a result, the perturbing (r, s)-wave acts as a time-dependent perturbing force

$$F_{n,\ell}^{r,s}(t) = MA_{r,s} \sin(rkz_{n,\ell}(t) - s\omega t) \tag{3.74}$$

imparting an acceleration to the molecule that is given by

$$\begin{aligned} \ddot{z}^{r,s}_{n,\ell} &= \frac{F^{r,s}_{n,\ell}(t)}{M} = A_{r,s}\sin(rkz_{n,\ell}(t) - s\omega t) \\ &= A_{r,s}\sin\left[\frac{r}{n}\phi_{n,\ell} - \omega^{r,s}_{n,\ell}t\right] \end{aligned} \tag{3.75}$$

where we made use of eq. (3.71) and introduced the frequency

$$\omega^{r,s}_{n,\ell} \equiv \frac{ns - \ell r}{n}\omega \equiv \frac{2\pi}{\tau^{r,s}_{n,\ell}} \tag{3.76}$$

which is a fast-oscillation frequency, since it is on the order of ω. Clearly, the time average of the perturbing force $F^{r,s}_{n,\ell}$ over the perturbation period $\tau^{r,s}_{n,\ell}$ vanishes

$$\langle F^{r,s}_{n,\ell}\rangle \equiv \frac{1}{\tau^{r,s}_{n,\ell}}\int F^{r,s}_{n,\ell}dt = 0 \tag{3.77}$$

as follows by substitution of eq. (3.75) into eq. (3.77) and integration, under the assumption that the slowly oscillating phase $\phi_{n,\ell}$ remains constant over the period $\tau^{r,s}_{n,\ell}$. Hence the perturbing force is seen to average out fast and so the perturbing wave has no *net* effect on the phase-stable motion of the molecule.

The velocity, $\mathrm{v}^{r,s}_{n,\ell}$, and the displacement, $z^{r,s}_{n,\ell}$, imparted by the perturbing wave can be obtained by integrating eq. (3.75). Integrating once (under the assumption of $\phi_{n,\ell}$ constant) yields the instantaneous velocity due to the perturbing wave

$$\mathrm{v}^{r,s}_{n,\ell}(t) = \frac{1}{\omega^{r,s}_{n,\ell}}A_{r,s}\cos\left[\frac{r}{n}\phi_{n,\ell} - \omega^{r,s}_{n,\ell}t\right] \tag{3.78}$$

Integrating once more gives the displacement caused by the perturbing force,

$$z^{r,s}_{n,\ell}(t) = -\frac{1}{\left(\omega^{r,s}_{n,\ell}\right)^2}A_{r,s}\sin\left[\frac{r}{n}\phi_{n,\ell} - \omega^{r,s}_{n,\ell}t\right] \tag{3.79}$$

Thus the effect of the perturbing wave on the velocity and on the displacement of the resonant wave is suppressed by $\omega^{r,s}_{n,\ell}$ and $\left(\omega^{r,s}_{n,\ell}\right)^2$, respectively. We see that the net effect of the perturbing wave vanishes because the perturbing wave fails to displace the molecule. This is indeed the reason why, to an excellent approximation, we are allowed to single out the resonant wave and handle it separately from the perturbing one(s). It is also the reason why a perturbing wave has no influence on phase stability.

The motion of a molecule resonant with the (n,ℓ)-wave and perturbed by the (r,s)-wave can now easily be evaluated (for the case of small oscillations) by simply adding eqs. (3.72) and (3.79) or (3.73) and (3.78), respectively. This analytic result can be compared with the result of a numerical integration of the differential equation for a non-synchronous molecule

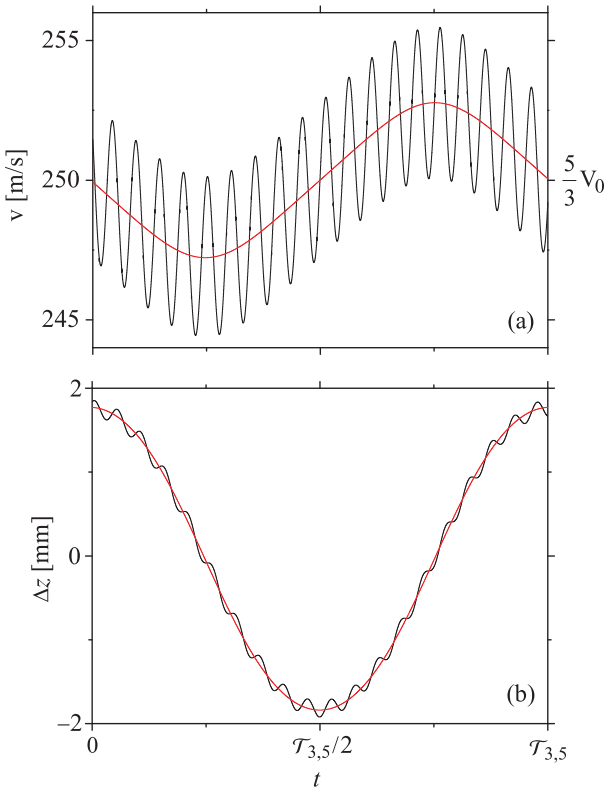

Figure 3.9: *Dynamics of a non-synchronous molecule riding the* $(3,5)$*-wave and perturbed by the* $(1,1)$*-wave. The dynamics is determined by numerically integrating the differential equation of the molecule interacting with only the* $(3,5)$*-wave (red lines) and with both waves (black lines). The initial conditions are chosen such that the* $(3,5)$*-wave is resonant and the* $(1,1)$*-wave perturbing. Both the longitudinal velocity,* $v(t)$*, panel (a), and the relative longitudinal position,* $\Delta z(t) = z(t) - \frac{\ell}{n} V_0 t - \frac{\phi_s}{nk}$*, with respect to the synchronous molecule, panel (b), exhibit slow oscillations (red lines) superposed by fast oscillations (black lines). While the influence of the non-resonant wave on the velocity is significant, its effect on the relative position* $\Delta z(t)$ *is strongly suppressed. The timescale is given in terms of the slow oscillation period* $\mathcal{T}_{n,\ell}$*.*

interacting with the (n,ℓ)- and the (r,s)-wave. For example, for the $(1,1)$- and the $(3,5)$-wave the equation is

$$\ddot{z} = A_{11}\sin(kz - \omega t) + A_{35}\sin(3kz - 5\omega t) \tag{3.80}$$

and Figure 3.9 shows the result of the corresponding numerical integration. The initial conditions are chosen such that the molecule interacts resonantly with the $(3,5)$-wave, which means that the $(1,1)$-wave acts as a non-resonant, perturbing wave. Since the $(1,1)$-wave dominates the right-moving waves and since its phase velocity is close to the $(3,5)$-wave, the perturbing effect of the $(1,1)$-wave is much larger than the effect of all the other waves in the Fourier expansion, eq. (3.16). And yet, this perturbing effect is seen to be strongly suppressed because of the fast oscillations with respect to the $(3,5)$-wave. While the perturbation of the velocity

is still noticeable on a short time scale, see Fig. 3.9 a, the perturbation of the coordinate amounts to just a ripple, see Fig. 3.9 b. We note that the frequency and amplitude of the fast oscillations are correctly predicted by eqs. (3.78) and (3.79), which reconfirms the validity of the assumptions used in our derivation.

In the case of acceleration/deceleration, the switching frequency is not constant, but increases/decreases in time throughout the acceleration/deceleration process. Nevertheless, the treatment of the perturbations for the case of guiding, as given above in this paragraph, remains also in place for the case of acceleration/deceleration, since $\omega(t)$ essentially doesn't change during a fast-oscillation period (typically by less than 1%) and can be treated as a constant.

The above treatment only breaks down in the limit $\omega(t) = kV(t) \to 0$,where the used assumption $\omega(t) \ll \Omega$ doesn't hold anymore. In reality this situation doesn't occur, since even if the molecules are decelerated to velocities conducive for trapping, see ref. [19, 20], then $\omega(t)$ still considerably exceeds Ω and the treatment remains in place.

3.4.1 Two (or More) Waves Travelling with the Same Phase Velocity

When the resonant and perturbing waves travel at the same phase velocity (i.e., for $\ell/n = s/r = \kappa\ell/\kappa n$, with κ an odd integer, the perturbing force, eq. (3.75), does *not* average out. In this case one cannot speak of resonant and nonresonant waves, because all the waves which travel at this same velocity are equally resonant and will jointly create phase stability. Since, obviously, any (n, ℓ) wave has such fellow-traveller waves, $(\kappa n, \kappa\ell)$, this is actually a usual situation. Figure 3.10 a shows typical relative sizes of two waves with successive n, travelling at the same velocity. We see that the resulting shape of the well is dominated by one of the two waves, namely the one with the smaller n, cf. eq. (3.12). Hence in order to draw conclusions about phase stability (which is determined by the shape and depth of the well), we can rely solely on the properties of the *dominant wave*.

However, when calculating switching sequences accurately, the influence of the non-dominant wave(s) cannot be fully dismissed, because of the effect it has on the deceleration a_s (typically, a deviation of a few percent with respect to a single-wave treatment can accumulate over 100 acceleration/deceleration stages). Thus when evaluating the acceleration on a dominant (n, ℓ) wave, one should replace eq. (3.24) with the sum

$$a_s = \sum_{\kappa\ odd}^{\infty} A_{\kappa n,\kappa\ell} \sin(\kappa\phi_s) \tag{3.81}$$

Note that this sum converges very fast, cf. eqs. (3.12), (3.15) and (3.17). Fig. 3.10 b shows, for the case of the $(1, 1)$ dominant wave, the modification of the force due to the presence of the

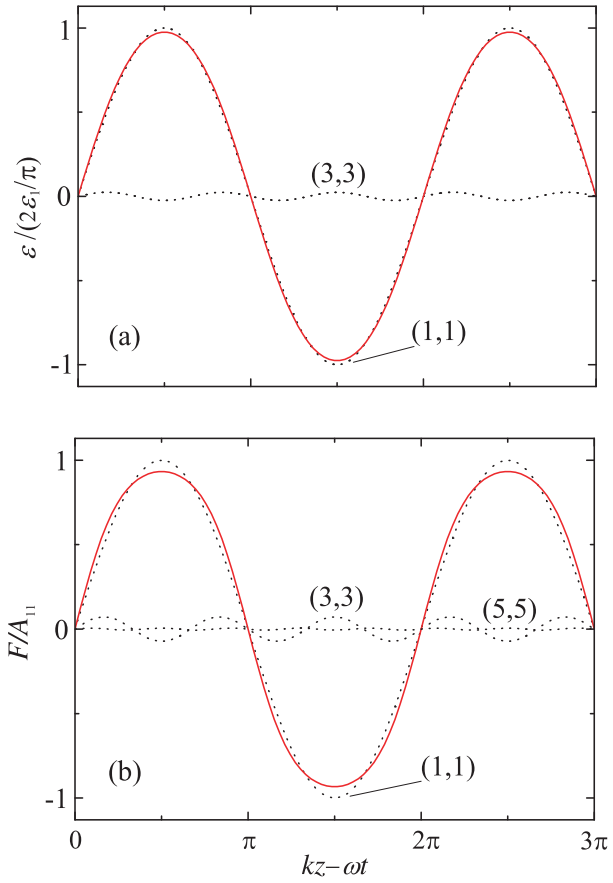

Figure 3.10: *(a) Relative magnitude of the electric fields due to the* $(1,1)$*-wave and the* $(3,3)$*-wave (black dotted curves), which are travelling at the same velocity. These relative magnitudes are typical for two waves with successive* n *and the same velocity. We see that the net field (red curve) is determined predominantly by the* $(1,1)$*-wave, i.e., the one with the smaller value of* n*. The conclusions about phase stability can be reached by considering solely this wave. (b) Typical relative magnitudes of the force due to the* $(1,1)$*-,* $(3,3)$*-, and the* $(5,5)$*-wave (black dotted curves), which are all travelling at the same velocity. Since a small deviation in the force can accumulate when calculating a switching sequence comprising many stages, one should rely on the net force (red curve) rather than on the dominant term.*

resonant non-dominant waves. We note that in order to achieve an accurate correspondence between a_s and ϕ_s, several terms in eq. (3.81) may have to be taken into account.

3.5 Two-wave Interferences

In Paragraph 3.1 it was shown that the electric field in a Stark decelerator consists of an infinite multitude of counter-propagating waves. A common feature of waves is that they interfere. Therefore, we might also expect the occurrence of interference effects in a decelerator.

Consider the differential equation of a molecule interacting with two waves, (n,ℓ) and

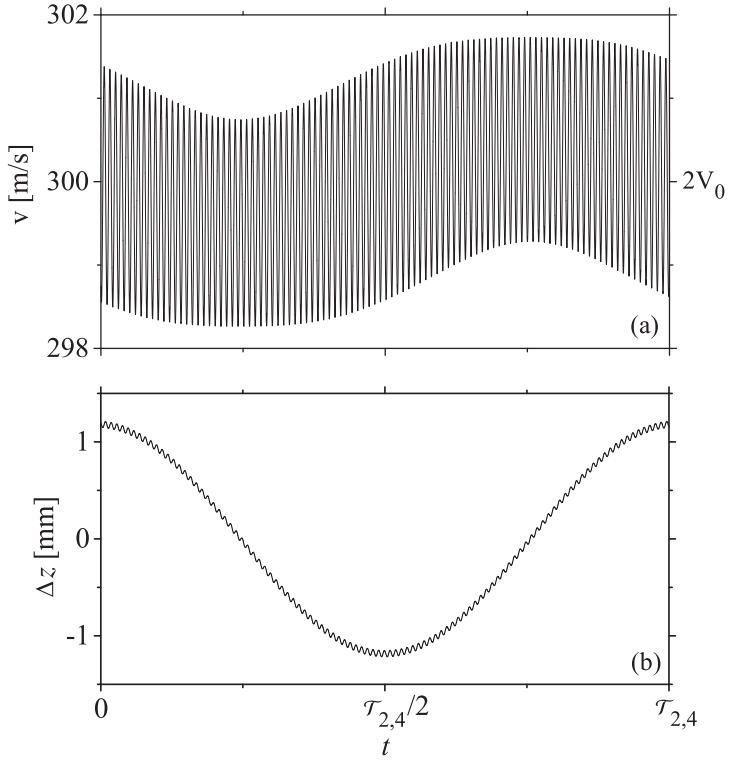

Figure 3.11: *Interference dynamics of a non-synchronous molecule interacting with the* $(1,1)$*-wave and the* $(1,3)$*-wave, that jointly create stability at* $\frac{\ell+s}{n+r}V_0 = 2V_0$*. The dynamics is determined by numerically integrating the equation of motion for a molecule interacting with the two waves, with initial condition* $v(0) \approx 2V_0$*. Both the longitudinal velocity,* $v(t)$*, panel (a), and the relative position,* $\Delta z(t) = z(t) - 2V_0 t$*, panel (b), exhibit slow oscillations superposed by fast oscillations, where we note the similarity with Fig. 3.9. The two interfering waves* $(1,1)$ *and* $(1,3)$ *act together as a single wave* $(2,4)$*, giving rise to a corresponding slow oscillation of period* $\mathcal{T}_{2,4}$*. See text.*

(r,s), for the case of guiding

$$\ddot{z} = A_{n,\ell}\sin(nkz - \ell\omega t) + A_{r,s}\sin(rkz - s\omega t) \tag{3.82}$$

which means that ω is constant. In the following, we will show that these two waves jointly give rise to phase stability at $\frac{\ell+s}{n+r}\mathrm{V}_0$. Since ℓ, s, n and r are odd, $\frac{\ell+s}{n+r}\mathrm{V}_0$ will be called an *even-fraction multiple* of V_0. This in contrast to $\frac{\ell}{n}\mathrm{V}_0$, the velocities at which phase stable areas due to single waves occur. $\frac{\ell}{n}\mathrm{V}_0$ will be called an *odd-fraction multiple* of V_0.

Figure 3.11 illustrates the interference dynamics of a molecule interacting with the (1,1)- and the (1,3)-wave which travel at V_0 and $3\mathrm{V}_0$ respectively. The dynamicswas obtained by numerical integration of eq. (3.82), where the initial condition was chosen such that $\mathrm{v}(0) \approx \frac{\ell+s}{n+r}\mathrm{V}_0 = 2\mathrm{V}_0$. Note the similarity between Fig. 3.9 and Fig. 3.11. Fig. 3.9 pertained to a non-synchronous molecule interacting resonantly with the (3,5)- and non-resonantly with the (1,1)-wave. As a result, the molecule performed slow, stable oscillations around $\frac{5}{3}\mathrm{V}_0$ superposed

by a fast oscillation due to the perturbing (1,1)-wave. Fig. 3.11 shows very similar dynamics, but now the slow, stable oscillation is centered around $2\mathrm{V}_0 = \frac{\ell+s}{n+r}\mathrm{V}_0$. It seems that the (1,1)- and the (1,3)-wave individually act as perturbing waves, but together act as a single stabilizing (2,4)-wave travelling at $\frac{\ell+s}{n+r}\mathrm{V}_0$. In the next paragraph we will show that this is indeed the case.

3.5.1 Derivation

The derivation will consist of four steps.

First, we perform a coordinate transformation

$$z = \mathrm{V}_g t + z_g \tag{3.83}$$

to a frame moving with velocity

$$\mathrm{V}_g = \frac{\ell + s}{n + r}\mathrm{V}_0 \tag{3.84}$$

Inserting eq. (3.84) into equation (3.82) yields

$$\ddot{z_g} = A_{n,\ell}\sin(nkz_g + \omega_g t) + A_{r,s}\sin(rkz_g - \omega_g t) \tag{3.85}$$

where the two waves are seen to act on the molecule with the same frequency

$$\omega_g = \frac{ns - \ell r}{n + r}\omega \tag{3.86}$$

Note that ω_g is a fast oscillation.

Second, we integrate eq. (3.85) under the assumption that the spatial phase kz_g is constant relative to the temporal phase $\omega_g t$. This is consistent with our goal to find stable, slowly oscillating solutions. For the constant spatial phase we take the value $kz_g(t')$, acquired at an arbitrary time t'. Thus we obtain

$$\dot{z_g}(t) = -\frac{A_{n,\ell}}{\omega_g}\cos[nkz_g(t') + \omega_g t] + \frac{A_{r,s}}{\omega_g}\cos[rkz_g(t') - \omega_g t] + C_1 \tag{3.87}$$

where C_1 is an integration constant, which can be evaluated by integrating both sides of eq. (3.87) over a fast oscillation period, $\tau_g \equiv \frac{2\pi}{\omega_g}$. This yields

$$\begin{aligned}
\bar{\dot{z}}_g(t') &\equiv \frac{1}{\tau_g}\int_{t'-\tau_g/2}^{t'+\tau_g/2} \dot{z_g}(t)dt \\
&= \frac{1}{\tau_g}\int_{t'-\tau_g/2}^{t'+\tau_g/2} \left[-\frac{A_{n,\ell}}{\omega_g}\cos[nkz_g(t') + \omega_g t] + \frac{A_{r,s}}{\omega_g}\cos[rkz_g(t') - \omega_g t] + C_1\right] dt \\
&= C_1
\end{aligned} \tag{3.88}$$

Note that eq. (3.87) is only valid for $t \approx t'$. Also note that it correctly describes the amplitude and the frequency of the fast oscillations in Fig. 3.11 a.

With the help of eq. (3.87) we can do a consistency check on our initial assumption that kz_g is constant relative to $\omega_g t$. This assumption is equivalent to $k\dot{z}_g \ll \omega_g$, which upon substitution of equation (3.87) leads to the conditions

$$\frac{k|A_{n,\ell}|}{\omega_g^2} \ll 1 \qquad \text{and} \qquad \frac{k|A_{r,s}|}{\omega_g^2} \ll 1 \tag{3.89}$$

Substituting values belonging to experimental conditions reveal that this condition is well satisfied (typically by a factor of 100).

Integrating equation (3.87) and using eq. (3.88) gives

$$z_g(t) = -\frac{A_{n,\ell}}{\omega_g^2}\sin(nkz_g(t') + \omega_g t) - \frac{A_{r,s}}{\omega_g^2}\sin(rkz_g(t') - \omega_g t) + \bar{\dot{z}}_g(t')(t - t') + C_2 \tag{3.90}$$

where C_2 is another integration constant, which can again be solved by integrating both sides over one period τ_g

$$\begin{aligned} \bar{z}_g(t') &\equiv \int_{t'-\tau_g/2}^{t'+\tau_g/2} z_g(t)dt \\ &= C_2 \end{aligned} \tag{3.91}$$

We note that eq. (3.90) correctly describes the amplitude and the frequency of the fast oscillations in Fig. 3.11 b and that it is valid for $t \approx t'$. In particular, it is valid for $t = t'$, yielding

$$z_g(t') = -\frac{A_{n,\ell}}{\omega_g^2}\sin[nkz_g(t') + \omega_g t'] - \frac{A_{r,s}}{\omega_g^2}\sin[rkz_g(t') - \omega_g t'] + \bar{z}_g(t') \tag{3.92}$$

Since the time t' was chosen arbitrarily, eq. (3.92) holds at *all times*, which makes t' into a *time variable*; we'll denote it by t again ($t' \to t$).

$$z_g(t) = -\frac{A_{n,\ell}}{\omega_g^2}\sin[nkz_g(t) + \omega_g t] - \frac{A_{r,s}}{\omega_g^2}\sin[rkz_g(t) - \omega_g t] + \bar{z}_g(t) \tag{3.93}$$

Eq. (3.93) shows that at every time t the instantaneous position z_g is given by the sum of an average value and a small correction due to fast oscillating perturbations. As in the single-wave case, the time dependence of the average value is not described by fast oscillations, but, as we will see, by slow oscillations. From eqs. (3.89) and (3.93) it follows that

$$z_g(t) \approx \bar{z}_g(t) \tag{3.94}$$

stating that the perturbations do not displace the molecule.

Next we solve equation (3.93) iteratively. Eq. (3.94) assures that already the first iteration (i.e., $z_g(t) \to \bar{z}_g(t)$ on the right hand side) generates an accurate solution

$$z_g(t) = -\frac{A_{n,\ell}}{\omega_g^2}\sin(nk\bar{z}_g(t)+\omega_g t) - \frac{A_{r,s}}{\omega_g^2}\sin(rk\bar{z}_g(t)-\omega_g t) + \bar{z}_g(t) = a + b + \bar{z}_g(t) \tag{3.95}$$

where a and b are shorthands for the first and second term, respectively.

Third, we insert (3.95) into the equation of motion (3.85) and obtain

$$\begin{aligned}\ddot{z_g} = A_{n,\ell}\sin\left(nk\Big(\bar{z}_g - \frac{A_{n,\ell}}{\omega_g^2}\sin(nk\bar{z}_g+\omega_g t) - \frac{A_{r,s}}{\omega_g^2}\sin(rk\bar{z}_g-\omega_g t)\Big) + \omega_g t\right)\\ + A_{r,s}\sin\left(rk\Big(\bar{z}_g - \frac{A_{n,\ell}}{\omega_g^2}\sin(nk\bar{z}_g+\omega_g t) - \frac{A_{r,s}}{\omega_g^2}\sin(rk\bar{z}_g-\omega_g t)\Big) - \omega_g t\right)\end{aligned} \tag{3.96}$$

Because of eq. (3.89), the following trigonometric approximations hold

$$\begin{aligned}\sin[nk(a+b)] &\approx nk(a+b) & \sin[rk(a+b)] &\approx rk(a+b)\\ \cos[nk(a+b)] &\approx 1 & \cos[rk(a+b)] &\approx 1\end{aligned} \tag{3.97}$$

Using the trigonometric identity

$$\sin(\alpha+\beta) = \sin(\alpha)\cos(\beta) + \cos(\alpha)\sin(\beta) \tag{3.98}$$

and the trigonometric approximations of eq. (3.97), eq. (3.96) becomes

$$\begin{aligned}\ddot{z_g} = A_{n,\ell}\sin(nk\bar{z}_g+\omega_g t) + A_{r,s}\sin(rk\bar{z}_g-\omega_g t)\\ -A_{n,\ell}\cos(nk\bar{z}_g+\omega_g t)\Big(\tfrac{nkA_{n,\ell}}{\omega_g^2}\sin(nk\bar{z}_g+\omega_g t) + \tfrac{nkA_{r,s}}{\omega_g^2}\sin(rk\bar{z}_g-\omega_g t)\Big)\\ -A_{r,s}\cos(rk\bar{z}_g-\omega_g t)\Big(\tfrac{rkA_{n,\ell}}{\omega_g^2}\sin(nk\bar{z}_g+\omega_g t) + \tfrac{rkA_{r,s}}{\omega_g^2}\sin(rk\bar{z}_g-\omega_g t)\Big)\end{aligned} \tag{3.99}$$

By invoking the identity $2\sin\alpha\cos\alpha = \sin 2\alpha$, we obtain

$$\begin{aligned}\ddot{z_g} &= A_{n,\ell}\sin\Big(nk\bar{z}_g+\omega_g t\Big) + A_{r,s}\sin\Big(rk\bar{z}_g-\omega_g t\Big)\\ &\quad -\frac{nkA_{n,\ell}A_{rs}}{\omega_g^2}\cos\Big(nk\bar{z}_g+\omega_g t\Big)\sin\Big(rk\bar{z}_g-\omega_g t\Big)\\ &\quad -\frac{rkA_{n,\ell}A_{r,s}}{\omega_g^2}\cos\Big(rk\bar{z}_g-\omega_g t\Big)\sin\Big(nk\bar{z}_g+\omega_g t\Big)\\ &\quad -\frac{nkA_{n,\ell}^2}{2\omega_g^2}\sin\Big(2nk\bar{z}_g+2\omega_g t\Big) - \frac{rkA_{r,s}^2}{2\omega_g^2}\sin\Big(2rk\bar{z}_g-2\omega_g t\Big)\end{aligned} \tag{3.100}$$

With the use of eq. (3.98), we finally receive at

$$\begin{aligned}\ddot{z_g} &= A_{n,\ell}\sin\Big(nk\bar{z}_g+\omega_g t\Big) + A_{r,s}\sin\Big(rk\bar{z}_g-\omega_g t\Big)\\ &\quad -\frac{(r+n)kA_{n,\ell}A_{r,s}}{2\omega_g^2}\sin\Big((n+r)k\bar{z}_g\Big)\end{aligned}$$

$$-\frac{(r-n)kA_{n,\ell}A_{r,s}}{2\omega_g^2}\sin\Big((n-r)k\bar{z}_g+2\omega_g t\Big)$$
$$-\frac{nkA_{n,\ell}^2}{2\omega_g^2}\sin\Big(2nk\bar{z}_g+2\omega_g t\Big)-\frac{rkA_{r,s}^2}{2\omega_g^2}\sin\Big(2rk\bar{z}_g-2\omega_g t\Big) \tag{3.101}$$

In eq. (3.101) every term on the right hand side oscillates fast except for the third term. Indeed, this is the term leading to the slow stable oscillating motion. The other terms average out fast and do not contribute to the displacement of the molecule. To bring equation (3.101) in a more illuminating form we can integrate both sides of the equation over a fast-oscillation period τ_g. All the fast oscillating terms on the right side will give zero and only the third term, which is constant with respect to this integration, remains

$$\bar{\ddot{z}}_g=-\frac{(r+n)kA_{n,\ell}A_{r,s}}{2\omega_g^2}\sin\Big((n+r)k\bar{z}_g\Big)=A_{n+\ell,r+s}\sin\Big((n+r)k\bar{z}_g\Big) \tag{3.102}$$

where

$$\bar{\ddot{z}}_g(t)\equiv\frac{1}{\tau_g}\int_{t-\tau_g/2}^{t+\tau_g/2}\ddot{z}_g(t')dt' \tag{3.103}$$

and

$$A_{n+r,\ell+s}\equiv-\frac{(r+n)kA_{n,\ell}A_{r,s}}{2\omega_g^2} \tag{3.104}$$

Since the derivative commutes with the integral, $\bar{\ddot{z}}_g=\ddot{\bar{z}}_g$, and we see that eq. (3.102) is a second order differential equation for $\bar{z}_g$ ($\approx z_g$). Eq. (3.102) reveals that a molecule that has a coordinate z_g with respect to a synchronous molecule travelling at a velocity V_g, is subject to sine shaped restoring force that leads to slow stabilizing oscillations. This comes about in exactly the same manner as in the case of a single-wave interaction.

Fourth, we realize that the waves (n,ℓ) and (r,s) jointly act as a single wave $(n+r,\ell+s)$. As this wave moves at the phase velocity $\mathrm{V}_g=\frac{\ell+s}{n+r}$, we can ascribe it a phase

$$\phi_{n+r,\ell+s}\equiv(n+r)kz-(\ell+s)\omega t \tag{3.105}$$

Plugging eqs. (3.83) and (3.84) into (3.105) then gives

$$\phi_{n+r,\ell+s}=(n+r)kz_g\approx(n+r)k\bar{z}_g \tag{3.106}$$

which implies

$$\ddot{\phi}_{n+r,\ell+s}\approx(n+r)k\ddot{\bar{z}}_g \tag{3.107}$$

Substitution from eqs. (3.106) and (3.107) into eq. (3.102) yields the final result

$$\ddot{\phi}_{n+r,\ell+s}=(n+r)kA_{n+r,\ell+s}\sin\phi_{n+r,\ell+s}=\alpha_{n+r,\ell+s}\sin\phi_{n+r,\ell+s} \tag{3.108}$$

where we introduced

$$\alpha_{n+r,\ell+s} \equiv (r+n)kA_{n+r,\ell+s} = -\frac{(r+n)^2k^2A_{n,\ell}A_{r,s}}{2\omega_g^2} \tag{3.109}$$

Eq. (3.108) is of the same form as eq. (3.44) for a single-wave interaction in the case of guiding ($\sin\phi_s = 0$). Therefore, all the results (for guiding) obtained from eq. (3.44) are equally valid for interference dynamics. As an example, we can evaluate the slow-oscillation frequency in the harmonic limit, giving

$$\Omega = |\alpha_{n+r,\ell+s}|^{1/2} = \frac{(r+n)k}{\sqrt{2}}\left(\frac{|A_{n,\ell}A_{r,s}|}{\omega_g^2}\right)^{1/2} \equiv \Omega_{n+r,\ell+s} \tag{3.110}$$

cf. eq. (3.64).

The treatment of more interference waves travelling at the same phase velocity is given in Appendix A.

3.5.2 Accelerating/Decelerating on an Interference Wave

Accelerating/decelerating on an interference wave is somewhat trickier than on a single wave. The main reason is that the $A_{n+r,\ell+s}$ coefficient, eq. (3.104), which depends on ω, becomes itself time dependent through the time dependence of $\omega = \omega(t)$. This needs to be taken into account when re-deriving expressions for $\mathrm{v}_s(t)$ and $\omega(t)$ from the condition of a constant synchronous phase with respect to the $(n+r, \ell+s)$ wave.

First, we realize that the acceleration imparted to the synchronous molecule by the interference wave is given by

$$a_s(t) = A_{n+r,\ell+s}(t)\sin\phi_s = -\frac{(n+r)^3}{2(ns-\ell r)^2\omega^2(t)}kA_{n,\ell}A_{r,s}\sin\phi_s \equiv \frac{A_d}{\omega^2(t)} \tag{3.111}$$

where we made use of eqs. (3.24), (3.86), and (3.104) and so is seen to depend on time. This time dependence does not affect the derivation of the interference dynamics (Paragraph 3.5.1) since $\omega(t)$ doesn't change appreciably during a fast-oscillation period. Eq. (3.111) can be integrated to yield the synchronous velocity, which must be equal to the phase velocity:

$$\begin{aligned}\mathrm{v}_s(t) &= \frac{\ell+s}{n+r}\mathrm{V}_0 + \int_0^t a_s(t')dt' = \frac{\ell+s}{n+r}\mathrm{V}_0 + \int_0^t \frac{A_d}{\omega^2(t')}dt' \\ &= \mathrm{V}_{n+r,\ell+s}(t) \equiv \frac{\ell+s}{n+r}\frac{\omega(t)}{k}\end{aligned} \tag{3.112}$$

By taking the time derivative of eq. (3.112) it can be recast into a differential equation for $\omega(t)$

$$\dot{\omega}(t) = \frac{n+r}{\ell+s}\frac{kA_d}{\omega^2(t)} \tag{3.113}$$

which can be easily solved by direct integration. With the initial condition $\omega(0) = k\mathrm{V}_0$ we obtain

$$\omega(t) = \left[\frac{3(n+r)kA_d}{\ell+s}t + (k\mathrm{V}_0)^3\right]^{1/3} \tag{3.114}$$

From eq. (3.114), the temporal phase becomes

$$\theta(t) = \int_0^t \omega(t')dt' = \frac{\ell+s}{4(n+r)kA_d}\left[\frac{3(n+r)kA_d}{\ell+s}t + (k\mathrm{V}_0)^3\right]^{4/3} - \frac{(\ell+s)(k\mathrm{V}_0)^4}{4(n+r)kA_d} \tag{3.115}$$

which generates the switching sequence required for accelerating/decelerating on a interference wave

$$\theta(t) = q\pi \qquad\qquad q = 0, 1, 2, ... \tag{3.116}$$

3.5.3 Multiple Interferences

It is straightforward to generalize the treatment of the interference effect to more than two waves. This can be done by treating the interference wave on the same footing as a single wave and letting it interfere with another single wave, in exactly the same way as the two single waves that gave rise to the interference. This results in a tiny, probably experimentally unobservable effect.

In the next chapter we will compare the analytical results obtained in this chapter with simulations and an experiment.

Chapter 4

Comparison with Simulations and Experiments

Abstract

In the previous chapter we described our analytical results about the dynamics of Stark acceleration/deceleration, considering single-wave interaction, perturbations due to non-resonant waves, two-wave interferences, etc. In this chapter a detailed comparison of the model with numerical simulations is made, demonstrating that the analytic model accurately describes the longitudinal physics in a Stark decelerator. Furthermore, an experiment will be described which showed that an arbitrary wave in the Fourier expansion can be used to perform phase stable deceleration of OH radicals, in complete agreement with the analytic model.

4.1 Full Fledged Dynamics

In paragraph 3.3, we discussed the dynamics due to a single resonant wave. In paragraph 3.5, the dynamics due to two interfering waves was treated, were we showed that together the two waves can also act as a single resonant wave. However, the exact (longitudinal) force that is acting on the molecules, eq. (3.16), is due to infinitely many partial waves, out of which all but one are non-resonant (notwithstanding the discussion of paragraph 3.4.1). In order to fully assess the role of the resonant wave *vis à vis* the non-resonant waves, we evaluated numerically the combined effect due to a large number of waves and compared it with the analytical single-wave treatment. The single-wave dynamics, the full-fledged dynamics and the correction that needs to be applied to the single wave dynamics in order to reproduce the full-fledged dynamics can be best visualized in a phase-space diagram. Such a diagram, or *phase portrait*, exemplified in Figure 4.1, shows the average velocities of the molecules as a function of their initial velocity and initial spatial phase. The link between the average velocity and phase stability is given by eq. (3.70).

The cases of guiding (no acceleration/deceleration) and acceleration/deceleration due to a single wave will be described separately in Paragraphs 4.2 and 4.3. Single-wave dynamics gives rise to features which occur at odd multiples, ℓ/n, of the fundamental velocity V_0. In Paragraph 4.4 we'll deal with features which occur at even multiples of the fundamental velocity V_0. These features arise from the interference of (typically) two adjacent waves.

Although the molecules move from left to right by convention, we will take all waves into account in this chapter, also the ones moving from right to left.

4.2 Guiding

The phase portrait shown in Fig. 4.1 was obtained from a numerical integration of the full equation of motion

$$\ddot{z}(t) = \frac{F(z,t)}{M} \tag{4.1}$$

with $F(z,t)$ given by eq. (3.16) and the temporal phase of the waves given by eq. (3.33), with $\sin\phi_s = 0$ corresponding to guiding. It was found that increasing the number of waves included in the computation beyond 80 ($n \leq 5$, $\ell \leq 25$) didn't lead to any changes of the phase portraits in the range of the initial velocities and positions shown. Moreover, we found that the phase portrait of Fig. 4.1 agrees perfectly well with the one obtained from Monte Carlo trajectory simulations which, in turn, perfectly reproduce experiment [53]. Therefore, for all intends and purposes, the phase portrait of Fig. 4.1 can be considered to be the exact result, reproducing correctly the experimental situation. The phase portrait captures all the complexity of the

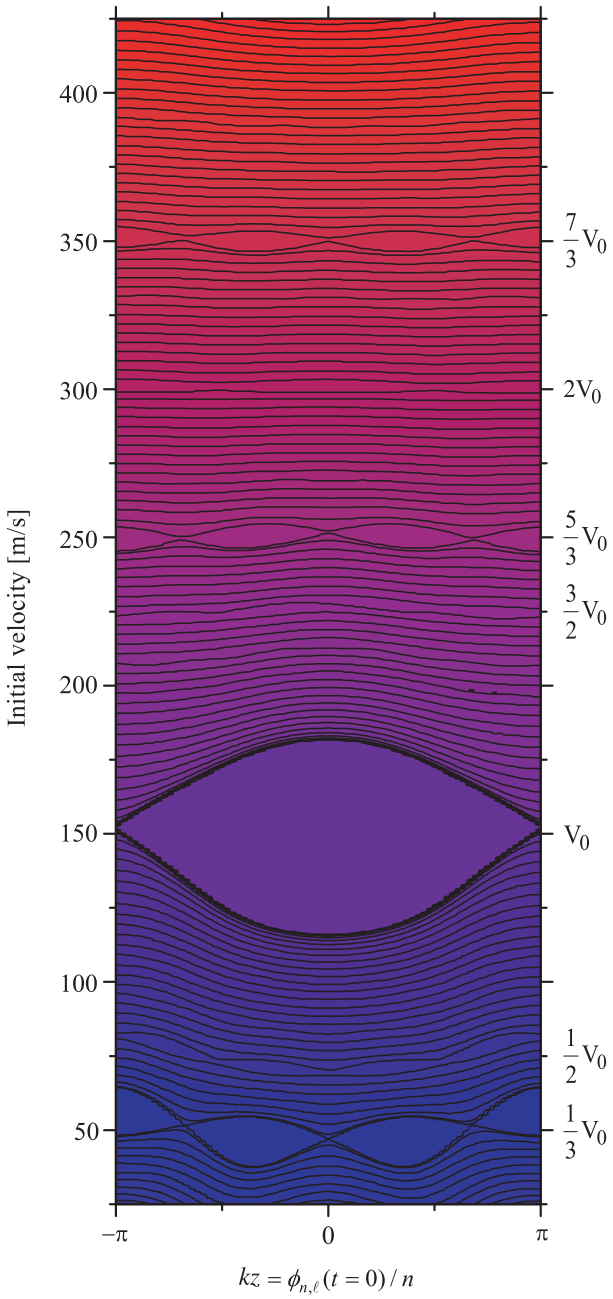

Figure 4.1: *Global phase portrait showing the phase stable areas due to the various waves (case of guiding). The contours pertain to average velocities of OH-molecules plotted as a function of their initial velocity v and initial spatial phase kz. The contour plot is obtained by numerically integrating the full equation of motion for* 80 *waves with a temporal phase corresponding to guiding* ($\sin\phi_s = 0$) *at* $V_0 = 150$ *m/s. The phase portrait is in perfect agreement with Monte Carlo trajectory simulations which, in turn, are in perfect agreement with experiment. See also text.*

dynamics in question and makes it possible to see at a glance the phase-stable areas due to various waves. We remind ourselves of the fact that while the spatial Fourier components of $F(z,t)$ decrease exponentially with increasing n, the temporal Fourier components decrease only as ℓ^{-1}. Therefore, phase-stable areas corresponding to waves with $n > 3$ can hardly be discerned but those with $\ell \lesssim 7$ can still be easily observed in the phase-space area depicted.

Figure 4.2 shows in panels (a) and (b) detailed views of the phase stable areas due to the first harmonic wave $(+,1,1)$ and due to the $(+,3,5)$-wave (note that $\alpha_{11} < 0$ and $\alpha_{3\ell} > 0$ for the example of low-field seeking states considered here). Their main features can be understood from eqs. (3.54) and (3.58), which for the case of guiding become

$$\dot{\phi}_{n,\ell} = \pm[-2\alpha_{n\ell}(\cos\phi_{n,\ell}+1)]^{1/2} \qquad \alpha_{n\ell} < 0 \tag{4.2}$$

and

$$\dot{\phi}_{n,\ell} = \pm[2\alpha_{n\ell}(-\cos\phi_{n,\ell}+1)]^{1/2} \qquad \alpha_{n\ell} > 0 \tag{4.3}$$

We realize that, in general, the phase $\phi_{n,\ell}$, eq. (3.20), pertains to a molecular velocity

$$\mathrm{v}_{n,\ell} = \frac{\dot{\phi}_{n,\ell}}{nk} + \frac{\ell}{n}\mathrm{V}(t) \tag{4.4}$$

Combining eq. (4.4) with eqs. (4.2) and (4.3), yields the separatrices for guiding

$$\mathrm{v}_{n,\ell} = \pm\frac{[-2\alpha_{n\ell}(1+\cos\phi_{n,\ell})]^{1/2}}{nk} + \frac{\ell}{n}\mathrm{V}_0 \tag{4.5}$$

and

$$\mathrm{v}_{n,\ell} = \pm\frac{[2\alpha_{n\ell}(1-\cos\phi_{n,\ell})]^{1/2}}{nk} + \frac{\ell}{n}\mathrm{V}_0 \tag{4.6}$$

The separatrices obtained from eqs. (4.5) and (4.6) are shown in Fig. 4.2 by the white curves. The equations capture all the qualitative features of the respective phase-stable areas seen in Figs. 4.1 and 4.2: (1) the phase stable areas occur at velocities $\frac{\ell}{n}\mathrm{V}_0$; (2) the velocity (i.e., vertical) width of a phase-stable area for a given n is proportional to $\ell^{-1/2}$, because $|\alpha_{n\ell}| \propto \ell^{-1}$, eq. (3.45); (3) the velocity width of a phase-stable area for a given ℓ is proportional to $\exp(-\frac{1}{2}\xi n)$, cf. eqs. (3.12) and (3.45); (4) when kz varies between $-\pi$ to π, then the initial phase $\phi_{n,\ell}(t=0) = nkz$ varies between $-n\pi$ to $n\pi$; as a result, the phase-stable area corresponding to an $(\pm,n,\ell)$ wave consists of n 'fishes' when the horizontal axis $kz = \phi_{n,\ell}(t=0)/n$ spans the interval of $-\pi$ to π; (5) for $\alpha_{n\ell} < 0$, the nodes occur at $\phi_{n,\ell}(t=0)/n = kz = \pm\pi, \pm\pi \mp \frac{2\pi}{n}, \pm\pi \mp \frac{4\pi}{n}, ...$; for $\alpha_{n\ell} > 0$, the nodes occur at $\phi_{n,\ell}(t=0)/n = kz = 0, \pm\frac{2\pi}{n}, \pm\frac{4\pi}{n}, ...$

A closer inspection of Fig. 4.2 reveals that the agreement between the separatrix obtained from either eqs. (4.5) or (4.6) with the exact phase portrait is not perfect. The agreement can be improved to the point of perfection by correcting for the effect of the non-resonant waves.

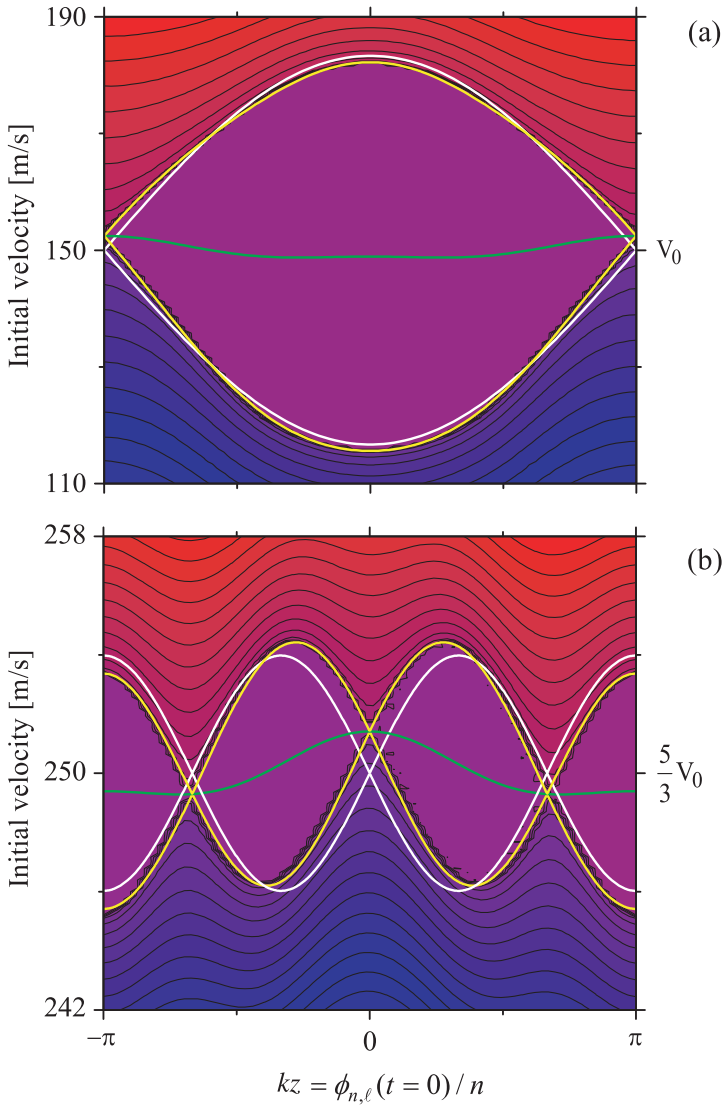

Figure 4.2: *Detailed view of the phase stable areas of Fig. 4.1 around (a) V_0 and (b) $\frac{5}{3}V_0$ (the case of guiding). The contours pertain to average velocities of OH-molecules plotted as a function of their initial velocity v and initial spatial phase kz. Zooming-in at the global phase portrait allows for an accurate comparison of the full-fledged numerical result with the analytic treatment of the dynamics. The white curves show the calculated separatrices for a resonant, single-wave interaction. The green curves comprise the calculated perturbations due to all the other, non-resonant waves. The yellow curves combine the two and are seen to render a perfect agreement with the full-fledged calculation.*

This we do by generalizing the approach developed for a single perturbing wave in Section 4.8 to all the waves, cf. eq. (3.16). As a result

$$\begin{aligned}\tilde{\mathrm{v}}_{n,\ell}(z,t) \;\equiv\; & \sum_{r\ \mathrm{odd}}\sum_{s\ \mathrm{odd}} \mathrm{v}_{n,\ell}^{r,s}(t) = \\ & \sum_{r\ \mathrm{odd}}\sum_{s\ \mathrm{odd}} \frac{n}{\omega(ns-\ell r)} A_{r,s}\cos\left[\frac{r}{n}\phi_{n,\ell} - \frac{\omega(ns-\ell r)}{n}t\right] \\ & + \sum_{r\ \mathrm{odd}}\sum_{s\ \mathrm{odd}} \frac{n}{\omega(ns+\ell r)} A_{r,s}\cos\left[\frac{r}{n}\phi_{n,\ell} + \frac{\omega(ns+\ell r)}{n}t\right] \\ & - \sum_{p\ \mathrm{even}} \frac{n}{p\ell\omega} A_p \cos\left[\frac{p}{n}(\phi_{n,\ell}+\ell\omega t)\right] \end{aligned} \tag{4.7}$$

where $\tilde{\mathrm{v}}_{n,\ell}$ is the velocity change of the molecules riding the resonant $(+,n,\ell)$ wave due to the effect of all the nonresonant waves (so the summation is over all $r,s = 1,3,...$ for which $ns-\ell r \neq 0$). Truncating the summation at $r=1$ and $p=2$, we obtain for $t=0$,

$$\begin{aligned}\tilde{\mathrm{v}}_{n,\ell}(z,t \;=\; & 0) \approx \sum_{s\ \mathrm{odd}} \frac{n}{(ns-\ell)\omega} A_{1s}\cos(kz) \\ & + \sum_{s\ \mathrm{odd}} \frac{n}{(ns+\ell)\omega} A_{1s}\cos(kz) - \frac{n}{2\ell\omega} A_2\cos(2kz) \end{aligned} \tag{4.8}$$

This is shown by the green line in Fig. 4.2 for $s \leq 21$. The yellow line shows the velocity $\mathrm{v}_{n,\ell}(z,t=0)+\tilde{\mathrm{v}}_{n,\ell}(z,t=0)$, and is seen to be in full agreement with the phase-stable area obtained from the full-fledged calculation. Note that no correction was needed for the position of the nodes, as the effect of the non-resonant waves is diminished by a factor proportional to ω^2, see eq. (3.78) and Fig. 3.9 b, and so does not show on the scale of the figure. Furthermore, in order to obtain full agreement with the numerical result, only the dominant resonant wave ($\kappa = 1$, cf. paragraph 3.4.1) has to be taken into account. The influence of the non-dominant resonant waves is also too small to show on the scale of the figure.

4.3 Acceleration/Deceleration

The phase portraits obtained for guiding can be easily generalized to the case of acceleration/deceleration, by incorporating in the numerical calculations a temporal phase, eq. (3.33), corresponding to an accelerating/decelerating wave. Figure 4.3 attests to this being the case: panels (a) and (b) show the same parts of the phase space as panels (a) and (b) in Fig. 4.2, but for $\phi_s = 20°$ and $\phi_s = -170°$, respectively, and both for deceleration.

By combining the eq. (3.54) and (3.58) with (4.4), we obtain the separatrices for

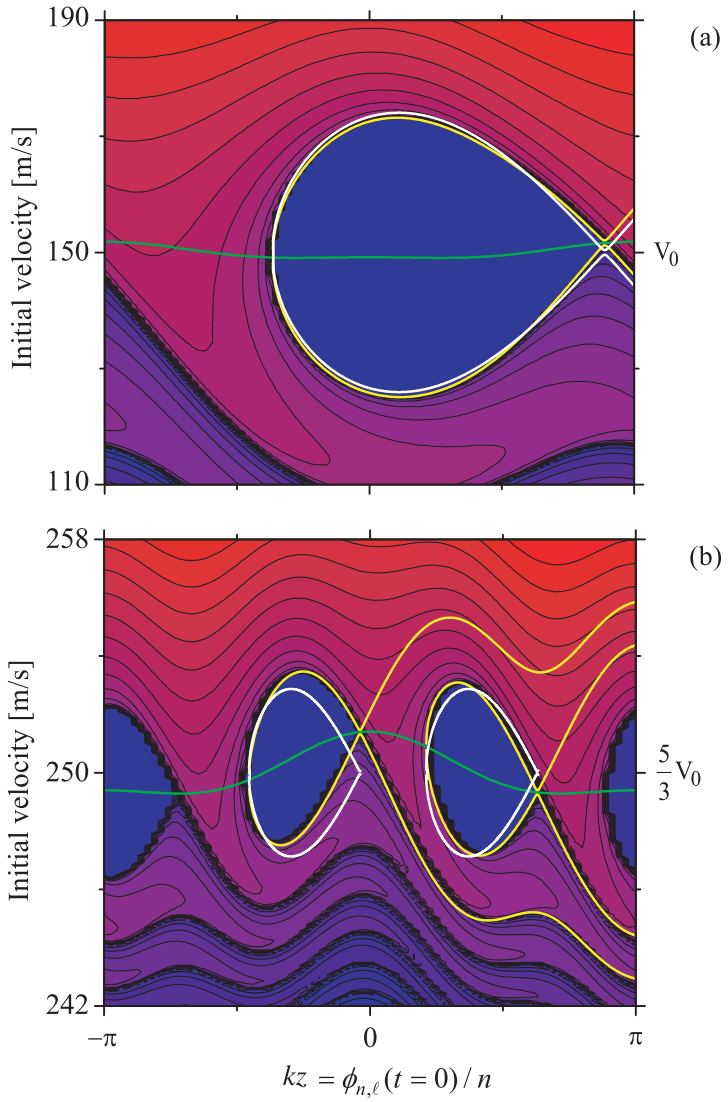

Figure 4.3: *Detailed view of the phase stable areas around (a) V_0 and (b) $\frac{5}{3}V_0$ for the case of deceleration. The contours pertain to average velocities of OH-molecules plotted as a function of their initial velocity v and initial spatial phase kz. The contours were obtained by numerically integrating the full equation of motion for 80 waves, with a temporal phase corresponding to deceleration ($A_{n,\ell} \sin \phi_s < 0$). Panel (a) shows the full-fledged numerical calculation for deceleration on the first harmonic $(+, 1, 1)$ wave with $\phi_s = 20°$. Panel (b) shows the full-fledged numerical calculation for deceleration on the $(+, 3, 5)$-wave with $\phi_s = -170°$. The white curves pertain to the separatrices obtained for a resonant, single-wave interaction. The green curves comprise the calculated perturbations due to all the other, non-resonant waves. The yellow curves combine the two and are seen to be in perfect agreement with the full-fledged calculation. See also text.*

Table 4.1: *Properties of several two-wave interferences*

Interfering waves	$(1,1)$,$(1,3)$	$(1,1)$,$(3,1)$	$(1,1)$,$(5,7)$	$(3,7)$,$(1,3)$
V_g	$\frac{4}{2}\mathrm{V}_0 = 2\mathrm{V}_0$	$\frac{2}{4}\mathrm{V}_0 = \frac{1}{2}\mathrm{V}_0$	$\frac{8}{6}\mathrm{V}_0 = \frac{4}{3}\mathrm{V}_0$	$\frac{10}{4}V_0 = \frac{5}{2}V_0$
$n+r$	2	4	6	4
ω_g	ω	$\omega/2$	$\omega/3$	$\omega/2$
$A_{n+\ell,r+s}$	$-\frac{4k^3W_1^2}{3\pi^2M^2\omega^2}$	$\frac{96k^3W_1W_3}{\pi^2M^2\omega^2}$	$-\frac{540k^3W_1W_5}{7\pi^2M^2\omega^2}$	$\frac{64W_1W_3}{7\pi^2M^2\omega^2}$

deceleration/acceleration

$$\mathrm{v}_{n,\ell}(t) = \pm\frac{[-2\alpha_{n,\ell}(\cos\phi_{n,\ell} + \cos\phi_s + (\phi_{n,\ell} - \pi + \phi_s)\sin\phi_s)]^{1/2}}{nk} + \frac{\ell}{n}\mathrm{V}(t) \tag{4.9}$$

and

$$\mathrm{v}_{n,\ell}(t) = \pm\frac{[2\alpha_{n,\ell}(-\cos\phi_{n,\ell} - \cos\phi_s - (\phi_{n,\ell} + \pi + \phi_s)\sin\phi_s)]^{1/2}}{nk} + \frac{\ell}{n}\mathrm{V}(t) \tag{4.10}$$

The white curves in Fig. 4.3 show the separatrices given by eqs. (4.9) and (4.10) at $t = 0$, the green lines the correction due to the nonresonant waves at $t = 0$, eq. (4.8), and the yellow lines the corrected separatrices at $t = 0$. Again, the agreement with the exact phase portraits is excellent.

4.4 Interference Effects

A close look at Fig. 4.2 reveals small regions of phase stability centered at *even-fraction multiples* of V_0, such as $\frac{6}{4}\mathrm{V}_0$ and $\frac{4}{2}\mathrm{V}_0$. Zooming-in would reveal many more phase stable areas, e.g., at $\frac{10}{4}$ V_0 or $\frac{8}{6}\mathrm{V}_0$. These phase-stable areas cannot arise from single-wave interactions, since, as we saw above, single waves travel at phase velocities $\frac{\ell}{n}\mathrm{V}_0$ with ℓ and n both odd. In Paragraph 3.5 we showed that interferences of two waves give rise to phase stable areas around velocities $\frac{\ell+s}{n+r}\mathrm{V}_0$. Let's see if our treatment of the interference dynamics can indeed explain all the features of the phase stable areas occurring at even-fraction multiples of the fundamental velocity.

Table 4.1 lists properties of interference effects due to different pairs of waves. Thus we see that the stability at $\frac{4}{2}$ V_0 results from the interference of the $(1,1)$- and the $(1,3)$-wave, whereas the stability at $\frac{2}{4}\mathrm{V}_0$ is generated by the $(1,1)$- and the $(3,1)$-wave. Fig. 4.1 shows that the phase-stable area at $\frac{4}{2}\mathrm{V}_0$ exhibits two 'fishes', whereas phase stability at $\frac{2}{4}\mathrm{V}_0$ exhibits four. This is in agreement with our treatment, since it follows immediately from the $(n+r)$-factor in eqs. (3.105) and (3.108), as explained in the discussion of Paragraph 4.2. Furthermore, the

sign of the prefactor $\alpha_{n+r,\ell+s}$ explains correctly whether the interference effect exhibits a node or an antinode at $z = 0$.

Let us zoom-in in Fig. 4.1 on the phase-stable area occurring at $2V_0$, and use it as a testing ground for the accuracy of our treatment of the interference effects. This phase-stable area is displayed in Figure 4.4 a. The white curve shows the separatrix obtained from eqs. (3.105), (3.109) and (4.5) for the resonant $(+, n + r, \ell + s) = (+, 2, 4)$-wave. We see that it correctly renders the size of the separatrix but not quite its shape. As in the case of single-wave dynamics, in order to obtain a full agreement between our theory and the exact result we have to take into account the influence of the perturbing waves. This influence can be taken into account in exactly the same way as before, i.e., by means of eq. (4.8). We have to substitute into it $n + r = 2$ for n and $\ell + s = 4$ for ℓ, which gives

$$\begin{aligned}
\tilde{\mathrm{v}}_{2,4}(z, t &= 0) \approx \sum_{p \text{ odd}} \frac{2}{(2p-4)\omega} A_{1,p} \cos(kz) \\
&\quad + \sum_{p \text{ odd}} \frac{2}{(2p+4)\omega} A_{1,p} \cos(kz) - \frac{2}{8\omega} A_2 \cos(2kz) \\
&= \sum_{p \text{ odd}} \left(\frac{1}{(p-2)p} + \frac{1}{(p+2)p} \right) \frac{A_{1,1}}{\omega} \cos(kz) - \frac{A_2}{4\omega} \cos(2kz) \\
&= -\frac{A_2}{4\omega} \cos(2kz) \qquad (4.11)
\end{aligned}$$

We see that in this particular case, the sum over p vanishes and so the correction given by eq. (4.11) takes quite a simple form. The correction is shown by the green curve in Fig. 4.4 a. The yellow curve is a sum of the white and green curves, and is seen to agree perfectly with the exact separatrix. We thus arrive at the conclusion that our analytic model accounts perfectly well for the observed phase stability at even-fraction multiples of the fundamental velocity, in terms of interferences of waves with n, ℓ odd.

4.4.1 Acceleration/Deceleration on an Interference Wave

In Paragraph 3.5 we derived a time sequence for accelerating/decelerating on an interference wave. The corresponding temporal phase, eq. (3.115), was used in a full-fledged calculation for the case of deceleration (at $\phi_s = 20°$) to generate the phase portrait shown in Figure 4.4 b.

Since for deceleration on an interference wave $\alpha_{n+r,\ell+s}$ is time-dependent, cf. eqs. 3.109 and 3.114, an exact evaluation of the separatrices is not possible. Still, the size and shape of the resulting separatrix can be approximated very well by treating $\alpha_{n+r,\ell+s}(t)$ as a constant, since $\alpha_{n+r,\ell+s}(t)$ varies very slowly in time. In order to correctly approximate the size of the separatrix, we need to take the minimum value of $|\alpha_{n+r,\ell+s}(t)|$, corresponding to the smallest

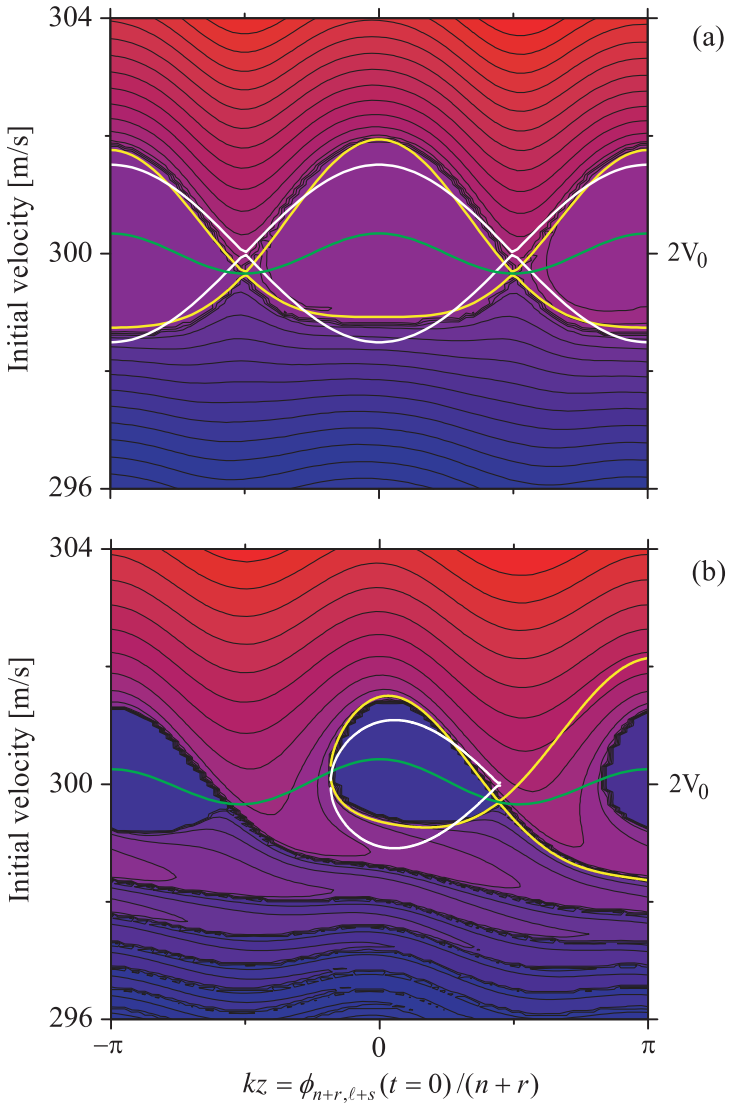

Figure 4.4: *Detailed view of the phase stable area around $2V_0$ for the case of guiding (with $\phi_s = 0°$), panel (a), and for deceleration ($\phi_s = 20°$), panel (b). The contours pertain to average velocities of OH-molecules plotted as a function of their initial velocity v and initial spatial phase kz. The full-fledged numerical calculations are compared with the analytic result for the case of the interference of the $(+,1,1)$-wave with the $(+,1,3)$-wave, which give jointly rise to a $(+,2,4)$-wave. The white curves show the calculated separatrices at $t = 0$. The green curves comprise the calculated perturbations due to all non-resonant waves. The yellow curves combine the two and are seen to be in excellent agreement with the full-fledged numerical calculation. See also text.*

potential well/separatrix. The reason for this is that the time scale at which molecules are lost is much smaller than the timescale at which the potential well increases. As a result, the minimum well depth determines the total amount of molecules that is captured and the size of the resulting phase stable area. For deceleration, the value of $|\alpha_{n+r,\ell+s}(t)|$ is minimal at $t = 0$. The white curve in Fig. 4.4 b corresponds to the separatrix obtained by substituting $\alpha_{n+r,\ell+s}(t = 0)$ into eq. (4.9). Also shown are the perturbations by all the other waves obtained from eq. (4.11) (green curve) and the resulting separatrix taking both effects into account (yellow curve). Again, a very good agreement between the latter and the full-fledged calculation is found.

4.5 An Experiment: Deceleration on the (3,5)-wave

So far, only a comparison of the wave model with the numerical integration of the full equation of motion (4.1) were made. Although they render exactly the same longitudinal results as full 3-D Monte Carlo trajectory simulations, which in turn excellently reproduce experimental data [53], it would still felt as a challenge to test the derived dynamics of Chapter 3 directly in a new experiment.

Phase-stable *guiding* using overtones ($n = 3, 5, ..$) was already performed and extensively studied in ref. [53]. In the same paper, also guiding on interference waves was demonstrated, although it was given a different interpretation there as second-order resonances. *Deceleration* on overtones ($n = 3, 5, ..$) and interference waves, however, was not performed before, because of two reasons: first of all, it was unclear from the 'intuitive model' (cf. Paragraph 1.2.5) if the phase stability obtained in guiding, would be maintained for deceleration. Second, deceleration on an overtone or interference wave is of little practical interest, because of the small deceleration rates and phase stable areas. In fact, an interference wave renders such a small deceleration rate, that it cannot even be observed in a 108 stage decelerator. Still, overtone deceleration yields an observable effect, which provides a possibility for an experimental test of the general treatment of single-wave interactions as given in Chapter 3, where it was shown that overtones give rise to phase-stable motion, also for deceleration.

In the performed experiment, eq. (3.34) was used to generate two switching sequences; one for guiding on the $(3, 5)$-wave and one for deceleration with $\phi_s = 53°$. The sequences were applied to the setup discussed in Paragraph 2.2.3, where Xenon was used as a carrier gas. For guiding, the applied switching sequence pertained to $V_0 = \frac{3}{5} \times 370$ m/s $= 222$ m/s, realizing a resonant interaction between the $(3, 5)$-wave and molecules travelling at the mean velocity

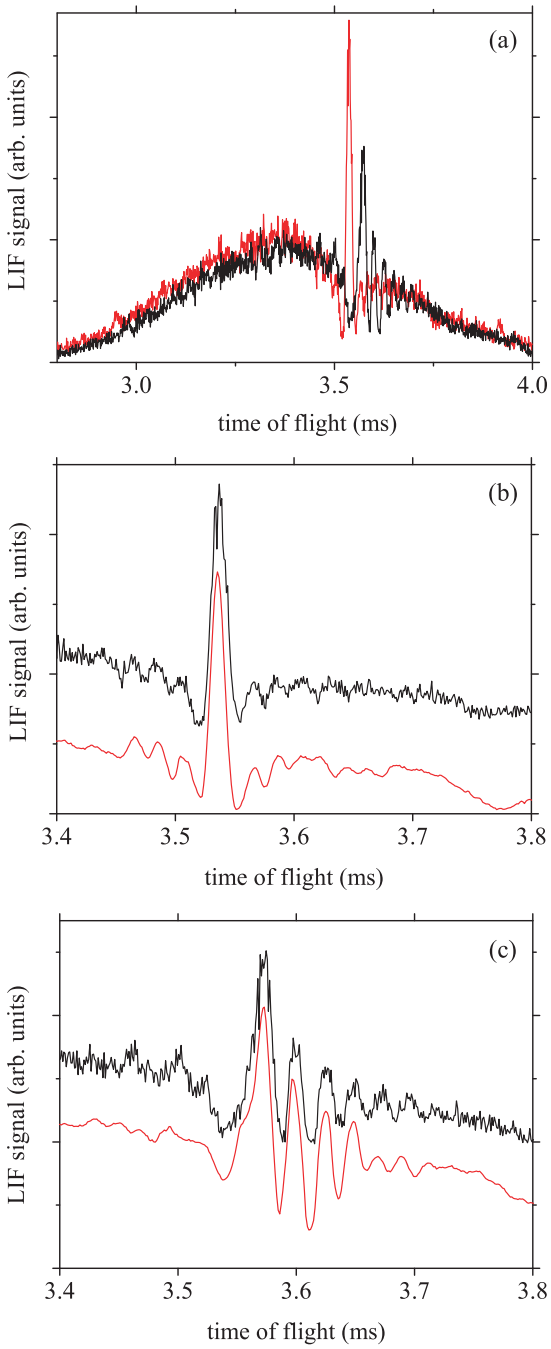

Figure 4.5: *Experiment showing phase stable guiding and deceleration of OH radicals on the* $(3,5)$*-wave. Two switching sequences were applied to the experimental setup described in Paragraph 2.2.3; one for guiding and one for deceleration* ($\phi_s = 53°$) *on the* $(3,5)$*-wave. Xenon was used as a carrier gas. Panel (a) shows the obtained experimental data consisting of two time of flight profiles. The red curve corresponds to guiding, the black curve to deceleration. Zooming into panel (a), we obtain panel (b), showing the TOF profile of the guiding experiment (black curve), and (c) showing the TOF profile of the deceleration experiment (black curve) in more detail. The results of Monte Carlo trajectory simulations (red curves) are added to both panels. Note the excellent agreement between the experimental data and the trajectory simulations.*

of the molecular beam pulse, about 370 m/s. For deceleration, the applied switching sequence pertained to an initial fundamental phase velocity of $V_i = \frac{3}{5} \times 370 = 222$ m/s and a final velocity of $V_f = \frac{3}{5} \times 362 = 217$ m/s, corresponding to a deceleration of the molecular beam from 370 m/s to 362 m/s.

The results of the experiment are displayed in Figure 4.5. Panel (a) shows the obtained experimental data consisting of two time of flight profiles, that are seen to be slightly shifted with respect to each other. The red curve with the higher peak corresponds to guiding, whereas the black curve with the lower peak, slightly shifted to the right, corresponds to deceleration. Note that this is also what one would expect for a decelerated peak. The time delay between the two peaks is 38 ± 10 μs, perfectly agreeing with the calculated delay of 36 μs for a deceleration from 370 m/s to 362 m/s in the decelerator described in Paragraph 2.2.3. This demonstrates that arbitrary waves in the Fourier expansion can be used to perform phase-stable deceleration.

By zooming into panel (a), we obtain both panel (b) showing the TOF profile of the guiding experiment, and panel (c) showing the TOF profile of the deceleration experiment in more detail. Each panel consists of two curves, a black one showing the experimental data, and a red one obtained from 3-D Monte Carlo trajectory simulations. Note the excellent quantitative agreement between the experiments and the trajectory simulations. Not only the shape and the position of the main peaks, but also the more detailed structure, such as the oscillations adjacent to the main peaks, are accurately reproduced. These oscillations can be understood from the motion of molecules that are *almost* phase stable, and are called phase space modulations. For a detailed discussion of phase space modulations, see [18].

Chapter 5

Summary and Conclusions

Stark deceleration is a technique that uses time-varying electric fields to decelerate a molecular beam to arbitrary velocities in the lab frame. It has resulted in the electrostatic trapping of ND_3 and OH [19, 20]. Furthermore, Stark deceleration gives rise to a very rich (longitudinal) dynamics, which has been studied extensively in this thesis by means of the wave model.

The wave model is based on the Fourier analysis of the time-varying, inhomogeneous electric fields in a decelerator, which can be Fourier expanded both in space and time. Performing the expansions reveals that the electric fields give rise to an infinite multitude of stationary as well as counter-propagating waves [2]. In this thesis, we tackled explicitly the resonant interaction of the molecules with an arbitrary wave in the Fourier expansion, where the isomorphism with the biased pendulum problem was exploited to obtain a description of phase stability, which is both intuitive and analytic. Furthermore, we studied the influence of non-resonant, perturbing waves, whose effect was shown to be heavily suppressed and therefore of no consequence for phase stability. Finally, we treated the dynamics of molecules interacting with two interfering waves that act together as a single wave and therefore also give rise to phase stable motion.

Furthermore, we compared the analytic results extensively with the numerical integration of the full equation of motion, taking into account as many as 80 waves in the Fourier expansion. The numerical integration yields the same longitudinal results as Monte Carlo trajectory simulations, which in turn excellently reproduce experimental data. We found that all analytic results were in excellent agreement with the numerical simulations. Every detail of the very rich structures observed in phase space could be accounted for by considering single wave dynamics, non-resonant perturbations or interference dynamics.

The link between the various stable regions in phase space and the experimentally observed first and second order resonances, was first studied in ref. [53]. As it turns out, the

wave model gives new interpretations of these resonances in terms of single wave interactions (for the first order resonances) and interference wave interactions (for the second order resonances). The wave model was also able to extend the study in ref. [53], performed for the case of guiding, to the general case of acceleration/deceleration. In this context a new experiment was performed, showing that arbitrary overtones in the decelerator can be used to perform phase stable deceleration. The wave model was found to be in full agreement with the experiment.

Appendix A

Comparison of Interference Effects with Second-order Resonances

In Paragraph 3.5 the dynamics due to two interfering waves was treated. In particular, it was shown that the $(+,1,1)$- and the $(+,1,3)$-wave jointly create phase stability at $2V_0$. But these are not the only waves that create stability at this velocity. An interference wave, just as a single wave, always has fellow travellers. For example, the $(-,1,1)$- and the $(+,1,5)$-wave also create phase stability at $2V_0$, just as the $(-,1,3)$- and the $(+,1,7)$-wave, etc. The combined effect of these fellow travellers is small; in total they give rise to a correction of about 4 % to the separatrix obtained from the interference of just the $(+,1,1)$- and the $(+,1,3)$-wave. But there is a more important reason for evaluating the effect of all these fellow travellers explicitly, namely the possibility of a comparison with an earlier obtained expression for second-order resonances by the 'intuitive model' [53]. Here, an analytic expression explaining the resonance at $2V_0$ was obtained in a completely different way.

The main difference between the wave model and the intuitive model, is that the wave model also performs a Fourier expansion of the electric fields in time, whereas the intuitive model doesn't. As a result, the intuitive model always takes implicitly all temporal waves into account. Therefore, in order to be able to make a comparison with the intuitive model, all the waves due to the temporal Fourier expansion have to evaluated. This will be done here.

From eq. (3.17), (3.86) and (3.109), we obtain for $\alpha_{2,4}$ due to the $(+,1,1)$- and the $(+,1,3)$-wave

$$\alpha_{2,4} = -\frac{8k^4 W_1^2}{3\pi^2 M^2 \omega^2} \tag{A.1}$$

The same evaluation can be done for the $(-,1,1)$- and the $(+,1,5)$-wave, where we note the

extra minus sign of the left moving wave

$$\alpha_{2,4} = \frac{8k^4 W_1^2}{45\pi^2 M^2 \omega^2} \tag{A.2}$$

Taking all combinations of $(\pm, 1, \ell)$ waves into account that generate phase stability at $2V_0$, we obtain for the total $\alpha_{2,4}$

$$\alpha_{2,4} = -\frac{8k^4 W_1^2}{\pi^2 M^2 \omega^2} \left(\frac{1}{3} - \sum_{i=3,5,\ldots}^{\infty} \frac{1}{i^2(i-2)(i+2)} \right) = -\frac{k^4 W_1^2}{4M^2\omega^2} \tag{A.3}$$

This expression for the total $\alpha_{2,4}$ gives rise to the following slow-oscillation frequency in the harmonic limit

$$\Omega_{2,4} = \sqrt{|\alpha_{2,4}|} = \sqrt{\frac{k^4 W_1^2}{4M^2\omega^2}} \tag{A.4}$$

An analytic expression for the slow-oscillation frequency $\Omega_{2,4}$ can also be obtained from the intuitive model in a completely different way. In this model the equation of motion takes the following form [53] (if we use the appropriate translation between the definitions of the intuitive model and the wave model: $L \to \lambda/2$, $m \to M$, $a_n \to W_n$, $v_{sw} \to V_0 = \omega/k$)

$$\frac{M\lambda}{2\pi} \frac{d^2\Delta\phi}{dt^2} = \bar{F}(\phi_0 + \Delta\phi) - \bar{F}(\phi_0) \tag{A.5}$$

where $\Delta\phi = k\Delta z$ with Δz the difference in position between a synchronous and a non-synchronous molecule, $\phi_0 = \phi_s/n$ and $\bar{F}$ is the average force acting on a molecule, which is evaluated from the amount of energy that the molecule loses between successive switch times. In ref. [53], also an analytic expression was obtained for the Stark energy that a synchronous molecule travelling at $2V_0$ loses after 2 times switching, namely

$$\Delta W_{Stark}(\phi_0) = \frac{\pi k^2 W_1^2}{2M\omega^2} \sin 2\phi_0 \tag{A.6}$$

Furthermore, a synchronous molecule with a velocity of $2V_0$ travels 2λ between two switching times (= 1 period τ), which leads to an average force on the synchronous molecule given by

$$\bar{F}(\phi_0) = -\frac{\Delta W_{Stark}}{2\lambda} = -\frac{k^3 W_1^2}{8M\omega^2} \sin 2\phi_0 \tag{A.7}$$

resulting in the equation of motion

$$\frac{M\lambda}{2\pi} \frac{d^2\Delta\phi}{dt^2} = -\frac{k^3 W_1^2}{8M\omega^2} [\sin 2(\phi_0 + \Delta\phi) - \sin 2\phi_0] \tag{A.8}$$

In the harmonic limit, i.e. $\Delta\phi \ll 1$, the following approximations hold

$$\sin 2\Delta\phi \approx 2\Delta\phi \tag{A.9}$$

$$\cos 2\Delta\phi \approx 1 \tag{A.10}$$

Together with (3.98), eqs. (A.9), (A.10) can be used to rewrite (A.8) yielding

$$\frac{d^2\Delta\phi}{dt^2} = -\frac{k^4 W_1^2 \cos 2\phi_0}{4M^2\omega^2}\Delta\phi \tag{A.11}$$

We note that for the case of guiding $\phi_0 = 0$. From eq. (A.11) we can immediately read off the corresponding slow oscillation frequency in the harmonic limit

$$\Omega = \sqrt{\frac{k^4 W_1^2}{4M^2\omega^2}} \tag{A.12}$$

which is in exact agreement with the result obtained from the wave model, eq. (A.4).

The same discussion can be applied to phase stability at $\frac{1}{2}\mathrm{V}_0$. Not only the $(+,1,1)$- and the $(+,3,1)$-wave create phase stability at this velocity, but also the $(+,1,3)$- and the $(-,3,1)$-wave, just as the $(-,1,1)$- and the $(+,3,3)$-wave, etc. Taking all combinations of $(\pm,1,\ell)$- and $(\pm,3,\ell)$-waves into account that generate phase stability at $\frac{1}{2}\mathrm{V}_0$, we obtain for the total $\alpha_{4,2}$

$$\begin{aligned}\alpha_{4,2} &= \frac{96k^4 W_1 W_3}{\pi^2 M^2\omega^2}\left(4 - \sum_{i=1,3,\ldots}^{\infty}\left(\frac{1}{(i+1/2)^2 i(i+2)} + \frac{1}{(i+3/2)^2 i(i+2)}\right)\right) \\ &= \frac{16k^4 W_1 W_3}{M^2\omega^2}\left(4 - \frac{16}{3\pi}\right)\end{aligned} \tag{A.13}$$

The corresponding slow-oscillation frequency $\Omega_{4,2}$ is

$$\Omega_{4,2} = \sqrt{\frac{16k^4 W_1 W_3}{M^2\omega^2}\left(4 - \frac{16}{3\pi}\right)} \tag{A.14}$$

This can again be compared with the results from the intuitive model obtained in ref. [53]. Here, an analytic expression was given for the Stark energy that a synchronous molecule travelling at $\frac{1}{2}\mathrm{V}_0$ loses after 4 times switching

$$\Delta W_{Stark}(\phi_0) = \frac{8\pi k^2 W_1 W_3}{M\omega^2}\left(4 - \frac{16}{3\pi}\right)\sin 4(\phi_0 - \pi/4) \tag{A.15}$$

Furthermore a synchronous molecule with a velocity of $\frac{1}{2}\mathrm{V}_0$ travels λ between four switching times ($= 2\tau$), which leads to an average force on the synchronous molecule given by

$$\bar{F}(\phi_0) = -\frac{\Delta W_{Stark}}{\lambda} = -\frac{4k^3 W_1 W_3}{M\omega^2}\left(4 - \frac{16}{3\pi}\right)\sin 4(\phi_0 - \pi/4) \tag{A.16}$$

In the same way as above we can derive the slow-oscillation frequency in the harmonic limit for the case of guiding, giving

$$\Omega = \sqrt{\frac{16k^4 W_1 W_3}{M^2\omega^2}\left(4 - \frac{16}{3\pi}\right)} \tag{A.17}$$

which is in exact agreement with the result obtained from the wave model, eq. (A.14).

So we see that the analytic results of the wave model describing interference effects are in full agreement with earlier obtained expressions by the intuitive model describing second-order resonances. Since both results have been obtained in a completely different way, the validity of the results is independently and mutually confirmed. Both models describe equally well the experimentally observed resonances that occur at even-fraction multiples of the fundamental phase velocity.

Bibliography

[1] H.L. Bethlem, G. Berden, and G. Meijer, Phys. Rev. Lett. **83**, 1558 (1999).

[2] B. Friedrich, Eur. Phys. J. D **31**, 313 (2004).

[3] J. van Veldhoven, J. Küpper, H.L. Bethlem, B. Sartakov, A.J.A. van Roij, and G. Meijer, Eur. Phys. J. D. **31**, 337 (2004)

[4] S.Y.T. van de Meerakker, N. Vanhaecke, M.P.J. van der Loo, G.C. Groenenboom, and G. Meijer, Phys. Rev. Lett. **95**, 013003 (2005).

[5] L.R. Hunter, Science, **252**, 73 (1991).

[6] J.J. Hudson, B.E. Sauer, M.R. Tarbutt, and E.A. Hinds, Phys. Rev. Lett. **89**, 023003 (2003).

[7] D.W. Rein, J.Mol. Evol. **4**, 15 (1974).

[8] V.S. Letokhov, Phys. Lett. **53A**, 275 (1975).

[9] M. Anderson, J. Ensher, M. Matthews, C. Wieman, E. Cornell, Science **269**, 198 (1995).

[10] B. de Marco, D. Jin, Science **285**, 1703 (1999).

[11] M.O. Mewes, M.R. Andrews, D.M. Kurn, D.S. Durfee, C.G. Townsend, W. Ketterle, Phys. Rev. Lett **78**, 582 (1997).

[12] S.E. Harris, L.V. Hau, Phys. Rev. Lett. **82**, 4611 (1999).

[13] C. Liu, Z. Dutton, C.H. Behroozi, L.V. Hau, Nature **409**, 490 (2001).

[14] M. Baranov, L. Dobrek, K. Goral, L. Santos, and M. Lewenstein, Phys. Scr. **T102**, 74 (2002)

[15] L. Santos, G.V. Shlyapnikov, P. Zoller, and M. Lewenstein, Phys. Rev. Lett. **85**, 1791 (2000).

[16] D. Herschbach, Rev. Mod. Phys. **71**, S411 (1999).

[17] N. Balakrishnan and A. Dalgarno, Chem. Phys. Lett. **341**, 652 (2001).

[18] S.Y.T. van de Meerakker, PhD Thesis, Radboud Universiteit Nijmegen (2005).

[19] H.L. Bethlem, G. Berden, F.M.H. Crompvoets, R.T. Jongma, R.T., A.J.A. van Roij, and G. Meijer, Nature, **406**, 491 (2000).

[20] S.Y.T van de Meerakker, P.H.M. Smeets, N. Vanhaecke, R.T. Jongma, and G. Meijer, Phys. Rev. Lett. **94**, 23004 (2005).

[21] D. DeMille, Phys. Rev. Lett. **88**, 067901 (2002).

[22] H.L. Bethlem, PhD Thesis, Katholieke Universiteit Nijmegen (2002).

[23] S. Chu, Rev. Mod. Phys. **70**, 685 (1998); C.N. Cohen-Tannoudji, Rev. Mod. Phys. **70**, 707 (1998); W.D. Phillips, Rev. Mod. Phys. **70**, 721 (1998).

[24] W. Ketterle and N.J. van Druten 1996, Adv. At., Mol., Opt., Phys. **37**, 181 (1996).

[25] M. Greiner, C.A. Regal, and D.S. Jin, Nature **426**, 537 (2003).

[26] S. Jochim, M. Bartenstein, A. Altmeyer, G. Hendl, S. Riedl, C. Chin, J. Hecker-Denschlag, and R. Grimm, Science **302**, 2101 (2003).

[27] C.A. Stan, M.W. Zwierlein, C.H. Schunck, S.M.F. Raupach, and W. Ketterle, Phys. Rev. Lett. **93**, 143001 (2004).

[28] S. Inouye, J. Goldwin, M.L. Olsen, C. Ticknor, J.L. Bohn, and D.S. Jin, Phys. Rev. Lett **93**, 183201 (2004).

[29] A.J. Kerman, J.M. Sage, S. Sainis, T. Bergeman, and D. DeMille, Phys. Rev. Lett. **92**, 033004 (2004).

[30] A.J. Kerman, J.M. Sage, S. Sainis, T. Bergeman, and D. DeMille, Phys. Rev. Lett. **92**, 153001 (2004).

[31] J.M. Sage, S. Sainis, T. Bergeman, and D. DeMille, Phys. Rev. Lett. **94**, 203001 (2005).

[32] J.M. Doyle, B. Friedrich, J. Kim, and D. Patterson, Phys. Rev. A **52**, R2515 (1995).

[33] B. Friedrich, R. deCarvalho, J. Kim, D. Patterson, J.D. Weinstein, and J.M. Doyle, J. Chem. Soc. Faraday Trans. **94**, 1783 (1998).

[34] J.D. Weinstein, R. deCarvalho, T. Guillet, B. Friedrich, and J.M. Doyle, Nature **395**, 148 (1998).

[35] M. Gupta and D. Herschbach, J. Phys. Chem. A **103**, 10670 (1999).

[36] M.S. Elioff, J.J. Valentini, and D.W. Chandler, Science **302**, 1940 (2003).

[37] R. Fulton, A.I. Bishop, and P.F. Barker, Phys. Rev. Lett. **93**, 243002 (2004).

[38] J.G. King, J.R. Zacharias, Quart. Progr. Rep. **48**, 15 January 1958, Research Laboratory of Electronics, MIT (1958).

[39] D. Auerach, E.E.A. Bromberg, L. Wharton, J. Chem. Phys. **45**, 2160 (1966).

[40] F.M.H. Crompvoets, H.L. Bethlem, R.T. Jongma, and G. Meijer, Nature **411**, 174 (2001).

[41] F.M.H. Crompvoets, H.L. Bethlem, J. Küpper, A.J.A. van Roij, and G. Meijer, Phys. Rev. A **69**, 063406 (2004).

[42] F.M.H. Crompvoets, R.T. Jongma, H.L. Bethlem, A.J.A. van Roij, and G. Meijer, Phys. Rev. Lett. **89**, 093004 (2002).

[43] H.L. Bethlem, A.J.A. van Roij, R.T. Jongma, and G. Meijer, Phys. Rev. Lett. **88**, 133003 (2002).

[44] J. van Veldhoven, H.L. Bethlem, and G. Meijer, Phys. Rev. Lett. **94**, 083001 (2005).

[45] J.R. Bochinski, E.R. Hudson, H.J. Lewandowski, G. Meijer and J. Ye, Phys. Rev. Lett. **91**, 243001 (2003).

[46] J.R. Bochinski, E.R. Hudson, H.J. Lewandowski, and J. Ye, Phys. Rev. A **70**, 043410 (2004).

[47] V. Veksler, *J. Phys.* (USSR) **9**, 153 (1944).

[48] E.M. McMillan, *Phys. Rev.* **68**, 143 (1945).

[49] H.L. Bethlem, G. Berden, A.J.A. van Roij, F.M.H. Crompvoets, and G. Meijer, Phys. Rev. Lett. **84**, 5744 (2000).

[50] H.L. Bethlem, F.M.H. Crompvoets, R.T. Jongma, S.Y.T. van de Meerakker, and G. Meijer, Phys. Rev. A **65**, 053416 (2002).

[51] H.L. Bethlem and G. Meijer, Int. Rev. Phys. Chem. **22**, 73 (2003).

[52] S.Y.T. van de Meerakker, N. Vanhaecke, H.L. Bethlem, and G. Meijer, Phys. Rev. A (in press).

[53] S.Y.T. van de Meerakker, N. Vanhaecke, H.L. Bethlem, and G Meijer, Phys. Rev. A **71**, 053409 (2005).

[54] P.F. Bernath, *Spectra of atoms and molecules*, (Oxford University Press, New York, 1995).

[55] G. Herzberg, *Molecular Spectra and Molecular Structure*, Volume 1 - Spectra of Diatomic Molecules, (Krieger Publishing Company, Malabar, Florida, 1950).

[56] R.N. Zare, *Angular momentum*, (John Wiley & Sons, New York, 1988).

[57] W. Gordy and R.L. Cook, *Microwave Molecular Spectra*, (John Wiley & Sons, New York, 1970).

[58] H.-J. Loesch and A. Remscheid, J. Chem. Phys **93**, 4779 (1990)

[59] B. Friedrich and D.R. Herschbach, Z. Phys. D. **18**, 153 (1991)

[60] G.H. Dieke and H. M. Crosswhite, J. Quant. Spectrosc. Radiat. Transf. **2**, 97 (1962)

[61] W.L. Meerts, Chem. Phys. Lett. **46**, 24 (1977)

[62] P. Andresen and E. Rothe, J. Chem. Phys. **82**, 3634 (1985)

[63] G. Scoles, *Atomic and Molecular Beam Methods*, Volume 1, (Oxford University Press, New York, 1988).

[64] B. Friedrich, *From the new world of cold molecules*, lecture notes, TU Berlin (2005)

[65] R.W. Anderson, J. Phys. Chem. A **101**, 7664 (1997)

[66] D.R. Yarkony, J. Chem. Phys. **97**, 1838 (1992)

[67] G.B. Arfken and H.J. Weber, *Mathematical methods for physicists* (Academic Press, New York, 1995)

[68] B. Friedrich and D.R. Herschbach, Comm. At. Mol. Phys. **32**, 47 (1995).

[69] The Stark-energy Fourier coefficients W_i of eq. (3.15) concide with the Stark-energy Fourier coefficients a_i introduced in previous work, ref. [51], i.e., $W_i = a_i$.

[70] Formula (3.35) is identical with eq. (15) of ref. [51] for $n = \ell = 1$ where, in the notation used in that reference, it takes the form $t(q) = \frac{mL}{2a_1 \sin\phi_0} \left(v(z=0) - \sqrt{v^2(z=0) - \frac{4qa_1}{m} \sin\phi_0} \right)$. The old notation translates into the new one in the following way: $a_1 \to W_1$; $\phi_0 \to \phi_s/n$; $L \to \frac{\lambda}{2}$, so that $k = \frac{2\pi}{\lambda} = \frac{\pi}{L}$; $m \to M$; $v(z=0) \to \mathrm{V}_0$; $s \to \frac{\ell}{n}$

[71] Formula (3.65) differs from eq. (10) of ref. [53] which, in the old notation, cf. endnote [70], reads $\sqrt{\frac{a_n \cos(n\phi_0)}{2\pi m s L^2}}$, and so is seen to lack a factor of $n^{1/2}$ in the numerator.

[72] R. Campargue, *Atomic and Molecular Beams* (Springer, Berlin, 2001)